MINIATURIZED PULSE TUBE REFRIGERATORS

A Dissertation
Presented to
The Academic Faculty

By

Theodore J Conrad

In Partial Fulfillment
Of the Requirements for the Degree
Doctor of Philosophy in Mechanical Engineering

Georgia Institute of Technology

August, 2011

MINIATURIZED PULSE TUBE REFRIGERATORS

Approved By:

Dr. S. Mostafa Ghiaasiaan, Advisor
School of Mechanical Engineering
Georgia Institute of Technology

Dr. Timothy C. Lieuwen
School of Aerospace Engineering
Georgia Institute of Technology

Dr. Prateen V. Desai
School of Mechanical Engineering
Georgia Institute of Technology

Dr. Carl S. Kirkconnell
Chief Technology Officer
Iris Technology Corporation

Dr. Sheldon M. Jeter
School of Mechanical Engineering
Georgia Institute of Technology

Date Approved: May 16, 2011

ACKNOWLEDGEMENTS

There are quite a few people who deserve my deepest thanks for their support and encouragement during this endeavor. First and foremost I would like to thank my advisor, Dr. S. Mostafa Ghiaasiaan, for his guidance and his patience. I would also like to thank my other committee members, Dr. Prateen V. Desai, Dr. Sheldon M. Jeter, Dr. Timothy C. Lieuwen, and Dr. Carl S. Kirkconnell for their interest in and technical assistance with this work.

I am also grateful to Dr. Tom Crittenden and Dr. Slava Yorish at Virtual AeroSurface Technologies for their contributions to this work. Slava performed the arduous task of individually punching all of the wire mesh screens for the experimental portion of the investigation. Additionally, I have had the pleasure of working with an outstanding group of fellow graduate students; they have provided feedback and ideas for this research and they have helped to make my time at Georgia Tech much more enjoyable than it might have been otherwise. Those who have worked with me in the cryogenics laboratory are Jeff Cha, Will Clearman, Evan Landrum, Mihir Pathak, and Tom Mulcahey, but outside of this group there are many more than I can possibly name here. A special acknowledgement is necessary to Evan Landrum for his role in the experimental investigations which were part of this work.

There are several people who have supported me through this undertaking in more personal ways. I am immensely grateful to my family for their unwavering support. I would like to especially thank my parents, Kathy and Charlie Conrad, without whom this would never have been possible, and my grandfather, Hunter Jack Conrad, whose

lifelong passion for education was an inspiration. I would also like to express my deepest appreciation to Stephanie Lin for her support, patience, and understanding, particularly during the more trying times of this endeavor.

TABLE OF CONTENTS

LIST OF TABLES

LIST OF FIGURES

NOMENCLATURE

Variables

A, B	Moving piston oscillatory motion amplitude (m)
a	Taper length (m)
b	Taper depth (m)
c	Step height (m)
C_p	Specific heat at constant pressure (J/kg K)
c_f	Forchheimer's inertial coefficient (-)
COP	Coefficient of performance (-)
$\overline{\overline{C}}$, C	Inertial resistance tensor, scalar (m^{-1})
$\overline{\overline{D}}$, D	Viscous resistance tensor, scalar (m^{-2})
D	Pulse tube diameter (m)
e	Specific total energy content (J/kg)
$\vec{F}$	Volumetric body force vector (N/m^3)
g	Gravitational acceleration (m/s^2)
h	Specific enthalpy (J/kg)
H	Enthalpy flow rate (W)
J	Diffusion flux (kg/m^2s)
k	Thermal Conductivity (W/m K)
K	Darcy permeability (m^2)
P	Pressure (Pa)
Pr	Prandtl number (-)
Q	Heat flux (W)

r	Tapered component radius (m)
R	Regenerator radius (m)
s	Specific entropy (J/kg K)
S	Source (-)
t	Time (sec)
T	Temperature (K)
$\vec{u}$	Velocity, superficial velocity (m/s)
$\vec{v}$	Physical velocity (m/s)
V	Volume (m^3)
W	Work (W)
Wo	Womersley number (-)
Z	Pressure amplitude (Pa)

Greek Letters

β	Ratio of component volume to compressor swept volume (-)
δ	Penetration depth (m)
δ	Regenerator defect length (m)
ε	Porosity (-)
θ	Taper angle (Deg)
ϕ	Phase angle (rad)
μ	Dynamic viscosity (kg/m s)
υ	Specific volume (m^3/kg)
ρ	Density (kg/m^3)
$\bar{\bar{\tau}}$	Viscous stress tensor (N/m^2)

ω	Angular frequency (rad/sec)

Subscripts

c	Cold
Carnot	Carnot
eff	Effective
f	Fluid
in	Input
m	Mass
h	Enthalpy
osc	Oscillatory
R	Refrigeration
sol	Solid
T	Thermal
V	Viscous
void	Void or pore volume
w	Warm
total	Total
m	Mass

SUMMARY

Pulse tube refrigerators (PTR) are robust, rugged cryocoolers that do not have a moving component at their cold ends. They are often employed for cryogenic cooling of high performance electronics in space applications where reliability is paramount. Miniaturizing these refrigerators has been a subject of intense research interest because of the benefits of minimal size and weight for airborne operation and because miniature coolers would be an enabling technology for other applications. Despite much effort, the extent of possible PTR miniaturization is still uncertain.

To partially remedy this, an investigation of the miniaturization of pulse tube refrigerators has been undertaken using several numerical modeling techniques. In support of these models, experiments were performed to determine directional hydrodynamic parameters characteristic of stacked screens of #635 stainless steel and #325 phosphor bronze wire mesh, two fine-mesh porous materials suitable for use in the regenerator and heat exchanger components of miniature PTRs. Complete system level and pulse tube component level CFD models incorporating these parameters were then employed to quantitatively estimate the effects of several phenomena expected to impact the performance of miniature PTRs. These included the presence of preferential flow paths in an annular region near the regenerator wall and increased viscous and thermal boundary layer thicknesses relative to the pulse tube diameter. The effects of tapering or chamfering the junctions between components of dissimilar diameters were also investigated.

The results of these models were subsequently applied to produce successively smaller micro-scale PTR models having total volumes as small as 0.141 cc for which

sufficient net cooling was predicted to make operation at cryogenic temperatures feasible. The results of this investigation provide design criteria for miniaturized PTRs and establish the feasibility of their operation at frequencies up to 1000 Hz with dimensions roughly an order of magnitude smaller than those that have recently been demonstrated, provided that challenges related to their regenerator fillers and compressors can be addressed.

CHAPTER 1

INTRODUCTION

1.1 Cryocoolers

Small cryogenic refrigerators, or cryocoolers, are used for cooling of relatively small heat loads at cryogenic temperatures, typically defined as 120 K and below. Many high performance electronic devices either require or may benefit from this cooling and therefore cryocoolers are often enabling components for these systems. Infrared focal plane arrays and superconducting quantum interference devices (SQUIDS) are examples of such devices for which cryocoolers are typically employed. Other common applications include cooling the superconducting magnets of MRI systems, cryopumping for semiconductor fabrication, and gas liquefaction. There is also an emerging need for relatively small and inexpensive cryocoolers to cool high-temperature superconductors for electric power and telecommunications applications.

Several types of cryocoolers have been developed to meet various demands, each having its own advantages and drawbacks [1-3]. They may generally be divided between regenerative and recuperative devices based upon their operating principles, although the thermoelectric coolers included here fall outside these classifications. Regenerative cooling cycles operate with oscillatory flow and the working fluid is alternately heated and cooled as it undergoes periodic displacement over the course of a cycle. Common regenerative cryocooler types include Stirling, Gifford–McMahon (GM), and pulse tube refrigerators (PTR's). Recuperative cycles operate with steady flow; reverse Brayton and

Joule-Thomson coolers are common examples of this type. Schematics of these cryocoolers are shown in Figure 1.1, followed by more detailed descriptions of their operating principles and brief discussion of their potential for adaptation to miniature scales. Thermoelectric coolers will also be included due to their potential to compete with miniature cryocoolers for higher temperature applications.

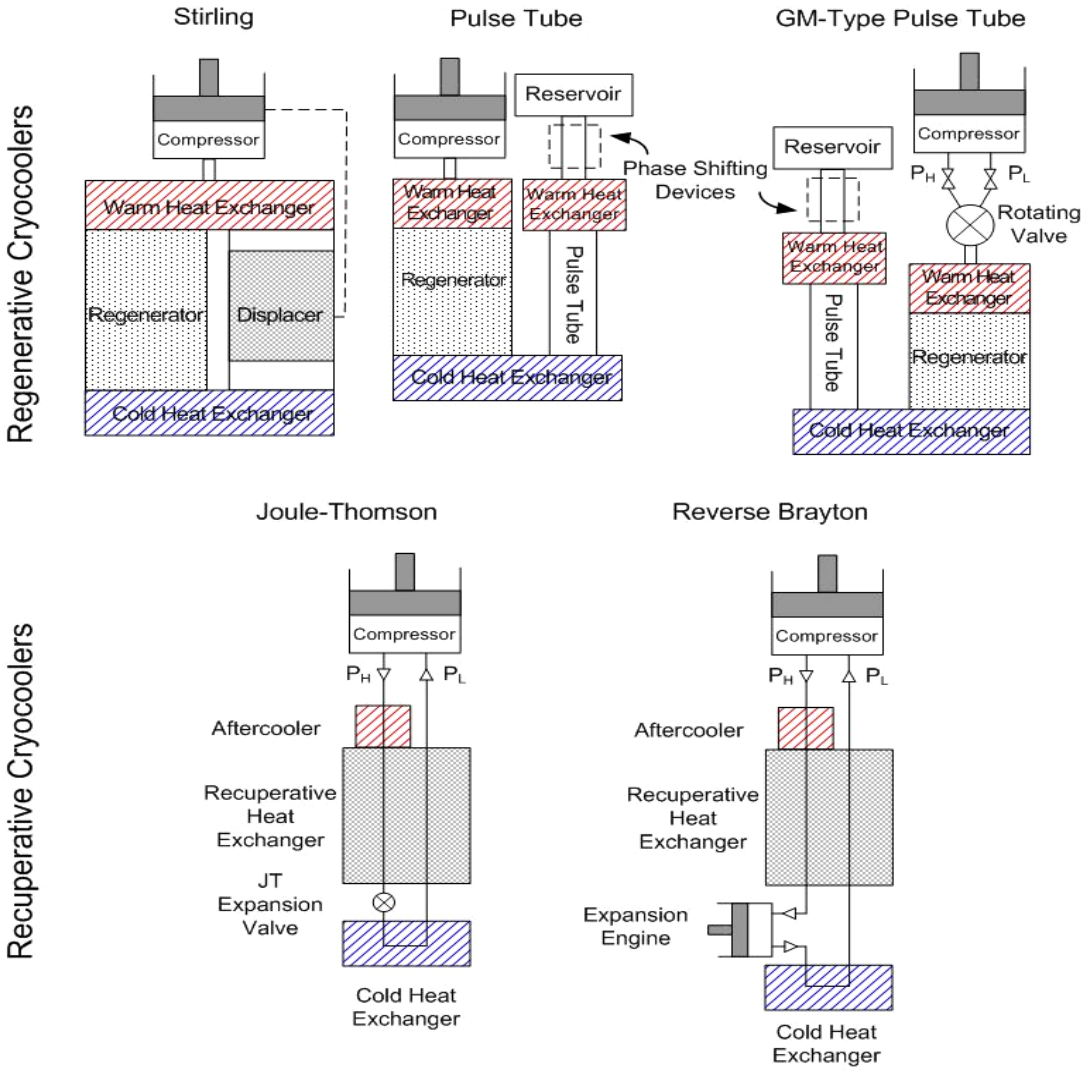

Figure 1.1 Schematics of selected cryocoolers

1.1.1 Stirling Refrigerators

Stirling cryocoolers operate on the Stirling refrigeration cycle, which is identical to the Stirling power cycle but operates in the reverse direction. In fact, refrigeration, heat pumping, or work production using the Stirling cycle may all be accomplished with identical hardware [2]. The ideal Stirling cycle is internally and externally reversible and therefore has a thermal efficiency identical to the Carnot cycle. It is made up of four completely reversible processes, as shown on T-s and P-υ diagrams in Figure 1.2. These processes are:

1-2 Isothermal compression and heat rejection at the warm temperature

2-3 Constant volume regeneration and displacement to the cold end

3-4 Isothermal expansion and heat absorption at the cold temperature

4-1 Constant volume regeneration and displacement to the warm end

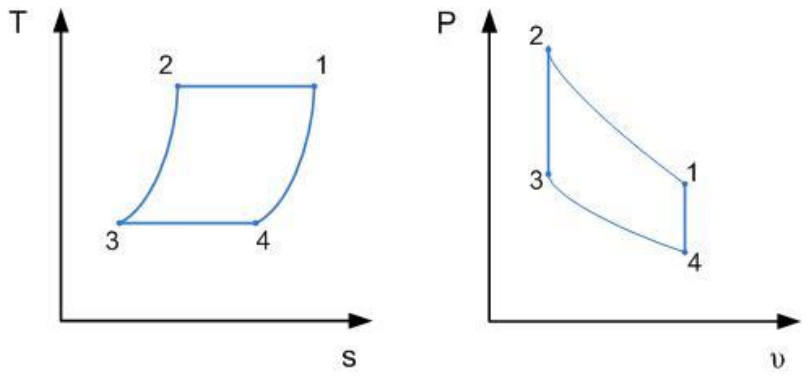

Figure 1.2 T-s and P-υ diagrams of the ideal Stirling cycle

Stirling cryocoolers have been produced in large numbers for cooling night vision equipment and other tactical infrared sensors. Adapted with flexure bearings and non-contacting clearance seals, long life Stirling coolers have successfully fulfilled the

rigorous requirements of space-based applications [4]. Their miniaturization involves many of the same challenges encountered in miniaturizing pulse tube refrigerators, particularly those involving the regenerators present in both devices [5,6]. These are discussed in further detail in Chapter 2. Very small tactical Stirling coolers having expander lengths of 11-12 cm and mass of approximately 1 kg are currently commercially available [7,8], and even smaller models (65 mm, 0.8 kg) have been demonstrated for higher temperature (130 K) applications [9].

1.1.2 Pulse Tube Refrigerators

Pulse tube refrigerators are similar to Stirling devices, with the pulse tube and associated phase shifting device taking the place of the moving piston on the cold end. The addition of these components makes it difficult to define a thermodynamic cycle for PTR's, however, because the processes experienced by a parcel of the working fluid depend on its location within the device. Because of their mechanical simplicity and lack of moving parts in the cold end, PTRs are extremely robust; they are therefore an attractive option for space applications and others which require very high reliability. The lack of moving parts in the cold end also gives them an advantage over other devices for applications which are sensitive to vibration. Their efficiency, which once lagged behind that of the other available cryocoolers and limited their employment, has now equaled and in cases even surpassed that of Stirling cryocoolers [1]. PTRs of various designs and scales have been widely employed to meet a variety of needs, from multiple stage cryocoolers capable of cooling small loads at temperatures as low as 2 K to industrial scale refrigerators cooling 2 kW at 120 K for liquefying natural gas [3].

Since their introduction by Gifford and Longsworth in 1964 [10], a great deal of work has been done to improve the performance, reliability, and efficiency of pulse tube refrigerators. New designs have been developed incorporating additional components such as orifices, bypass lines, and inertance tubes. Gifford and Longsworth's device, now referred to as the basic pulse tube refrigerator, reached a minimum cold end temperature of 124 K. This performance was markedly improved with the addition of an orifice and reservoir by Mikulin in 1984 [11] and subsequent modification by Radebaugh in 1986 [12], leading to the orifice pulse tube refrigerator (OPTR) shown in Figure 1.3A, which was capable of reaching 60 K. Further improvement came with the addition of a bypass line and secondary orifice by Zhu in 1990 [13], which offered improved control over the phasing between pressure and flow oscillations and thereby increased the efficiency of the PTR. This double inlet pulse tube refrigerator (DIPTR) achieved a temperature of 42 K at the cold end and is shown in Figure 1.3B. In 1997, Zhu reported the effectiveness of "long neck tubes" for controlling the phase [14] and Gardner and Swift replaced the orifice with an inertance tube [15], resulting in the inertance tube pulse tube refrigerator (ITPTR) shown in Figure 1.3C.

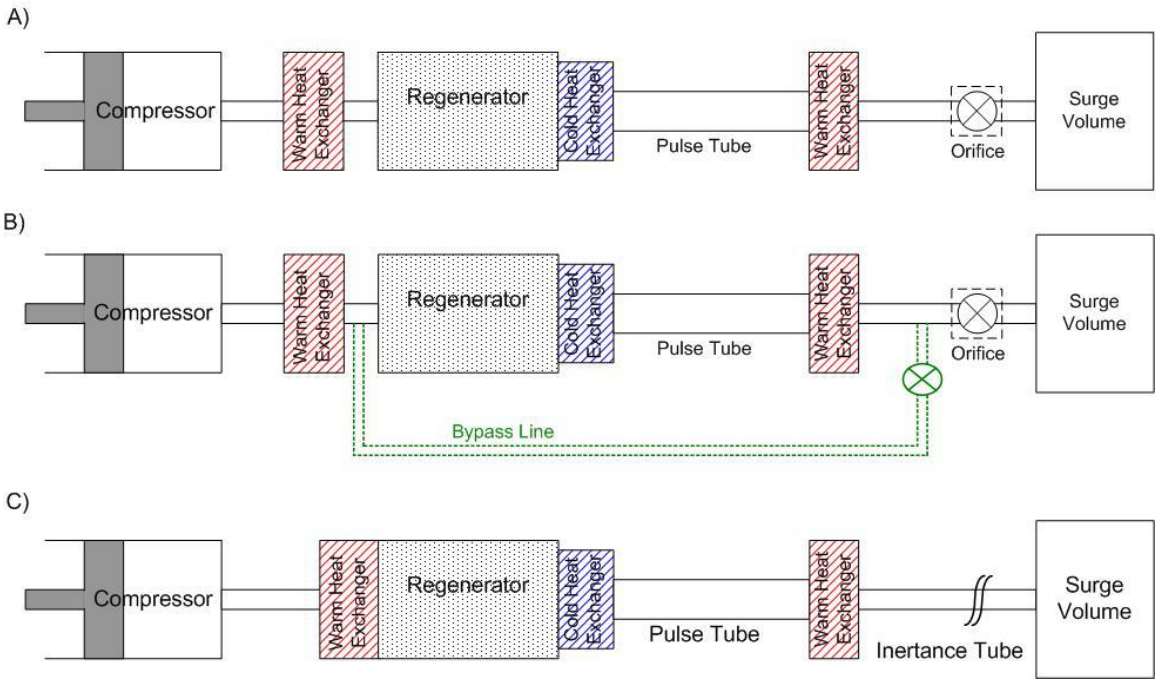

Figure 1.3 Schematics of several types of pulse tube refrigerators

More recent research [1] has focused on improving the efficiency of pulse tube cryocoolers, particularly at very low temperatures (4 - 10 K) where efficiencies of approximately 1% of Carnot are typical. Operation at higher frequencies for higher power density has also been of great interest, both for obtaining more cooling from a PTR of a given size and to allow for smaller devices. Higher frequencies for pulse tube and Stirling cryocoolers are generally defined as those above 60 Hz. There has also been significant research activity devoted to miniaturizing pulse tube refrigerators which will be reviewed in detail in the next chapter. The combination of high efficiency, which they share with Stirling coolers, and lack of cold end moving parts which are potentially problematic at miniature scales make pulse tube refrigerators especially promising as miniature cryocoolers.

1.1.3 Gifford-McMahon Refrigerators

Gifford-McMahon and GM-type pulse tube coolers substitute a mechanical valve switching between high and low pressure sources for the oscillating piston compressors of Stirling and pulse tube refrigerators. This modification allows the use of more common oil lubricated compressors which have historically reduced the cost and improved the reliability of GM coolers relative to other devices. The addition of the mechanical valve generally limits the operating frequency of GM coolers to a few Hz but allows the cooler to work with a pressure ratio unconstrained by the swept volume of the pressure oscillators used in Stirling machines. GM coolers require additional oil removal equipment between the compressor and cold head to prevent oil from condensing in the cold region, a task typically performed by an adsorber which must be replaced every year or two. They tend to be large compared with other coolers of similar capacity but their reliability and cost have resulted in widespread use of GM coolers for a variety of applications, particularly where portability is not a concern. It seems unlikely that they will be adapted to miniature scales, largely due to the requirement of additional equipment for oil removal and the constraint placed on the operating frequency by the switching valve.

1.1.4 Joule-Thomson Cryocoolers

Joule-Thomson cryocoolers operate with steady flow and produce cooling by expanding a high pressure gas through a valve, orifice, or other flow restriction. This expansion occurs at constant enthalpy and for this reason they require working fluids exhibiting real gas behavior, i.e. enthalpy must be a function of pressure as well as

temperature. Using a gas mixture as a working fluid helps fulfill this requirement and significantly improves JT cooler performance [16]. The temperature drop resulting from the expansion is generally modest and therefore the recuperative heat exchanger must be very efficient in order to reach cryogenic temperatures. To operate at very low temperatures, Joule-Thomson refrigerators are often pre-cooled by other types of cryocoolers or staged in a cascade configuration. Other limitations of JT coolers include low efficiency in comparison with Stirling and pulse tube refrigerators and susceptibility of the orifice or other expansion passage to plugging. However, because JT coolers have no moving parts aside from the compressor, they are relatively straightforward to miniaturize. A recent paper by Lin [17] describes a miniature JT cooler with a 25 mm long by 0.61 mm diameter heat exchanger and 2mm square by 1.2 mm deep cold head. Using a mixed working fluid, a pressure ratio of 16:1, and a warm end pre-cooled to 240K this device achieved a steady cold temperature of 140K and very briefly reached 76K.

1.1.5 Reverse Brayton Cryocoolers

The throttling expansion process of the Joule-Thomson cryocooler neglects the potential of the high pressure gas to do work as it is expanded and is inherently less efficient than a reversible expansion process. Because it replaces the JT expansion orifice or valve with an expansion engine the reverse Brayton cryocooler has the potential to recover this lost work, resulting in improved efficiency. Because work is extracted during the expansion, cooling occurs even with an ideal gas as the working fluid. Although the reverse Brayton cooler schematic in Figure 1.1 shows a piston compressor and expansion

engine, rotary compressors and turboexpanders are more common and result in lower vibration export. Like JT coolers, they require very efficient recuperative heat exchangers to reach cryogenic temperatures; these heat exchangers are often the largest part of the Brayton cryocooler. Even with the improvement provided by the expansion engine, efficiencies are still generally lower than those of Stirling and pulse tube refrigerators. Relatively small reverse Brayton cryocoolers have been developed including long-life designs suitable for space applications; a notable example is the NICMOS cooler on the Hubble Space Telescope [18]. Miniaturization of the critical components (turbine compressor and expander, recuperative heat exchanger) of the reverse Brayton cooler has proven to be difficult so far and it seems unlikely that they may be miniaturized to the same scale as Stirling and pulse tube refrigerators.

1.1.6 Thermoelectric Coolers

Thermoelectric coolers (TEC) are solid state devices which move heat against a temperature gradient in response to an applied electrical current [19]. They have no moving parts and are easily scaled, but their efficiency is generally low compared to other refrigerators. The temperature difference developed across a single thermoelectric junction is dependent on the junction materials but is generally limited as well, to approximately 67 K for material combinations which are currently in common use. Larger temperature differences or better efficiency may be achieved by cascading several junctions in series, but the maximum temperature difference attainable is still limited [2]. For these reasons along with a lack of thermoelectric materials having suitable properties at cryogenic temperatures, TECs have yet to be employed for cryogenic cooling.

However, in anticipation of more suitable materials becoming available a cascade cryogenic thermoelectric cooler has recently been patented [20]. For now, TECs may compete with other miniaturized refrigerators for higher temperature applications [21] and serve as a performance baseline against which other devices may be measured [6,22].

1.2 Motivation and Scope of the Investigation

Cryocooling is an enabling technology for a wide variety of applications, many of which have only become practical as suitable cryocoolers became available. As an example, the development of reliable and efficient space cryocoolers has made possible compact and long-term military, commercial, and scientific space missions utilizing cryogenically cooled instruments [4]. Previously, such missions were limited by the size and lifetimes of the stored cryogen refrigeration systems which the space coolers have now mostly supplanted. Similarly, the development of miniature and microscale cryocoolers promises to enable a wide range of miniaturized sensors and faster, higher powered electronic devices.

The potential applications of miniature cryocoolers are numerous, and consequently there has been a great deal of research effort devoted to their development. A recent program by DARPA [23] has sought Micro Cryogenic Coolers (MCC) and associated hardware for targeted cooling of a long list of sensors, amplifiers, and other devices. The goals of this program include reducing the size of the cryocooler to the same scale as the device being cooled and removing impediments of size, weight, cost and complexity from the use of cryogenically cooled systems. Additionally, miniature

cryocoolers are desirable for space applications and portable devices due to their minimal size and weight. They might also be useful in a cascade configuration when small cooling loads must be carried at temperatures lower than that required by the primary load. In such an application, a larger cryocooler might carry the primary load while miniature stages carry the smaller, colder ones, improving the overall efficiency of the cooling system.

If the required cold temperature is increased beyond the traditional cryogenic range of 120 K and below, another set of potential applications for miniature cryocoolers emerges. Refrigeration of microprocessors, even just slightly below ambient temperatures, may result in increased speed, reliability, and lifetimes for these devices. Several authors have proposed small vapor compression refrigerators for this task [24,25] and thermoelectric coolers are an obvious option as well, but it seems quite feasible that miniaturized cryocoolers may eventually be competitive with these technologies [21,26]. Stirling and especially pulse tube coolers have advantages of mechanical simplicity over the vapor compression refrigerators and advantages of efficiency over TECs. This efficiency advantage may be critical, both for minimizing the overall power consumption of a cooled system and reducing the amount of heat which must ultimately be rejected by the device and thus the size of its ambient heat exchanger.

The work presented here focuses on the miniaturization of one type of cryocooler, the pulse tube refrigerator, although much of the discussion, results, and conclusions are also applicable to Stirling devices. Miniaturizing pulse tube refrigerators has been a subject of intense research interest for some time [6,27,28], and miniature PTRs have recently begun to be practically demonstrated [29]. It is still a matter of debate, however,

just how much miniaturization of pulse tube refrigerators will be possible. It is believed that certain physical processes, many of which are discussed in detail in the following chapter, will limit performance as the PTR size is reduced. It is likely that these loss mechanisms will impose a minimum size threshold below which they become practically insurmountable.

The development of miniature cryocoolers is likely to require directly applicable methods and tools for their design and analysis. Although such tools are available for large Stirling machines and PTRs, their applicability and accuracy for miniature systems is uncertain. It is in part due to this deficiency that the possible extent of PTRs miniaturization is still unclear. Broadly stated, the goals of this work are the improvement of design methods and tools applicable to miniature cryocoolers and the use of these tools to quantitatively estimate the effects of several of the previously mentioned phenomena expected to limit their performance. More specifically, investigations have been performed using available, state of the art analytical tools to scale conventional PTRs down to successively smaller sizes. Based on the expected operating conditions of the miniature PTRs, suitable regenerator and heat exchanger materials have been identified and experiments have been performed to determine their hydrodynamic parameters, important closure relations for cryocooler modeling. Computational Fluid Dynamics (CFD) models of both entire miniature PTRs and subsections containing their pulse tubes have been developed and utilized to quantitatively estimate the effects of various loss mechanisms and their dependencies on parameters such as system size, operating conditions, and material characteristics. The results of these models were then utilized for

a second scaling analysis, during which computational models of hypothetical PTRs much smaller than the current state of the art were produced.

CHAPTER 2

BACKGROUND

In this chapter many of the technical challenges and considerations involved in miniaturizing pulse tube refrigerators are discussed and reported results in the literature for miniaturized PTRs are reviewed. Additionally, several numerical modeling techniques commonly used for Stirling and pulse tube cryocoolers are described and their likely applicability to miniature devices is assessed.

2.1 Considerations for PTR Miniaturization

Successful miniaturization of pulse tube refrigerators will require comprehensive understanding of the impacts of their reduced scale on the physical phenomena which limit their performance. Many of the issues expected to complicate the miniaturization of pulse tube cryocoolers have been qualitatively identified [6,27,28,30,31] even though their effects and relative importance as the system size is reduced have not yet been quantitatively determined. These issues are reviewed in the following section and their ramifications for miniature PTR design are discussed.

2.1.1 Enhanced Axial Conduction

Because of their greatly reduced length scale, very large axial temperature gradients will exist for miniature PTRs. These gradients will drive axial heat conduction in the solid walls and regenerator matrix as well as in the working fluid. This direct heat transfer between the hot and cold ends of the PTR is a parasitic load which reduces the amount of useful refrigeration available; therefore, when designing miniature PTRs care must be taken to minimize it. The reduced diameters and cross sectional areas anticipated for miniature PTRs will help in this regard, and novel materials with reduced thermal conductivity for regenerators and structural components may also be useful for reducing these losses. Examples of such unconventional materials are the regenerator segmented by low therrmal conductivity layers described by Moran [31] and the PEEK walls of the pulse tube and regenerator of the miniature PTR reported by Garaway [30]. PEEK is a semicrystalline thermoplastic polymer which may be reinforced with glass fibers. It is relatively easy to machine, has a very low thermal conductivity, and has good mechanical and thermal expansion properties at cryogenic temperatures [32]. The drawback to using such a material is that it cannot be brazed and thus unconventional fabrication techniques must be used, which may make producing consistent hermetic seals in the PTC difficult.

2.1.2 Surface Effects and Periodic Flow in Miniature Components

Because of their smaller diameters or cross sections, miniature PTRs will have a higher surface area to volume ratio than their larger counterparts. Viscous dissipation losses, particularly in small connecting capillaries and inertance tubes, are therefore expected to become more significant as the sizes of these components are reduced. In the

pulse tube, where adiabatic compression, displacement, and expansion processes are desired, increased heat transfer between the working fluid and the walls may also occur. Nearly uniform flow in the pulse tube is also believed to be necessary for efficient cryocooling and this condition may be compromised by increased viscous drag from the pulse tube wall. These thermal and viscous losses are both expected to increase as the pulse tube diameter becomes smaller relative to the thermal and viscous boundary layer thicknesses.

Additionally, miniature PTRs may experience enhanced acoustic streaming losses resulting from increased thermal and viscous interactions between the working fluid and the pulse tube walls. The thermal and viscous penetration depths, δ_T and δ_V, and their magnitudes relative to the pulse tube diameter and wall thickness are important parameters for all of these phenomena [33]. The orders of magnitude of these are defined in Eq. 2.1 and 2.2, respectively. Frequency dependence of the boundary layer thicknesses enters the equations through ω, the angular frequency.

$$\delta_T \approx \sqrt{\frac{2k}{\omega \rho C_p}} \tag{2.1}$$

$$\delta_V \approx \sqrt{\frac{2\mu}{\omega \rho}} \tag{2.2}$$

Upon examination of these equations, it is apparent that for a given fluid and temperature, the boundary layer thicknesses may be reduced by increasing either the density, through an increase in mean pressure, or the frequency. As a result, miniature PTRs may be expected to operate at significantly higher frequency and fill pressure than conventional scale cryocoolers.

2.1.3 Enhanced Dead Volume

The ratio of the volume of connecting capillaries and other passive elements to the volume of the essential PTR components will likely be higher for miniature PTRs than for macro-scale ones. This extra fluid volume requires additional work input as it must be compressed each cycle but does not contribute to useful cooling, reducing the PTR efficiency. Beyond their own added dimensions, these volumes also make an extra contribution to the overall system size because in order to maintain a given pressure ratio the compressor swept volume, and likely the dimensions of the compressor itself, must be increased. In idealized models dead volumes may be minimized or even eliminated, but in physical devices they are often necessary for a variety of reasons. Separating the expander from the compressor is often desirable for system integration and vibration elimination, but it requires a transfer line. Likewise, instrumentation of PTRs is often done for performance monitoring, but connections for pressure transducers also add a small amount of dead volume which is likely to be more significant in a miniature device. Care should be taken to minimize these extra volumes for miniature PTRs and to only include them where absolutely necessary.

2.1.4 Regenerators

Miniature PTRs will require operation at significantly higher frequencies than the 50-60 Hz commonly used in conventional scale devices, placing interdependent constraints on the regenerator geometry, fill material, and charge pressure if efficient operation is to be maintained [28]. In order to maintain proper phase relationships across the regenerator and avoid overly high mass flow rates with their accompanying pressure

losses, the volume of the regenerator must decrease as the frequency increases. In order to maintain sufficient surface area for heat transfer, this decrease in regenerator volume must be accompanied by a decrease in the regenerator filler hydraulic diameter. Additionally, it is generally believed that for effective regeneration the pore or hydraulic diameter of the passages in the filler material must be smaller than the thermal penetration depth in the working fluid. However, these requirements place additional constraints on the operating conditions of miniature PTRs. Anticipated increases in fill pressure and frequency, needed to increase the power density for a given compressor displacement, also result in a decrease in thermal penetration depth; values of these operating parameters are therefore limited by the hydraulic diameter of the utilized porous regenerator filler. The finest conventional mesh screen regenerator filler which is readily available is #635 stainless steel mesh, having a wire diameter of 20.3 μm and a pore diameter of 20 μm. This material has been used in regenerators operating up to 300 Hz [34]. Conceivably, regenerators may operate at much higher frequencies and smaller sizes if materials having smaller hydrodynamic diameters can be produced.

An additional concern for miniaturized regenerators is that the ratio of the heat capacity of the regenerator matrix to that of the working fluid displaced in a cycle must remain relatively large. Simulations indicate that the performance of the regenerator will be significantly degraded if this ratio falls below about 50, although the decrease in performance is predicted to begin at ratios well above that [28]. This parameter is expected to become important due to the decrease in regenerator volume and increase in fill pressure previously stipulated for operation at higher frequencies, both of which tend to drive down the heat capacity ratio.

Finally, because of their reduced diameter the relative importance of gaps existing between the porous regenerator filler and the interior wall of the regenerator shell will likely be greater for miniature cryocoolers. Such a gap would exist for any regenerator using conventional mesh screen fillers and provide a low resistance flow path with a size on the order of a pore diameter which may decrease the effectiveness of the regenerator. For this reason and because of the need for smaller hydraulic diameters, many conventional regenerator fillers are not practical for miniature PTRs and it is quite possible that the use of MEMS fabricated or other innovative regenerators may be advantageous or even essential. Semiconductor fabrication techniques used with silicon [35] and micro-machining of metal fillers [36] have shown promise but the regenerators produced have been severely limited by high conductive losses. A novel approach involving offset layers and low thermal conductivity interfaces may help to reduce this parasitic load [31], but tests of this regenerator in a miniaturized stirling refrigerator failed to produce cooling [22]. This failure was likely due to the test device rather than the regenerator, however.

2.1.5 Phase Shifting Devices

Maintaining correct phase relationships between the oscillatory pressure and mass flow is critical to the efficient operation of pulse tube refrigerators. To minimize losses in the regenerator and maximize the heat lift, an approximate criterion is that the mass flow should be in phase with the pressure in the center of the regenerator, leading it at the warm end and lagging it at the cold end. This may be accomplished by a number of mechanisms as discussed in the previous chapter. In miniaturized PTRs, higher operating

frequencies and smaller dimensions may make it difficult to implement some of these phase shifting devices, however, and they may also behave differently than they do at the conventional scale. As an example, the reservoir has been eliminated altogether from a miniature PTR reported by Garaway; due to the cooler's high operating frequency and small tidal displacements, the volume of the inertance line was sufficient to perform the reservoir function [30].

Most of the common phase shifting devices have potential drawbacks for miniature PTRs. Precise control of orifice diameters or valve openings may become difficult as their dimensions are sufficiently decreased, and plugging of very small passages with contaminants becomes a potential issue as well. Additionally, orifices and valves can be significant sources of irreversibility and the efficiencies of orifice PTRs are generally lower than those of inertance tube PTRs. Miniature PTRs, however, are expected to operate with relatively low input powers and will need to be extremely efficient in order to reach cryogenic temperatures. Bypass lines can be very effective for phase control and have the added benefit of potentially reducing the mass flow through the regenerator and thereby reducing the regenerator pressure losses. Without precise control of their flow impedance, however, they can lead to circulating flow loops in a PTR which convect heat between the warm and cold ends. This impedance is often set with orifices or valves and therefore such control may be difficult as the system dimensions are reduced.

In the case of the inertance tube phase shifter, the required length appears to be a potential drawback as it seems incompatible with the construction of a very compact refrigerator. However, inertance tubes are generally coiled up and are often integrated

into the reservoir, reducing their contribution to the refrigerator's outer dimension. Furthermore, as the operating frequency of the PTR increases the optimal inertance length decreases, so the necessary length will scale down with the cryocooler. There are also fewer concerns with construction and blockages for an inertance tube and ITPTRs generally have the highest efficiency of the pulse tube refrigerators. For all of these reasons, inertance tubes are likely to be a good choice for miniaturized PTRs.

2.1.6 Compressors

The development of miniaturized compressors or pressure oscillators which can operate efficiently at high frequency will almost certainly be necessary for progress on miniature PTRs to continue and for their eventual maturation into practical, commercially viable cryocoolers. Many of the investigations reviewed in the following section used relatively large compressors operating at frequencies much higher than they were designed for while others likely failed partially for lack of a suitable compressor.

Several different approaches have been taken towards developing miniature pressure oscillators. Scaling down of linear or flexure bearing/Oxford type compressors has resulted in compressors capable of frequencies up to around 150 Hz with a swept volume under 1 cm^3 [9,37]. An effort has also been made at Virtual AeroSurface Technologies, in collaboration with Raytheon and Georgia Tech, to develop a similar long-life miniature compressor capable of operating at 300 Hz (T. Crittenden, personal communication). A second option is the use of piezoelectric drivers, which function easily at high frequencies and can produce relatively large forces. For these reasons they seem well suited for miniaturized pressure oscillators, but their displacement is limited.

To increase the swept volume, mechanisms which magnify their displacement can be used along with a deformable membrane [38], or other novel amplitude enhancing methods may be employed [39].

2.2 Review of Miniaturization Efforts

A number of papers regarding miniature pulse tube refrigerators have been published in the last several years and experimental results for devices of various scales have been reported. In 1996, Xu et al. reported reaching 160K with a coaxial DIPTR with a pulse tube diameter of 5 mm operating at 11 Hz and a mean pressure of 1.19 MPa [40]. The following year Curlier [41] reached ~90K with a concentric DIPTR having a total diameter of 10 mm as well as temperatures below 70K with a U-tube DIPTR having pulse tube and regenerator diameters of 5 mm. No details were provided regarding the operating conditions of these two cryocoolers. Similar results reported in the open literature include Liang et al. in 2000 [42] with a coaxial PTR of 9 mm total outside diameter capable of lifting 200 mW at 81 K and operating at 50 Hz, Tward et al. [43] in 2004 with a coaxial PTR operating at 65 K and 80 Hz, and Chen et al. in 2008 with a hybrid DIPTR/ITPTR reaching 50 K [44]. Despite the relatively small scale of these devices, their operating conditions are generally characteristic of classical scale PTRs and for this reason they may be more representative of the small end of the size range for conventional devices than actual miniaturized PTRs.

Further reductions in PTR scale will require comprehensively addressing the previously listed considerations affecting miniaturization. This has been recognized by

several authors and incorporated into a few devices at considerably smaller scales than those previously described, with various degrees of success. In 2004, Nika et al. identified and attempted to address several of the previously described issues in the course of constructing a miniature PTR with a 1 mm x 5 mm rectangular cross section using semiconductor fabrication techniques. Unfortunately, this device was limited to only 10-12 K of cooling, most likely by the 50 Hz maximum frequency limitation on its compressor and the high thermal conductivity of the silicon from which it was made [27]. In 2006 Radebaugh and O'Gallagher outlined criteria for very high frequency operation of regenerators for microcoolers [28]; this paper was followed in 2007 and 2008 by experimental demonstration of a small pulse tube expander operating at 3.5 MPa and 120 Hz [45,46]. The regenerator and pulse tube of this cooler were approximately 10 mm and 5 mm in diameter, respectively, and both were 30 mm in length. The compressor used in this work, however, was quite large, and with sufficient input power the cooler reached a no-load temperature of approximately 50 K.

Also in 2006, Garaway and Grossman performed a numerical study on high frequency oscillating compressible flow applied to miniaturized cryocoolers [47]. Building on this work in 2008, they listed several guidelines for designing a miniature pulse tube refrigerator which generally coincide with the considerations listed in the previous section. Incorporating these principles, they then presented results for a miniature linear PTR with 3.5 mm diameter and 12 mm length for both its regenerator and pulse tube. This PTR had a total volume of 2.3 cm^3, excluding the compressor, and reached 146 K operating at 128 Hz and a fill pressure of approximately 3.85 MPa [30]. This cooler had its pulse tube and regenerator walls constructed of PEEK, a material with

low thermal conductivity, to minimize conductive losses. This material also complicated the cooler assembly, however, and separate subsequent miniature PTRs reported by Garaway and Grossman have used more standard materials for these components. This PTR also utilized a novel inertance tube without a reservoir as its phase shifting device, although the successive coolers by both authors have also abandoned this configuration in favor of an inertance tube with a reservoir.

More recently in 2009, Garaway [29] adapted the miniature PTR previously developed by Radebaugh to use a high frequency miniature linear compressor made by Ricor. This cooler used a regenerator and pulse tube 27 and 40.4 mm in length and 4.5 and 2.1 mm in diameter, respectively, an operating frequency of 150 Hz, and fill pressure of 5 MPa. Although its compressor only achieved a pressure ratio of 1.17, far less than the 1.30 design point, this PTR reached a minimum temperature of 97.5 K. A subsequent re-optimization of this cooler for lower pressure ratios combined with the diagnosis and correction of unstable flow phenomena in its pulse tube led to increased performance [48], although a significant decrease in the minimum temperature attained was not reported. Additionally, Sobol, Katz, and Grossman [49] have presented simulated and experimental results for a miniature PTR which is a descendent of the cooler constructed by Garaway and Grossman. This device maintains the scale of the previous one but incorporates stainless steel pulse tube and regenerator walls and a stepped inertance tube with a reservoir. Operating at approximately 100 Hz and a fill pressure of 4 MPa, it reached a minimum temperature of 99 K and provided 400 mW of cooling at 110 K. Finally, while not explicitly discussing challenges related to miniaturization, a

continuation of the previously described work by Tward et al. extended the operation of that cooler to frequencies up to 144 Hz with improved performance [37].

2.3 Models and Design Tools for Miniature PTRs

As part of the ongoing research effort to improve the performance of cryocoolers, analytical and computational models of Stirling and pulse tube refrigerators have been developed with various degrees of sophistication. Application of any of these to miniature PTRs must be done carefully because some of the phenomena affecting the performance of PTRs at the miniature scale are likely to differ from those that are dominant at larger scales. The following paragraphs describe several common modeling approaches, their strengths and limitations, and their expected applicability to miniature PTRs. Examples of each model type are given and the Sage and Fluent programs used in this investigation are also introduced.

Analytical models of Stirling and pulse tube cryocoolers often involve control volume analysis [50] or the representation of cryocooler components with analogous electrical circuits [27,51]. In order to accurately represent actual systems, they need significant correction with empirical parameters. These models are good for providing information about parametric dependencies and have sometimes been applied as design tools, but their applicability to miniature PTRs is likely to be seriously limited. Both of these analytical approaches inherently neglect details of the flow inside their control volumes or analogous circuit elements, and knowledge of these flow details is necessary

for assessing the effects of several of the previously discussed phenomena likely to limit the performance of miniature PTRs.

A more detailed approach involves computational models which have been developed specifically for Stirling or pulse tube refrigerators. These models are generally one dimensional and based on solution of the differential fluid conservation equations at component boundaries and axially distributed nodes. They are therefore partially mechanistic models; however, like the analytical models, they require many empirical closure relations to obtain accurate results. Widely used models of this type include LANL's DeltaE [52], the REGEN code published by NIST [53], and Sage by Gedeon Associates [54], which will be utilized in this investigation.

Sage is a modular, hierarchical modeling program, with various sub-levels of models which can be assembled to represent almost any Stirling or pulse tube system. It is capable of very quickly solving for the steady-periodic performance of PTR's and includes tools for multidimensional optimization. Sage is limited, however, in that it cannot solve for time-dependent behavior and is one-dimensional, although it does include empirical corrections for some specific multi-dimensional effects. For larger scale systems, Sage has proven to be reliable and fairly accurate, particularly when its empirical corrections are based on directly relevant experimental results. Its direct applicability to miniature systems is unknown, however, and Sage does not include corrections for several of the phenomena expected to influence PTR performance at the miniature scale. In spite of these potential shortcomings, however, good agreement has been reported between Sage model results and experimental results for a miniature PTR by Sobol et. al. [49].

The modeling approach which appears most promising for miniature scale PTRs is the application of Computational Fluid Dynamics (CFD), a modeling technique widely used for a variety of problems. CFD based models solve the differential conservation equations for mass, momentum, and energy on a computational grid which is a discretized representation of the entire model domain, usually in two or three dimensions. Two dimensional axisymmetric models are most commonly used for PTR simulation. Depending on the solver used, additional capabilities such as turbulence models and the ability to represent deforming volumes are often included. The need for the additional detail which may be provided by these models has been recognized [55], and recent successful CFD simulations of entire cryocooler systems and selected components [56-61] have shown that such models can provide useful performance predictions for pulse tube refrigerators. All of these PTR simulations have been performed with Fluent, although other CFD solvers such as STAR-CD, CFD-ACE, and CAST have been used to perform Stirling engine simulations [55].

Fluent is a state of the art commercial CFD package capable of detailed solutions of models encompassing very complex geometries in two or three dimensions [62]. It is capable of obtaining either steady state or transient solutions to problems involving a variety of flow phenomena, including flow in porous media. Fluent may also be expanded using user defined functions (UDFs) in order to add or modify closure relations and incorporate custom boundary conditions. Because CFD models such as Fluent solve the governing conservation equations throughout the model domain, they do not include some of the simplifying approximations and assumptions which are present in dedicated PTR models, and therefore there may be more confidence about their applicability to

miniature systems. CFD models are also able to predict the complex flow details overlooked by one-dimensional models, likely improving their accuracy for miniature PTRs. For these reasons, CFD modeling is likely to be the most useful technique available for modeling miniature PTRs.

There are a few limitations, however, that come along with the advantages of CFD modeling. The models still need accurate closure relations and boundary conditions in order to produce meaningful results, particularly with regard to the hydrodynamic and thermal transport processes occurring in the porous segments of the PTR system. Additionally, the increased detail provided by CFD models is paid for with greatly increased computational time, and thus performing extensive parametric studies with CFD may be prohibitively time consuming.

CHAPTER 3

EXPERIMENTAL MEASUREMENT OF HYDRODYNAMIC PARAMETERS

This chapter describes experimental measurements of the directional hydrodynamic parameters of stacked discs of #635 stainless steel and #325 phosphor bronze wire mesh, two fine-mesh porous materials suitable for use in miniature PTRs. These experiments encompassed steady and oscillatory flows in predominantly axial and predominantly radial directions through samples of these two porous materials.

3.1 Background and Theory

Accurate CFD modeling of Stirling and pulse tube refrigerators requires realistic closure relations, particularly with respect to the hydrodynamic and thermal transport processes for the porous media which make up their heat exchangers and regenerators. The pressure drop and phase shift across the regenerator are both important parameters for efficient PTR operation and are dependent upon the hydrodynamic resistance of the regenerator porous filler. Experimental data and correlations have been published for some widely used filler materials suitable for large and small scale devices [63-68]. Generally, these porous media are morphologically anisotropic, and thus the parameters which characterize them are anisotropic as well. Measurement of the hydrodynamic parameters in at least two dimensions is therefore preferred. For the axisymmetrical

geometries commonly seen in Stirling and pulse tube refrigerators, a cylindrical coordinate system is convenient. Such coordinates are used in the experiments described in this chapter, in which the resistances to flow in the axial and radial directions are measured.

Because of the difficulty of directly simulating fluid flow in the microscopic passages of typical porous media, computational models often use empirical relationships to predict the macroscopic behavior of the fluid. Porous media are often anisotropic with randomly oriented elements and thus solutions for flow and heat transfer at the pore scale are generally unattainable. Under somewhat limiting conditions, however, direct pore level simulations have been performed [69-73]. Thus far, such simulations have remained too computationally demanding for direct incorporation into cryocooler models and have not necessarily been applicable to the oscillatory, compressible flow encountered therein.

The Fluent CFD code models porous media by applying modified conservation equations with empirical closure relations to porous zones. The general conservation equations solved by Fluent will be presented first, followed by their porous formulations [62]. Conservation of mass, momentum, and energy are displayed as Equations 3.1-3.3, respectively, below. Source terms S_m and S_h are included in the mass and energy conservation equations, although these are not incorporated in the models described in this work. The momentum equation includes gravitational body forces and a generic term representing all other body forces as its last two terms. In all of the models used in this investigation, gravitational forces are neglected. The generic body force term includes the momentum sink terms added by the porous media model in regions where it is enabled.

$$\frac{\partial \rho}{\partial t} + \nabla \cdot (\rho u) = S_m \tag{3.1}$$

$$\frac{\partial}{\partial t}(\rho \vec{u}) + \nabla \cdot (\rho \vec{u}\vec{u}) = -\nabla P + \nabla \cdot (\bar{\bar{\tau}}) + \rho \vec{g} + \vec{F} \tag{3.2}$$

$$\frac{\partial}{\partial t}(\rho e) + \nabla \cdot \left(\vec{u}(\rho e + P)\right) = \nabla \cdot \left(\mathrm{k_{eff}} \nabla \mathrm{T} - \sum_{\mathrm{j}} \mathrm{h_j J_j} + (\bar{\bar{\tau}}_{\mathrm{eff}} \cdot \vec{u})\right) + \mathrm{S_h} \tag{3.3}$$

Two different velocities are often defined for flow through porous media. The superficial or Darcy velocity is based on the volumetric flow rate and total cross sectional area, making it identical to the velocity outside the porous zones. In porous media, the presence of the solid phase decreases the flow area for a constant overall cross section; assuming constant density, conservation of mass then requires an increase in velocity in the fluid phase for a given mass flow rate. The physical velocity accounts for this decrease in flow area and more accurately depicts the actual fluid velocity in the porous zone. The two velocities are related by the porosity through the Dupuit-Forchheimer relationship, Equation 3.4. The porosity is the ratio of the open or void volume to the total volume of the porous material; it is defined in Equation 3.5. In these equations, $\vec{u}$ is the superficial velocity, $\vec{v}$ the physical velocity, and ε is the porosity. Because the porosity must by definition lie between 0 and 1, the magnitude of the physical velocity will always be greater than or equal to that of the superficial velocity.

$$\vec{u} = \varepsilon \vec{v} \tag{3.4}$$

$$\varepsilon = \frac{V_{void}}{V_{total}} \tag{3.5}$$

The modified conservation equations solved by Fluent for porous media are obtained from the general conservation equations through the addition of momentum sink terms with empirically determined coefficients to the momentum equation and the

alteration of the energy equation to include both solid and fluid phases, which are assumed to remain in thermal equilibrium. The added momentum sink terms are given in their most general form in Equation 3.6, where $\overline{\overline{D}}_{ij}$ and $\bar{\bar{C}}_{ij}$ are the viscous and inertial resistance tensors, respectively.

$$S_i = -\left(\sum_{j=1}^{3} \overline{\overline{D}}_{ij}\mu\vec{v}_j + \sum_{j=1}^{3} \bar{\bar{C}}_{ij}\frac{1}{2}\rho|\vec{v}|\vec{v}_j\right) \tag{3.6}$$

With the addition of this term to the right hand side of the momentum equation and the inclusion of the solid phase in the energy equation, the mass, momentum and energy conservation equations for porous media, as solved by Fluent, are given in Equations 3.7-3.9 respectively. These equations are recast in terms of the physical velocity and the diffusive enthalpy flux term $h_j J_j$ is omitted from the energy equation for the investigated case of a single component fluid.

$$\frac{\partial}{\partial t}(\varepsilon\rho) + \nabla\cdot(\varepsilon\rho\vec{v}) = 0 \tag{3.7}$$

$$\frac{\partial}{\partial t}(\varepsilon\rho\vec{v}) + \nabla\cdot(\varepsilon\rho\vec{v}\vec{v}) = -\varepsilon\nabla P + \nabla\cdot\left(\varepsilon\bar{\bar{\tau}}\right) + \varepsilon\vec{F}_{bf} - \mu\overline{\overline{D}}\cdot\vec{v} - \frac{\overline{\overline{C}}\rho}{2}\cdot|\vec{v}|\vec{v} \tag{3.8}$$

$$\frac{\partial}{\partial t}\left(\varepsilon\rho_f e_f + (1-\varepsilon)\rho_{sol}e_{sol}\right) + \nabla\cdot\left(\varepsilon\vec{v}\left(\rho_f e_f + P\right)\right) - \nabla\cdot\left(\left(\varepsilon k_f + (1-\varepsilon)k_{sol}\right)\nabla T + \bar{\bar{\tau}}\cdot\varepsilon\vec{v}\right) = 0 \tag{3.9}$$

Physical significance of the viscous and inertial resistance parameters is best described by analogy to simpler flow models. For the special case of steady, one dimensional flow with no body forces, the assumption that the convective acceleration

and viscous stress terms are small relative to the porous media viscous and inertial resistance terms can be made and Equation 3.8 can be directly compared to the classic Forchheimer equation through the pressure gradient term. This particular form of the momentum equation is given as Equation 3.10 and the Forchheimer equation is given as Equation 3.11 [74]. The Forchheimer equation is an extension of Darcy's law; the two terms on the right hand side of Equation 3.11 are often referred to as the Darcy and Forchheimer terms and are proportional to the velocity and the square of the velocity, respectively.

$$\varepsilon \frac{dP}{dx} = -\mu D v - \frac{C\rho}{2}|v|v \tag{3.10}$$

$$\frac{dP}{dx} = -\frac{\mu}{K}\varepsilon v - \frac{\rho c_f}{\sqrt{K}}\varepsilon^2 |v|v \tag{3.11}$$

In Equation 3.11, K is the Darcy permeability and c_f is Forchheimer's inertial coefficient. For one dimensional flow the viscous and inertial resistance tensors in Equation 3.10 become constants; in both equations ν is simply the magnitude of the physical velocity in the x direction. The bracket denoting magnitude is thus redundant but remains for easy comparison with Equation 3.8. Multiplying Equation 3.11 by the porosity and equating its right hand side with that of Equation 3.10, it is apparent that the Fluent viscous and inertial resistance terms are analogous to the Darcy and Forchheimer terms, respectively. The Darcy permeability and Forchheimer inertial coefficient may then be related to the Fluent viscous and inertial resistances through Equations 3.12 and 3.13.

$$K = \frac{\varepsilon^2}{D} \tag{3.12}$$

$$c_f = \frac{C\sqrt{K}}{2\varepsilon^3} \tag{3.13}$$

3.2 Experimental Methodology

Experiments were performed in order to determine the hydrodynamic parameters of stacked screens of #635 stainless steel and #325 phosphor bronze wire meshes in the axial and radial flow directions for both steady and oscillatory flow regimes. Hydrodynamic parameters related to the Darcy permeability and Forchheimer inertial coefficient were obtained from the experimental data using a CFD-assisted methodology which was implemented in Fluent, a widely used commercial CFD code. Measurements were made of fluid mass flow rate and pressure drop across each porous sample for the steady flow cases. Likewise, for the oscillatory flow cases pressure waveforms were recorded at either end of each sample for a range of operating frequencies. Each experimental apparatus was then simulated with Fluent and the model viscous and inertial resistances were iteratively adjusted to produce agreement between the simulated and experimental results. This methodology was proposed by Harvey [63] and further developed by Cha [65] and Clearman [64]. Additional details of the experiments described in this chapter are given by Landrum [66], and the results are also published in [75].

The methodology common to all of the performed experiments will be described in this section, while details specific to a particular flow regime or direction will be given in the following subsections. For each of the tests, the apparatus was purged of air and

other contaminants and filled with research grade helium. Leak testing was performed and experiments were conducted only after verifying that the apparatus was hermetically sealed. For the steady flow apparatus, which was vented to the atmosphere during experiments, leak testing was performed up to the downstream valve. All testing was conducted at ambient temperatures of approximately 300 K.

The #635 stainless steel and #325 phosphor bronze mesh materials are commercially available and were purchased from TWP Inc. They are plain square weave meshes, woven in a simple over and under pattern with square openings; the leading number (e.g. #635) describes the number of parallel wires per inch. Wire diameters and hydraulic diameters of these materials and porosities for the tested samples are given in Table 3.1. The axial samples were made up of stacked screen discs 4 mm in diameter while the radial samples utilized stacked annular screens with inner and outer diameters of 4 mm and 20 mm, respectively. The screens were punched individually as this process was found to produce cleaner and more circular edges than EDM cutting or punching of multiple layers at once; representative screens are shown in Figure 3.1 and magnified views of the #635 stainless steel mesh are shown in Figure 3.2.

Table 3.1 Wire mesh characteristics and sample geometry

Porous Media	Sample Geometry			Mesh Geometry		Measured
	ID mm	OD mm	Length [mm]	Wire Dia μm	Pore Size μm	Porosity ---
Axial Samples						
325 Phosphor Bronze	N/A	4	12.7	35.6	43	0.6738
635 Stainless Steel	N/A	4	12.7	20.3	20	0.6312
Radial Samples						
325 Phosphor Bronze	4	20	3.4	35.6	43	0.6702
635 Stainless Steel	4	20	6.1	20.3	20	0.6304

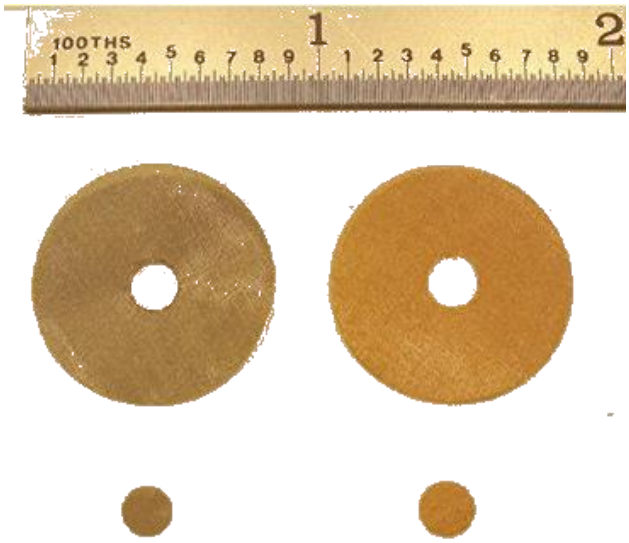

Figure 3.1 Photograph of punched wire mesh screens

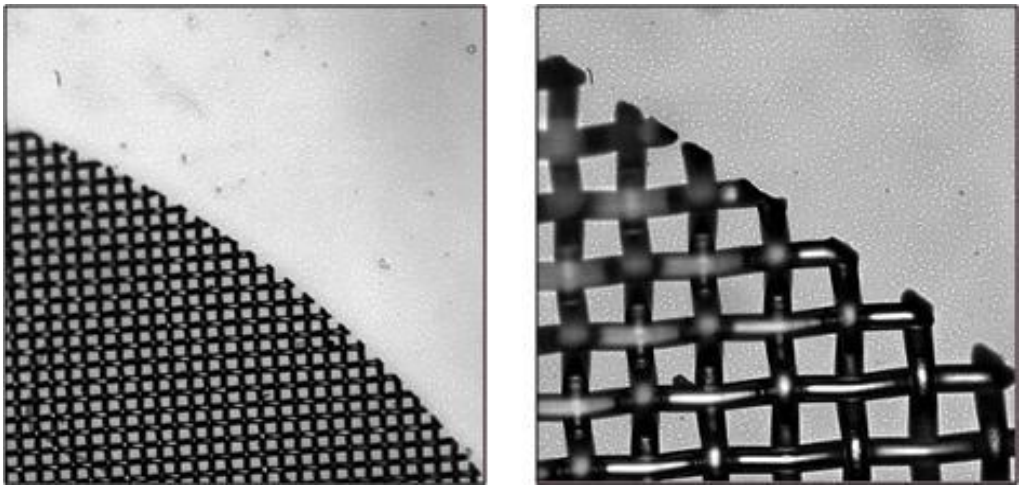

Figure 3.2 Magnified views, punched #635 stainless steel wire mesh screen

3.2.1 Steady Flow Methodology

Schematics of the closely related apparatuses for the steady axial flow and steady radial flow experiments are shown in Figure 3.3 and Figure 3.4, respectively. In both cases, a helium cylinder and pressure regulator provided a steady supply pressure and static pressure transducers were positioned upstream and downstream of the porous samples. A mass flow meter (Sierra Instruments, TopTrak model 826) was positioned downstream of the final control valve, which throttled the helium in order to regulate the mass flow rate. This positioning of the mass flow meter allowed it to make measurements at essentially atmospheric pressure, its calibration condition. The mass flow meter had a range of 0~1.5 g/s with an accuracy of +/- 1.5% of full scale. The pressure transducers (Paine Electronics, series 210-10) had an accuracy of +/- 0.35% of full scale with a range of 0~3.45 MPa. Each transducer's output was amplified by a signal conditioner (Omega DMD-465WB), the output of which was calibrated before each experiment using a dial pressure gauge as a reference. Analog voltage outputs of each instrument were read using handheld digital multimeters.

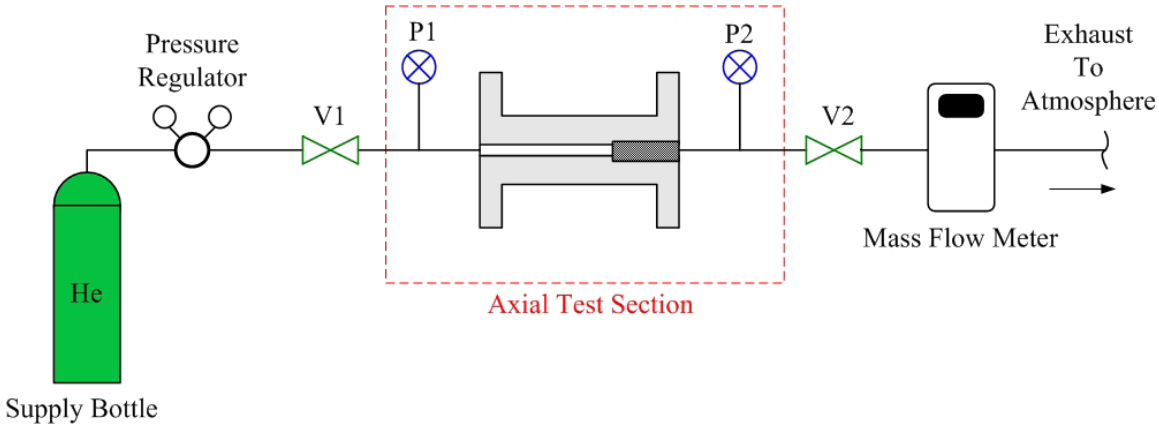

Figure 3.3 Schematic of steady axial flow test apparatus

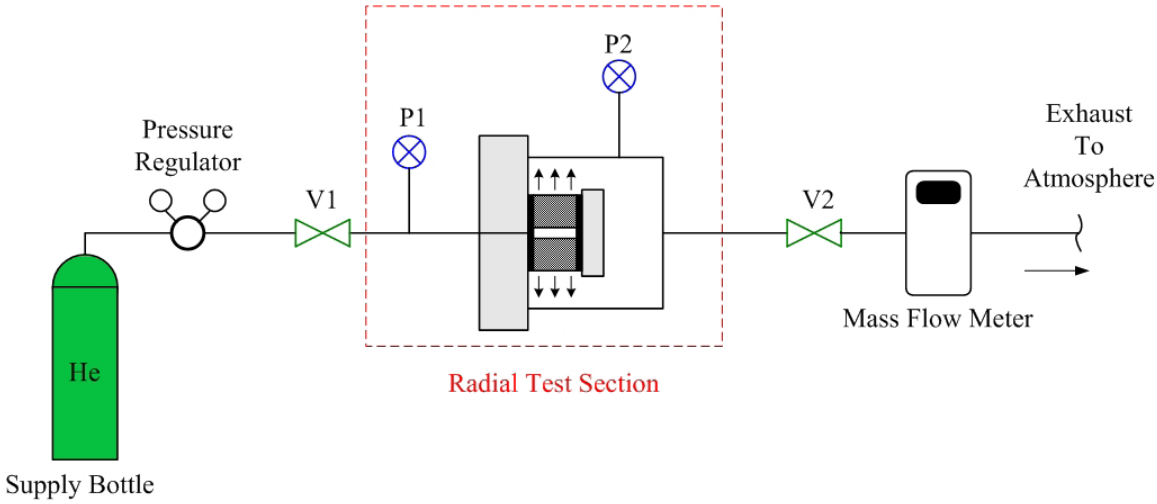

Figure 3.4 Schematic of steady radial flow test apparatus

The steady axial flow and steady radial flow experiments used separate porous samples, the geometry and porosity of which are given in Table 3.1. The axial samples were circular discs, randomly packed into a cylindrical housing, while the radial samples were annular discs which were randomly stacked and then compressed to the desired porosity using threaded rods and a top plate. For the axial samples, firm pressure was applied as consistently as possible to each screen during this procedure in order to maintain a high packing density. An effort was made to make the porosities of the axial and radial samples for each material match as closely as possible.

The section of the axial flow apparatus which housed the porous sample was a hollow aluminum cylinder with a step change from 2.0 mm to 4.013 mm in its inner diameter. The porous sample was held in place in the larger diameter section by the step and the mating face of the adjoining end piece. The test sample and housing were designed with a relatively large aspect ratio (length-to-diameter ratio) of 3.2 to ensure that the flow within the porous structure was predominately in the axial direction. Strict

tolerances used in fabrication ensured a negligible clearance between the stacked screens and the test section's inner diameter. A photograph of this part of the apparatus, showing the test section and static pressure transducers, is displayed in Figure 3.5.

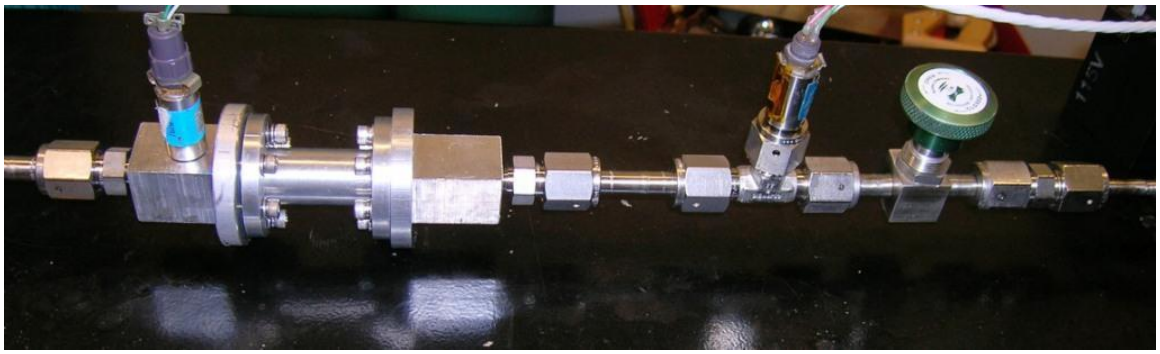

Figure 3.5 Photograph of axial flow test apparatus

In the radial flow apparatus, the porous samples were housed in a cylindrical shell with an inner diameter and length much greater than those of the samples. Flow entered the inner passage of the annular samples through an inlet having a diameter less than the inner diameter of the sample. This arrangement ensured that the flow direction through the sample was predominantly radial. An aluminum end cap, attached with three threaded rods, held the samples against the face of the housing unit inlet. By adjusting sample length using the cap and threaded rods, the porosity of the sample could be specified. Thin rubber discs were placed between the screens and both the housing face and end cap to eliminate the possibility of low-resistance flow paths at these locations. Figure 3.6 shows a photograph of a radial flow sample mounted in the housing unit with the outer shell removed.

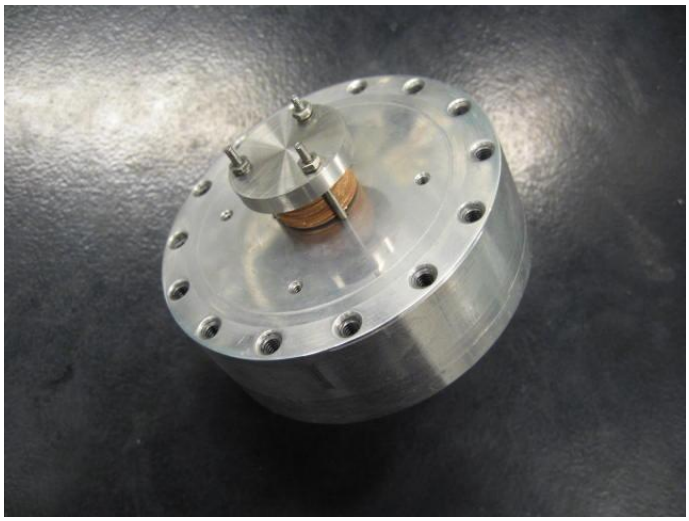

Figure 3.6 Photograph of #325 phosphor bronze radial flow sample mounted in test apparatus

Identical procedures were used for steady flow testing in both axial and radial directions. Tests began with the upstream valve, V1, fully open and the downstream valve, V2, closed. The system was pressurized to the nominal test pressure by adjusting the regulator, then valve V2 was slowly opened allowing helium to flow through the test section. By careful adjustment of V2 the mass flow rate through the test section could be controlled. For each test, the mass flow rate was swept up to its maximum value and then swept back down again until V2 was closed. Pressure data from the upstream and downstream pressure transducers P1 and P2, respectively, and the mass flow rate were recorded at discrete points after waiting a short time for the instrument outputs to stabilize. The maximum mass flow rate was generally 1.5 g/s, although a maximum allowable pressure drop of 0.7 MPa was also imposed which limited the mass flow rate to lower values in some cases. This restriction on the pressure drop prevented large density variations in the sample and resulted in more accurate and relevant determination of the sample hydrodynamic parameters [76]. Experiments were performed with a charge

pressure of 2.76 MPa and were repeated multiple times for each material, charge pressure, and flow direction.

3.2.2. Oscillatory Flow Methodology

Schematics of the oscillatory axial flow and oscillatory radial flow apparatuses are shown in Figure 3.7 and Figure 3.8, respectively. Both experiments utilized a Stirling type compressor (Hughes Aircraft Condor) driven by an amplifier (Crown DC-300A series II) and a function generator (HP-Agilent 33120A). A transformer, not shown, was included between the amplifier and compressor to better match the output of the amplifier to the electrical impedance of the compressor. Two high frequency dynamic pressure transducers (PCB Piezotronics 101A05) having a resolution of 0.014 kPa were also utilized, along with a data acquisition and control unit (HP-Agilent 3852A) which recorded their outputs and provided input to the function generator. The oscillatory flow apparatuses used the same wire mesh samples and housings as the steady flow experiments, with changes made only to the end pieces and mounting brackets in order to incorporate the dynamic pressure sensors. The sample geometries are shown in Table 3.1 in the previous subsection. Before performing experiments, each apparatus was purged of air and then charged to a specified mean pressure with research grade helium from a high pressure cylinder and regulator, not shown in the schematics. The valve V1 was then closed, leak testing was performed, and experiments were then conducted with the system closed.

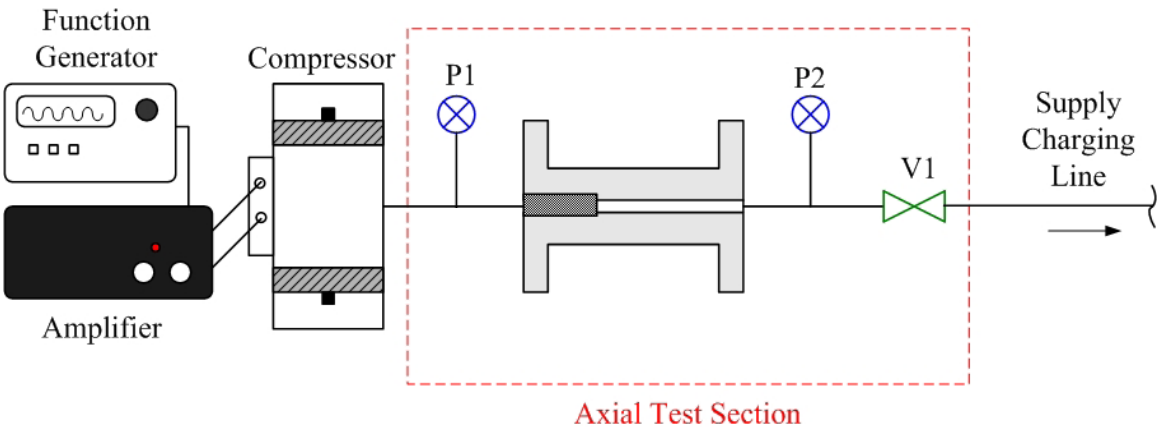

Figure 3.7 Schematic of oscillatory axial flow apparatus

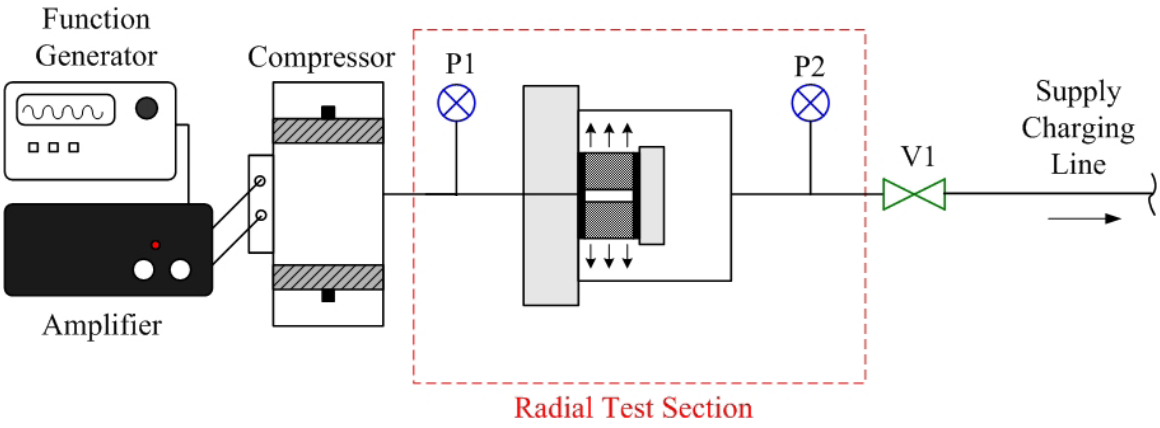

Figure 3.8 Schematic of oscillatory radial flow test apparatus

During the oscillatory flow experiments, a sinusoidal input was provided to the compressor by the function generator and amplifier at 7 discrete frequencies from 50 to 200 Hz, spaced at 25 Hz intervals. Oscillatory flow testing was performed at two mean pressures, 2.8 and 3.5 MPa. Both the selected pressures and driving frequencies are high relative to those typical for conventional scale cryocoolers but are expected to be more applicable to miniature PTRs. Pressure waveforms measured by each dynamic pressure transducer were recorded along with a Fast Fourier Transform (FFT) representation of the first three harmonics, based on the compressor drive frequency. This representation is

shown in Equation 3.14, where Z_j are the amplitudes and ϕ_j are the phases of each harmonic.

$$P_{osc} = Z_1 \cos(\omega t + \phi_1) + Z_2 \cos(2\omega t + \phi_2) + Z_3 \cos(3\omega t + \phi_3) \tag{3.14}$$

For each flow direction and charge pressure, data for a low oscillatory mass flow rate was obtained first at 50 Hz by reducing the amplifier gain so that the oscillatory pressure amplitude measured at P1 was relatively small. This low flow rate case was later used to more easily determine the viscous resistance of the porous sample. Subsequently, measurements were taken for each driving frequency with the amplifier gain increased to the point where the compressor maximum displacement or the amplifier maximum current was reached. These higher flow rate data were later used to determine the sample's inertial resistance.

3.2.3 Computational Analysis

In order to determine hydrodynamic parameters characteristic of the tested wire mesh samples from the experimental data, the test sections were modeled with the Fluent CFD code. Two-dimensional, axisymmetric representations of each experimental apparatus were constructed and the model hydrodynamic parameters were iteratively adjusted until agreement was reached between the simulation results and the experimental data. Grid independence of the simulated results was ensured by solving selected cases for each modeled apparatus using multiple computational grids with increasingly refined mesh spacing. Meshes possessing the lowest cell counts while still producing results essentially unchanged from finer mesh schemes were subsequently

employed for the determination of the sample parameters. Typically, variations in simulated pressure amplitude of less than 1% when the mesh spacing was halved were considered negligible. Time steps were selected for the oscillatory flow simulations such that there were at least 190 steps per period of the fundamental harmonic of the user defined pressure inlet function. The independence of the solution on the time step was also ensured by performing simulations with the time step halved for a limited number of cases, which resulted in changes of less than 0.2% in the simulated pressure amplitudes.

For the steady and oscillatory axial cases, identical computational grids were used for the #635 stainless steel and #325 phosphor bronze wire meshes. However, the radial cases used slightly different grids for the two materials to account for the differences in sample length, described in Table 3.1. In the radial flow models, the rubber gaskets and threaded rods in the experimental apparatus were excluded from the CFD analysis, but the end cap constraining the sample was included and treated as an adiabatic wall.

In all of the simulations, the helium was modeled as an ideal gas, gravitational body forces were neglected, and all walls were modeled as smooth, adiabatic surfaces. Model parameters such as first or second order discretization techniques and pressure-velocity coupling methods were chosen for each setup to offer the best residual convergence. A universal set of convergence criteria was applied to all simulations that restricted residual values to less than 1E-7. The Fluent porous media model, which solves the equations described in section 3.1, was utilized for the zones representing the porous samples. For steady flow through porous media, transition from laminar to turbulent flow occurs at $\mathrm{Re}_k \approx 350$ [77]. By this criterion, the majority of the flows in the performed experiments were in the laminar regime, and laminar models were therefore applied for

most of the simulations. However, for some steady axial flow experiments this Reynolds number was exceeded and therefore the standard k-epsilon turbulence model was applied for these cases. Laminar flow models were used for all of the oscillatory flow cases.

The Fluent porous media model utilizes input values for directional viscous and inertial resistance coefficients. For each case, these values were iteratively adjusted until the simulation's predicted output variables matched those measured experimentally. For the steady flow cases, the mass flow rate and outlet pressure were inputs for the models and the resistance parameters were adjusted until the simulated inlet pressure matched the experimental value. For the oscillatory cases, the FFT representation of the inlet pressure was supplied as a boundary condition to the model by way of a Fluent user defined function (udf). The viscous and inertial resistance parameters were then adjusted to match both the amplitude of the simulated pressure waveform at the location of the second pressure transducer, P2, and its phase relative to the inlet waveform. Further description of the steady and oscillatory flow simulations is given in the following paragraphs.

From the steady flow experimental data, polynomial curve fitting was used to obtain expressions for the pressure drop as a function of the mass flow rate for each wire mesh material and flow direction. Seven representative data points from each of these curves were chosen for CFD analysis and a single steady flow case was generated for each one. For the steady flow cases, the CFD models encompassed each experimental apparatus from the mounting point of the inlet static pressure transducer, P1, to the mounting point of the outlet transducer, P2. Starting with the case for the lowest selected mass flow rate, solutions to the models were obtained with guessed hydrodynamic parameters, which were then iteratively adjusted until agreement with the experimental

data was reached. At the lowest mass flow conditions inertial effects, proportional to the velocity squared, are small and viscous effects, proportional to the velocity, dominate; therefore, the viscous resistance coefficient may be more easily determined from the low mass flow rate cases. The inertial resistance coefficient may then be determined, also through iterative adjustment, from the higher mass flow rate cases.

From the oscillatory flow data, individual models were constructed for each frequency, wire mesh material, and mean pressure for which experiments were performed, as well as for the 50 Hz low flow tests. The oscillatory models had their inlets at the mounting locations of the dynamic pressure transducers labeled P1 in their schematics, but their domains extended past the second pressure transducer mount to the valves V1 which closed off these systems. These valves were represented as walls in the CFD models. Each case was iterated with the transient solver for ten periods of the fundamental frequency of the harmonic input pressure function, at which point an essentially steady-periodic state had been reached. Iterative adjustment of the model viscous and inertial resistance parameters was then made and simulations repeated until the simulated pressure amplitude and phase at the P2 location matched the experimentally measured pressure waveform there. As was the case for the steady flow simulations, the viscous resistance was initially determined at low mass flow conditions where viscous effects were dominant using the 50 Hz low flow case. Here approximate viscous resistance coefficients were determined, although unlike for the steady flow cases these were adjusted along with the inertial resistance coefficients in the higher flow rate cases in order to produce the best agreement possible between the simulated and experimental results.

3.3 Results and Discussion

3.3.1 Steady Flow

The experimentally measured and simulated pressure drops are plotted against the mass flow rate in Figure 3.9 for the axial flow direction and in Figure 3.10 for the radial flow direction. These figures were presented earlier in [66,75].The error bars represent the uncertainty in the experimental measurements. For the radial flow experiments, the uncertainty in the measured pressure is relatively large because the measured pressure differentials were small. This was a result of the small size of the porous sample; due to the expense of the wire cloth material, particularly the #635 stainless steel mesh, small sample dimensions were initially chosen. In hindsight, a sample with a larger outside diameter would most likely facilitate more precise determination of the radial hydrodynamic parameters. In spite of this, steady flow results in both the axial and radial flow directions were quite reproducible; each plotted data series incorporates several increasing and decreasing sweeps of the mass flow rate.

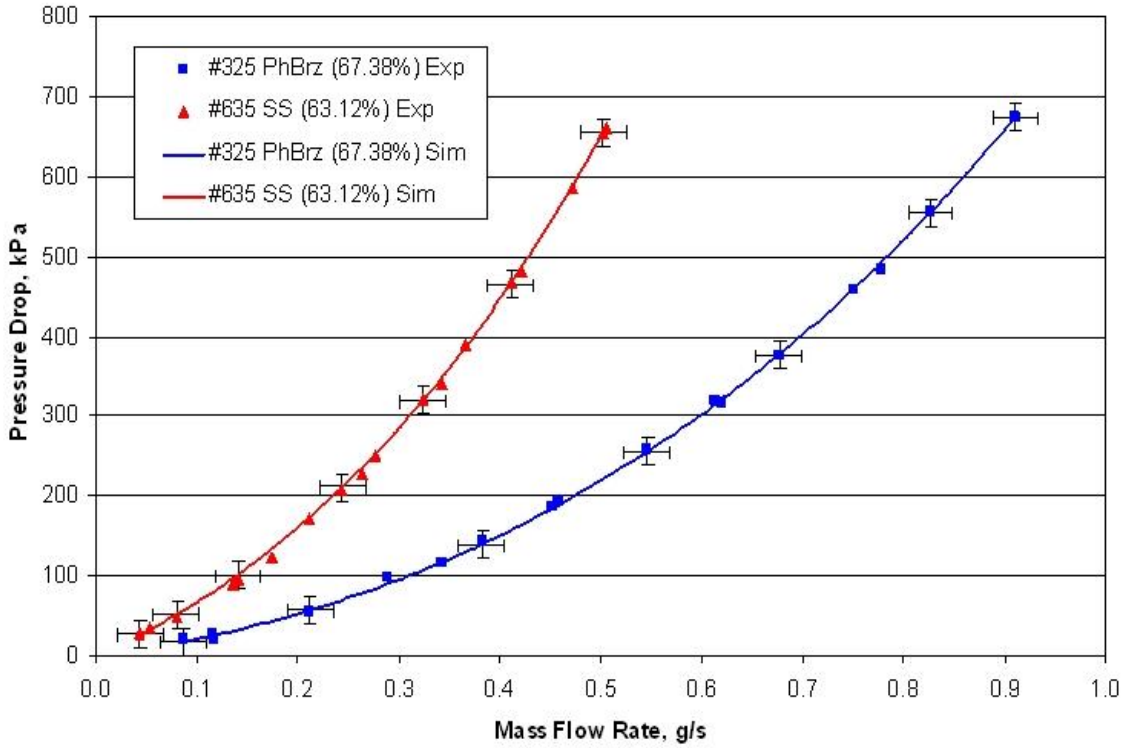

Figure 3.9 Pressure drop vs. mass flow rate, steady axial flow

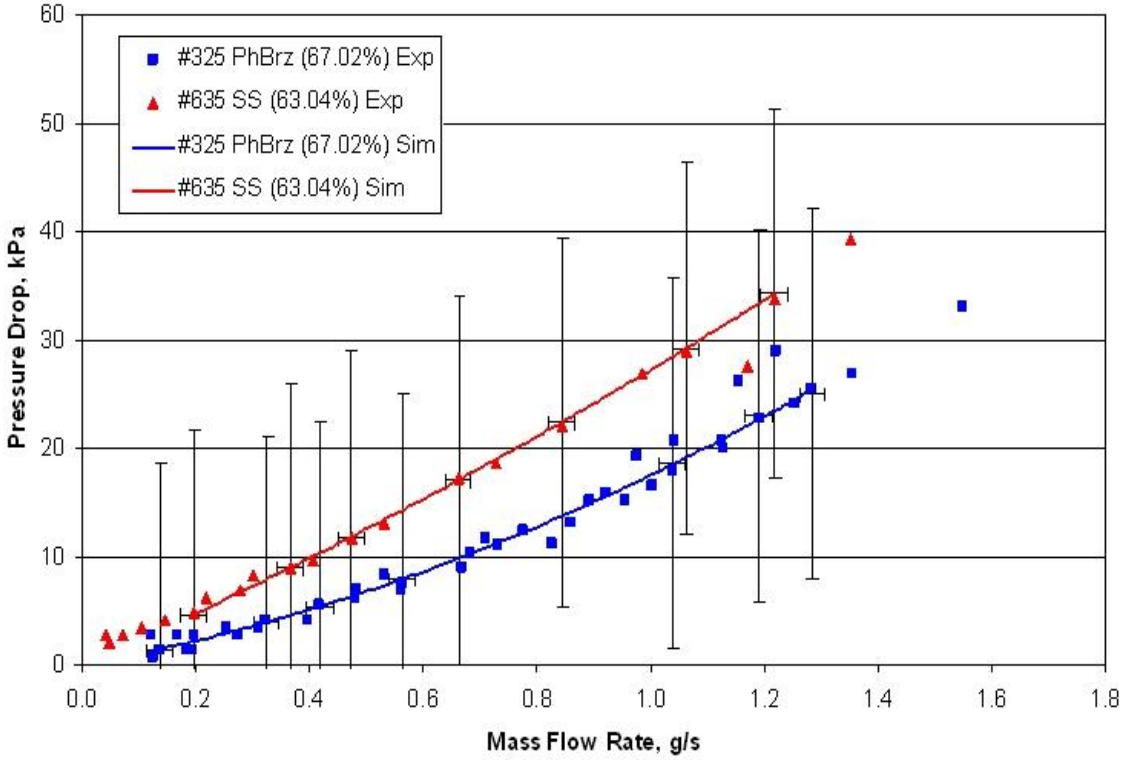

Figure 3.10 Pressure drop vs. mass flow rate, steady radial flow

Following the procedures detailed in section 3.2, steady flow hydrodynamic parameters were determined for stacked screens of both #635 stainless steel and #325 phosphor bronze wire meshes in the axial and radial directions. These parameters are tabulated in Table 3.2. As expected, anisotropic viscous and inertial resistances are seen, although this is more pronounced for the #325 phosphor bronze than the #635 stainless steel. Confidence intervals for the parameters in Table 3.2 are estimated based upon the scatter observed in the measured data.

Table 3.2 Steady flow hydrodynamic parameters

Porous Media	Measured Porosity [-]	Viscous Resistance Coefficient [m^{-2}]	Inertial Resistance Coefficient [m^{-1}]	Darcy Permeability [m^2]	Forchheimer's Coefficient [-]
Axial Samples					
#325 Phosphor Bronze	0.6738	2.85±0.3 E+10	27500±1500	1.593±0.17 E-11	0.179±0.014
#635 Stainless Steel	0.6312	9.95±0.4 E+10	69000±3000	4.004±0.16 E-12	0.275±0.013
Radial Samples					
#325 Phosphor Bronze	0.6702	2.85±0.5 E+10	58000±7000	1.576±0.29 E-11	0.382±0.057
#635 Stainless Steel	0.6304	1.24±0.1 E+11	59000±5000	3.205±0.26 E-12	0.211±0.057

To ensure the accuracy of the directional hydrodynamic parameters determined in this investigation, it was verified that the simulated flow through the porous samples was predominantly one dimensional and that the pressure drop across the porous samples was much larger than any other changes in pressure occurring elsewhere in the test apparatus. Figure 3.11 and Figure 3.12 show simulated contours of pressure and simulated velocity vectors, respectively, for the steady axial flow experiments. The same quantities are shown for the steady radial flow experiments in Figure 3.13 and Figure 3.14.

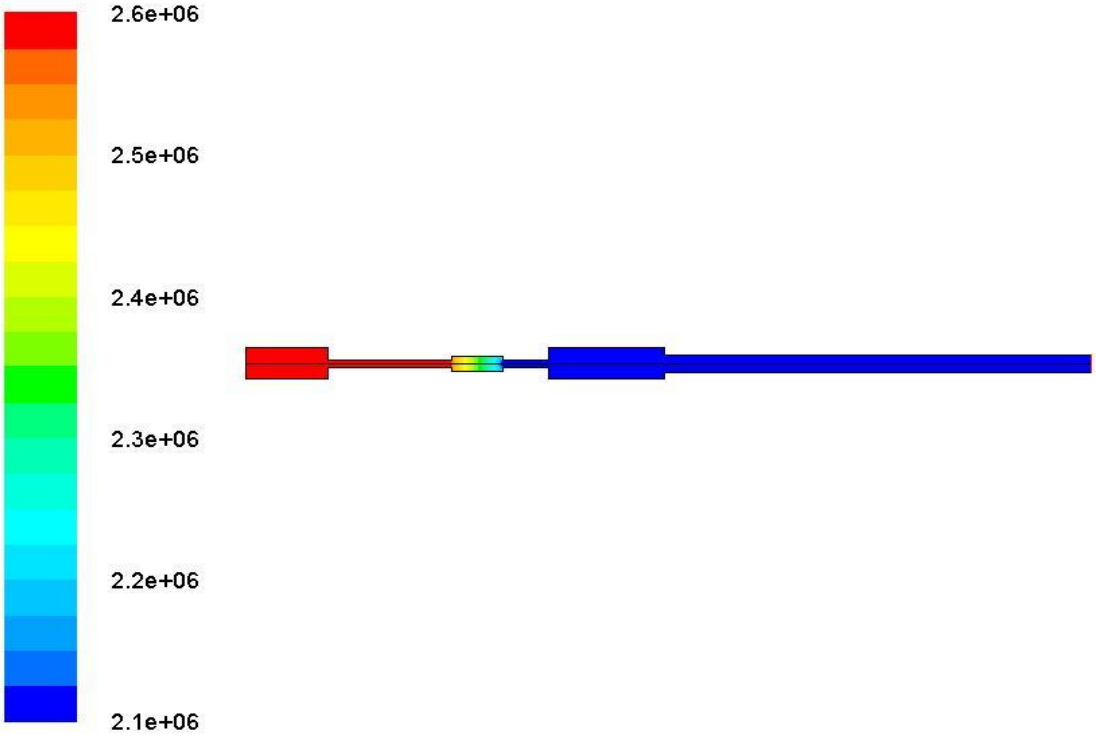

Figure 3.11 Simulated contours of static pressure, steady axial flow

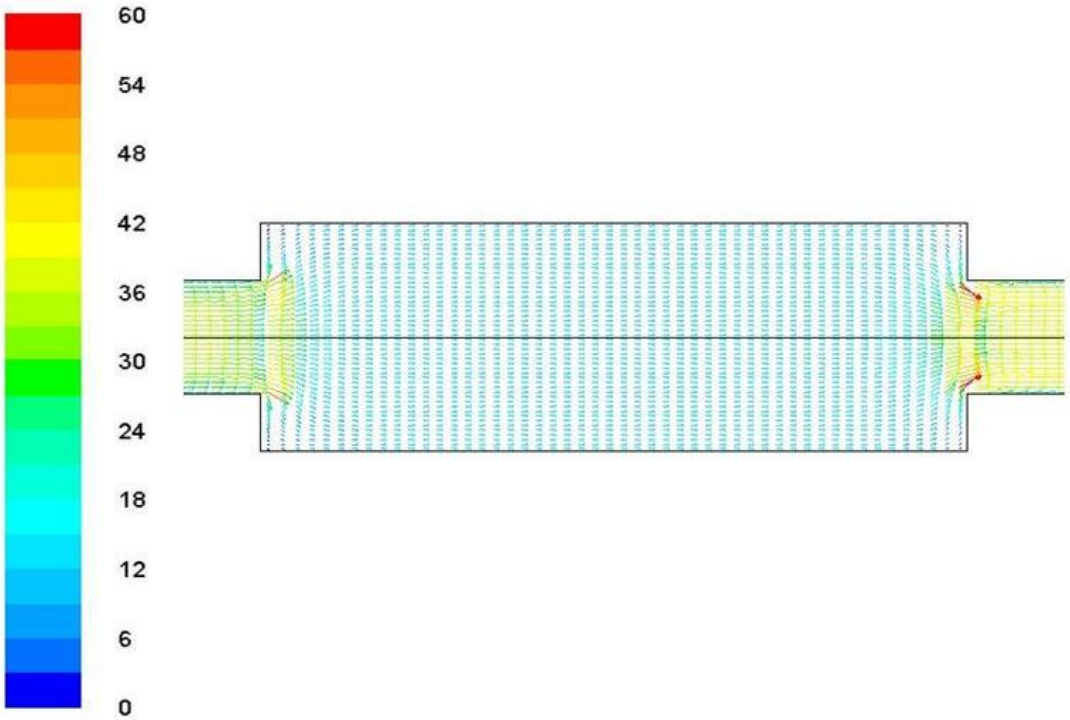

Figure 3.12 Simulated velocity vectors, steady axial flow

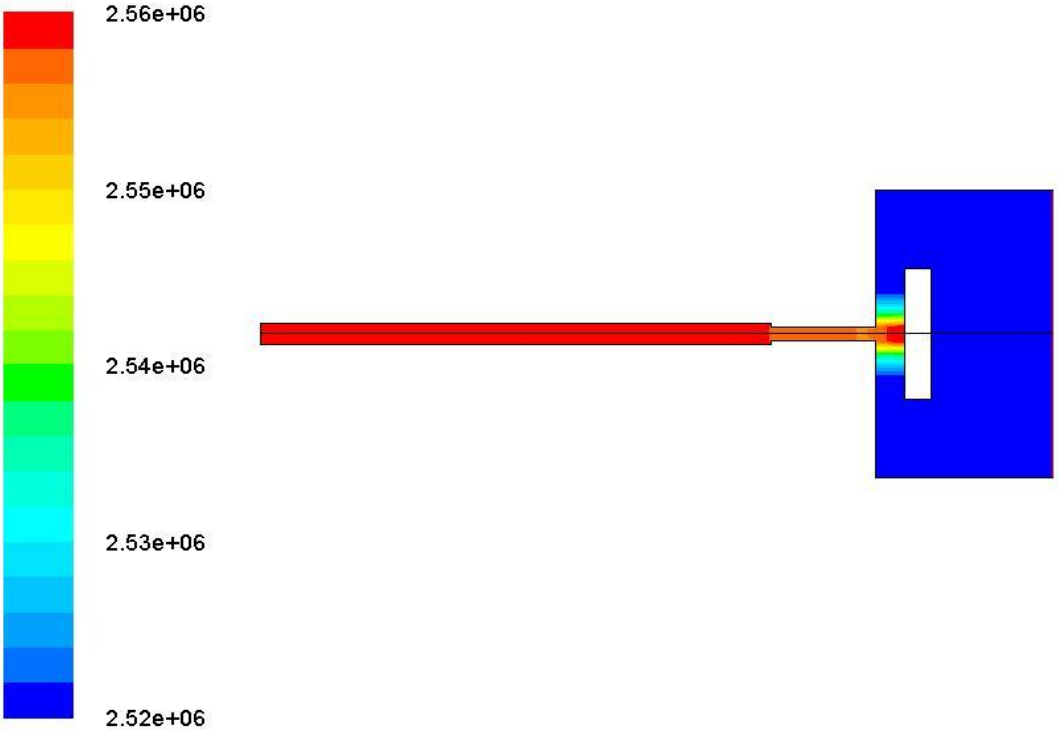

Figure 3.13 Simulated contours of static pressure, steady radial flow

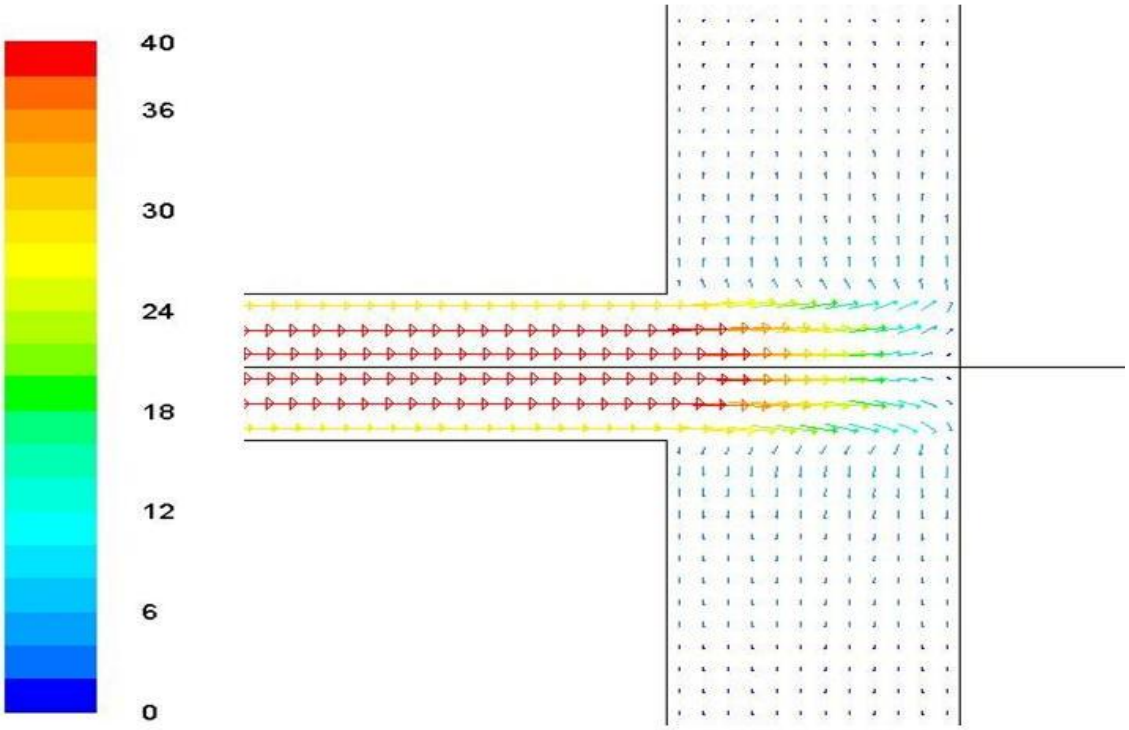

Figure 3.14 Simulated velocity vectors, steady radial flow

From these figures it is apparent that the simulated pressure drops occur almost entirely in the porous regions of the test section models. Additionally, in the axial flow model the simulated velocity vectors are predominantly axial and in the radial flow model they are predominantly radial throughout the porous zone. For these reasons, there may be confidence that the hydrodynamic parameters determined using this methodology are truly directional and that effects of the flow outside of the samples do not contribute significantly to the parameter values.

3.3.2. Oscillatory Flow

Following the previously described methodology, the oscillatory flow experimental data was used to determine hydrodynamic parameters for oscillatory axial flow and oscillatory radial flow in the two tested porous fillers at each of the two charge pressures utilized in the experiments. In each instance, a single set of parameters was determined which provided the best fit over the tested frequency range of 50 – 200 Hz. An additional attempt has been made to resolve hydrodynamic parameters individually for each frequency, but this was hampered by the very limited pressure amplitude supplied by the compressor at the higher frequencies and the results were generally inconclusive [78].

The experimental and simulated results were compared graphically and quantitatively using a matlab code which is reproduced in Appendix A. A sample plot displaying experimental and simulated results is shown in Figure 3.15, which was presented earlier in [66,75]; a comprehensive set of these figures is available in [66]. In

Figure 3.15 it is apparent that there is excellent agreement between the simulated and experimentally measured pressure waveforms.

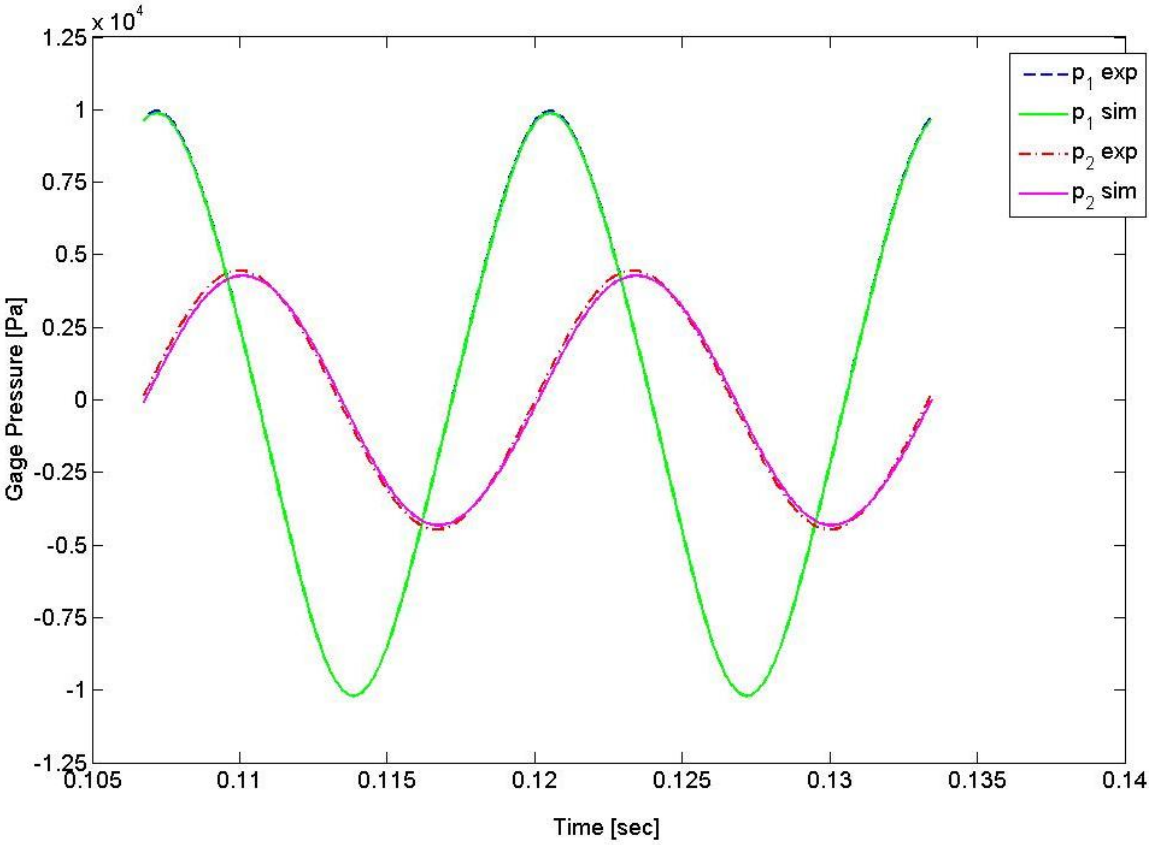

Figure 3.15 Typical oscillatory flow experimental and simulated waveforms, #635 stainless steel, radial flow at 75 Hz, 3.5 MPa

The hydrodynamic parameters determined by this methodology for each material, mean pressure, and flow direction are displayed in Table 3.3. Confidence intervals for these oscillatory cases were estimated based upon the range of parameters providing reasonably good agreement between simulated and experimental result. For this set of hydrodynamic paramaters, the average errors between the simulated and experimentally measured pressure amplitudes at P2 were 3.7% and 3.5% for the axial and radial flow

directions, respectively. Average errors in the phase angle between P1 and P2 were 1.48 and 1.43 degrees for the axial and radial flow directions, respectively.

Table 3.3 Oscillatory flow hydrodynamic parameters

Porous Media	Charge Pressure [MPa]	Viscous Resistance coefficient [m^{-2}]	Inertial Resistance coefficient [m^{-1}]	Darcy Permeability [m^2]	Forchheimer's Coefficient [-]
Axial Samples					
#325 PhBrz (67.38%)	2.8	1.70±0.2 E+10	50000±6000	2.672±0.32 E-11	0.422±0.056
#325 PhBrz (67.38%)	3.5	1.70±0.2 E+10	50000±6000	2.672±0.32 E-11	0.422±0.056
#635 SS (63.12%)	2.8	9.50±0.2 E+10	40000±5000	4.194±0.08 E-12	0.163±0.020
#635 SS (63.12%)	3.5	9.50±0.2 E+10	40000±5000	4.194±0.08 E-12	0.163±0.020
Radial Samples					
#325 PhBrz (67.02%)	2.8	2.90±0.2 E+10	50000±10000	1.549±0.11 E-11	0.327±0.066
#325 PhBrz (67.02%)	3.5	2.90±0.2 E+10	50000±10000	1.549±0.11 E-11	0.327±0.066
#635 SS (63.04%)	2.8	1.05±0.05 E+11	120000±20000	3.785±0.18 E-12	0.466±0.078
#635 SS (63.04%)	3.5	1.11±0.05 E+11	120000±20000	3.596±0.16 E-12	0.454±0.076

As expected, the hydrodynamic parameters determined for oscillatory flow are generally anisotropic and different from those obtained under steady flow conditions. For both of the tested charge pressures, however, identical viscous and inertial resistances were determined to best fit the experimental data. The only observed exception was for the #635 stainless steel filler in radial flow, for which the obtained viscous resistances differed slightly with the fill pressure. However, the two values determined were within the confidence intervals of one another and thus the variation is not deemed to be significant. The results therefore suggest that the hydrodynamic parameters of these materials under oscillatory flow may be insensitive to the mean pressure. Such a result is not unexpected as the pressure insensitivity of steady flow hydrodynamic parameters for several regenerator fillers has been previously demonstrated [76]; however, more experimentation is needed to verify this conclusion.

CHAPTER 4

COMPUTATIONAL MODELING OF MINIATURE PTRS

This chapter describes the various numerical models which have been used in this investigation to simulate miniature pulse tube refrigerators. The results of the initial Sage scaling models are also presented.

4.1 General Approach

The modeling approach which has been followed in order to develop CFD models of miniaturized pulse tube cryocoolers is described here. An initial scaling analysis was performed using the Sage cryocooler modeling program, followed by the construction of full system and component level models using the Fluent CFD code. The system level CFD models were divided into two groups: meso-scale models having complete system volumes of less than 10 cc and micro-scale models having volumes of approximately 1 cc or less. The meso-scale CFD models shared geometry and operating conditions so that their results could be quantitatively compared to one another. Following this approach the effects of preferential flow paths in the regenerator and tapering of sharp edged component junctions were examined. A component level model of the pulse tube and its adjoining heat exchangers was also developed and used to investigate the effects of variation in the thermal and viscous boundary layer thicknesses relative to the pulse tube diameter. Finally, by applying the results of these investigations a series of micro-scale system level PTR models was constructed at successively higher operating frequencies

and smaller dimensions. These final models are intended to illustrate the possibility of PTR miniaturization well beyond what has presently been accomplished, providing that challenges pertaining to the regenerator filler and compressor can be overcome.

As discussed in Chapter 2, it is believed that CFD simulation will be the most accurate and directly relevant technique for modeling miniature PTRs. Because CFD codes such as Fluent numerically solve the governing conservation equations throughout a multidimensional model domain, they do not include some of the simplifying approximations and assumptions which are present in dedicated PTR models; therefore, there may be more confidence about their applicability to miniature systems. These governing equations, as formulated in Fluent, are described in Section 3.1. Due to their multidimensionality, CFD models are also able to predict complex flow details overlooked by one-dimensional models, likely improving their accuracy for miniature PTRs.

Some of the limitations of CFD modeling must be addressed, however, in order to successfully simulate miniature PTRs with this technique. In order to produce meaningful results, the models need accurate closure relations and boundary conditions, particularly with regard to the hydrodynamic and thermal transport processes occurring in the porous segments of the PTR. Fluent's porous media model, used for the regenerator and heat exchangers, requires values for viscous and inertial resistance coefficients characteristic of the particular porous media being modeled. To address this need, the experiments and simulations described in Chapter 3 have been performed in order to determine these parameters for stacked screens of 635 stainless steel and 325 phosphor-bronze wire meshes. These are among the finest commercially available wire meshes and are suitable

for use as regenerator and heat exchanger fillers, respectively, for miniature PTRs. The hydrodynamic parameters used to represent these materials in both the system level and component level CFD models are the oscillatory flow parameters presented in Table 3.3.

Another significant limitation of CFD modeling is the considerable amount of computational time required to obtain solutions to complex problems. In this investigation, this is compounded by the need for transient solutions to represent the periodic processes occurring in PTRs. Generally, such simulations need to be iterated for many cycles of the device operating frequency before reaching the necessary steady-periodic state. For this reason, performing extensive parametric studies and optimization with CFD models is often prohibitively time consuming. However, previous efforts at modeling miniature PTRs in Fluent by directly scaling down existing models of larger cryocoolers resulted in drastically reduced performance [65], and thus such studies were necessary at the outset of this investigation in order to produce viable miniature scale models. To address this need, Sage has been used for preliminary optimization of both the geometry and operating conditions for the meso-scale system level CFD models, as well as for determining suitable inertance tube lengths for the successive micro-scale models. This parallel use of Sage and Fluent takes advantage of the complementary strengths of the two techniques, i.e. the speed of Sage and the high level of detail provided by Fluent.

4.2 Sage Modeling and Initial Scaling Analysis

At the outset of this investigation, it was anticipated that the miniature PTR models to be developed would require geometry and operating conditions different from those of conventional scale devices. Therefore, in order to provide viable initial values of these parameters for the CFD models of miniature PTRs developed in this investigation, a preliminary scaling analysis was performed using Sage [56]. In this preliminary analysis, the abilities of Sage to quickly solve for the steady-periodic behavior of PTRs and perform multi-dimensional mappings and optimizations were exploited to produce not only approximate geometry and operating conditions for miniature PTRs but expected trends in their performance as several essential parameters were varied. The Sage models used for this task were based upon an existing, experimentally correlated model of a relatively small conventional scale PTR [63]; a diagram of one of these models is shown in Figure 4.1. Initially, this model was directly scaled down to produce meso-scale representations of both standard inertance tube PTRs and reservoir-less versions as introduced by Garaway [30] with total volumes of 2-4 cm^3. Mesh fillers for the regenerator and heat exchangers were changed from the coarser materials in the original model to #635 stainless steel and #325 phosphor bronze wire meshes, respectively. Parametric mappings and optimizations of select parameters were then performed with these models in order to determine geometry and operating conditions more suitable to miniature PTRs.

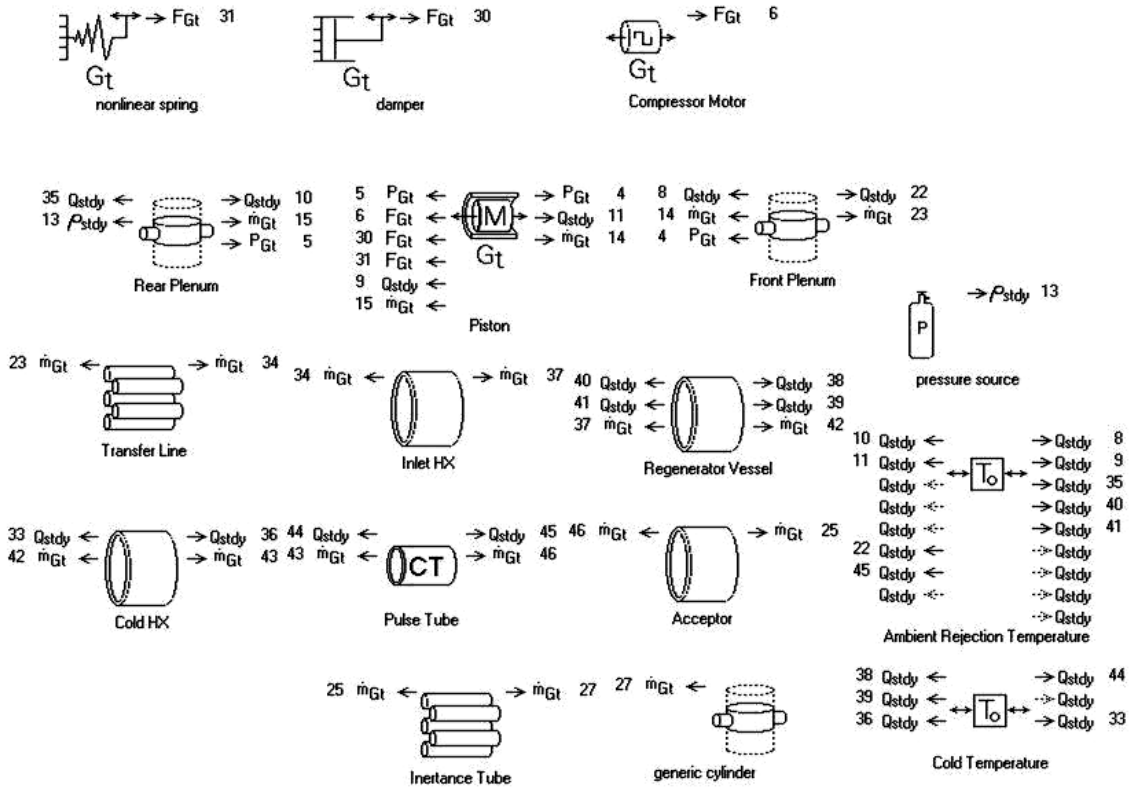

Figure 4.1 Sage diagram of simulated PTR

Despite the multi-parameter optimization capabilities of Sage, only a limited number of geometrical dimensions could be effectively optimized. Therefore, the length and/or diameter of most PTR components were fixed after the initial direct scaling and only the parameters expected to have the greatest effect on the system performance were optimized. These optimized parameters included the lengths of the pulse tube, regenerator, and inertance tube, the operating frequency and the charge pressure. The results of the optimizations and mappings of these parameters will be discussed in the following paragraphs. The resulting geometry and operating conditions, both directly scaled and optimized, are displayed in Table 4.1 and Table 4.2 preceding this discussion so that they may be referred to as needed.

Table 4.1 Geometry for initial Sage miniature PTR models

Model	Regenerator		Pulse Tube		Inertance Tube		Reservoir
	Length (mm)	Dia (mm)	Length (mm)	Dia (mm)	Length (mm)	Dia (mm)	Volume (cc)
Standard ITPTR	20	4	40	2.5	0.8097	0.6	2
Reservoir-less ITPTR	20	4	40	2.5	1.656	0.6	----

Model	Warm Heat Exchanger 1		Cold Heat Exchanger		Warm Heat Exchanger 2		Total
	Length (mm)	Dia (mm)	Length (mm)	Dia (mm)	Length (mm)	Dia (mm)	Volume (cc)
Standard ITPTR	10	4	4	4	5	4	4.06
Reservoir-less ITPTR	10	4	4	4	5	4	2.29

Table 4.2 Operating conditions for initial Sage miniature PTR models

Frequency (Hz)	Operating Pressure (Mpa)	Cold End Temperature (K)
200	3.55	120

For these initial Sage models, the compressor volume and stroke were initially scaled to produce a pressure ratio of 1.15. This pressure ratio was selected in order to preserve the possibility of building an experimental system using facilities mostly available at the time. Similar criteria were applied to the frequency and operating pressure. Because increases in either of these parameters resulted in increased input power to the model, it was difficult to determine optimized values for them with Sage as originally planned. Therefore, the frequency and operating pressure were selected for the initial models based upon the maximum value of each considered achievable experimentally at the time and the remaining model geometry was then optimized around the chosen values.

As discussed in Chapter 2, correct phasing between the oscillatory pressure and mass flow rates is critical to pulse tube refrigerator performance and therefore conclusions regarding model performance could not be drawn without first setting the proper phase relationships; therefore, the first geometric parameter optimized in Sage

after the initial scaling was the inertance tube length. Simulated curves of predicted cold end heat lift versus inertance tube length for both standard and reservoir-less ITPTR models are shown in Figure 4.2. As seen in this figure, several different lengths can provide near-optimal phase shift and thus maximize performance. The absolute maximum system performance occurs with the shortest of these, however, and so it was important to start the Sage optimizer near this point in order to avoid the other local maxima at longer lengths.

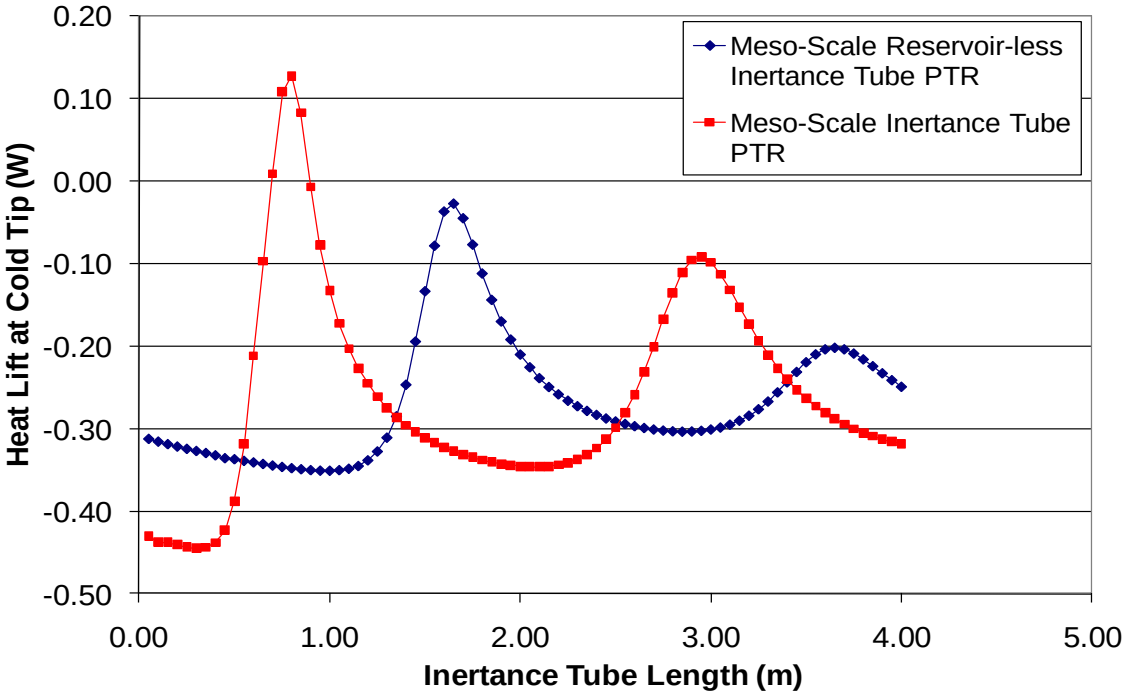

Figure 4.2 Sage predicted performance vs. inertance tube length

In order to determine optimal lengths for the regenerator and pulse tube, the variation in the Sage models' predicted performance was determined as these parameters were independently mapped over a range of values. Generally, simply optimizing these lengths with the built in Sage optimizer resulted in Sage increasing them up to the

maximum length allowed by the user specified constraints. Therefore, chosen values of these lengths were determined from the mappings displayed in Figure 4.3 and Figure 4.4 in order to strike a balance between performance, evaluated here by heat lift from the cold end, and compactness of the miniature PTR. Because the phasing of the oscillatory pressure and mass flow rate is dependent on the lengths of the regenerator and pulse tube, for each mapped length in Figure 4.3 and Figure 4.4 the inertance tube length was re-optimized to maintain the proper phase relationship. In both figures, all other geometry and operating conditions were those given in Table 4.1 and Table 4.2. For the regenerator length, shown in Figure 4.3, the predicted performance falls off sharply below 20 mm but increases only slightly as the length is increased to 30 mm. As shown in the figure, 20 mm was therefore selected as the regenerator length. The predicted performance increased more steadily with the pulse tube length, shown in **Figure 4.4**; in this case, 40 mm was selected in order to best balance the predicted heat lift and device compactness.

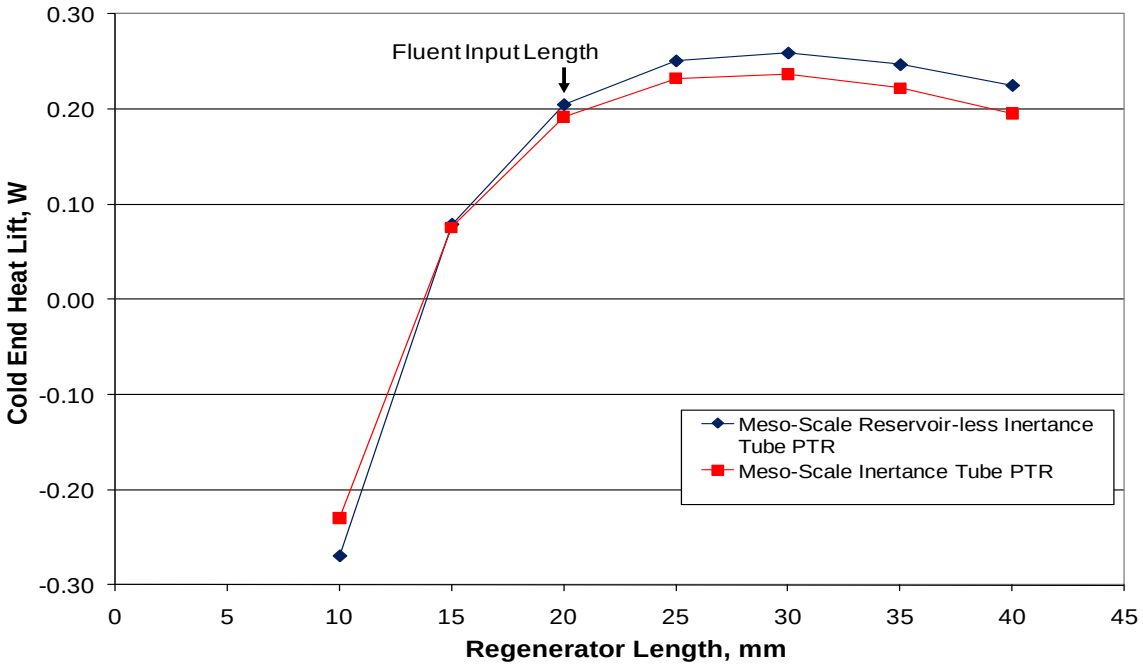

Figure 4.3 Sage predicted performance vs. regenerator length

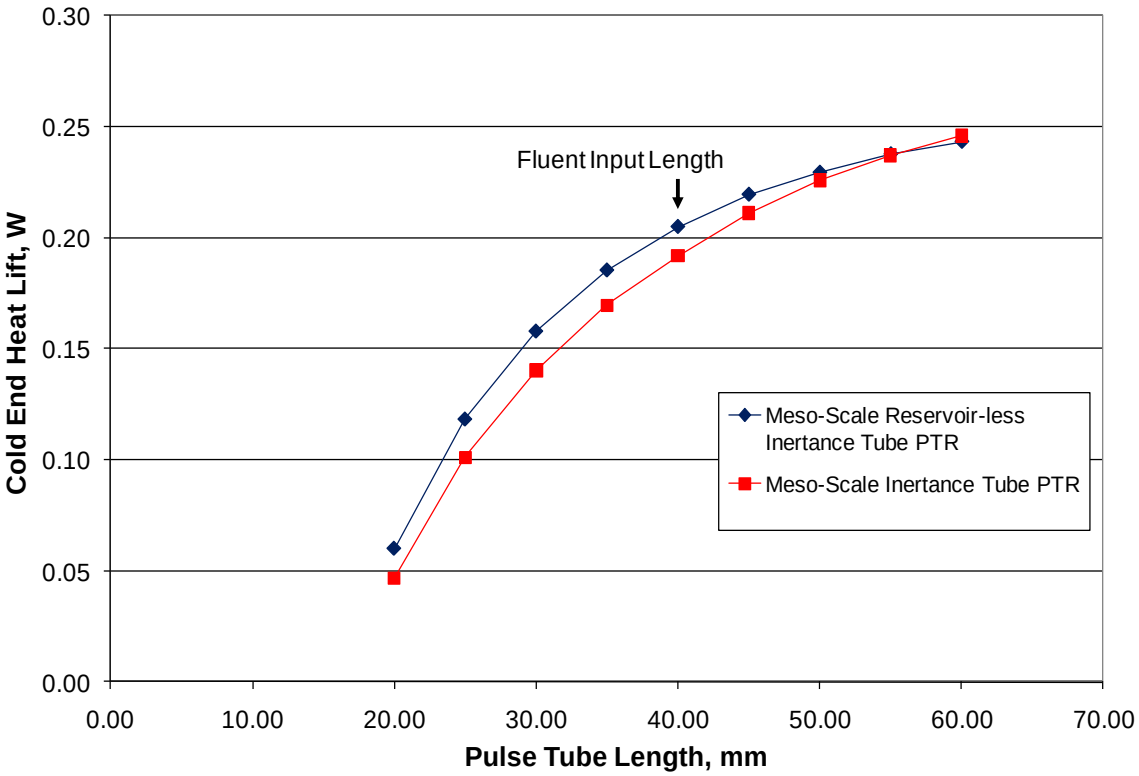

Figure 4.4 Sage predicted performance vs. pulse tube length

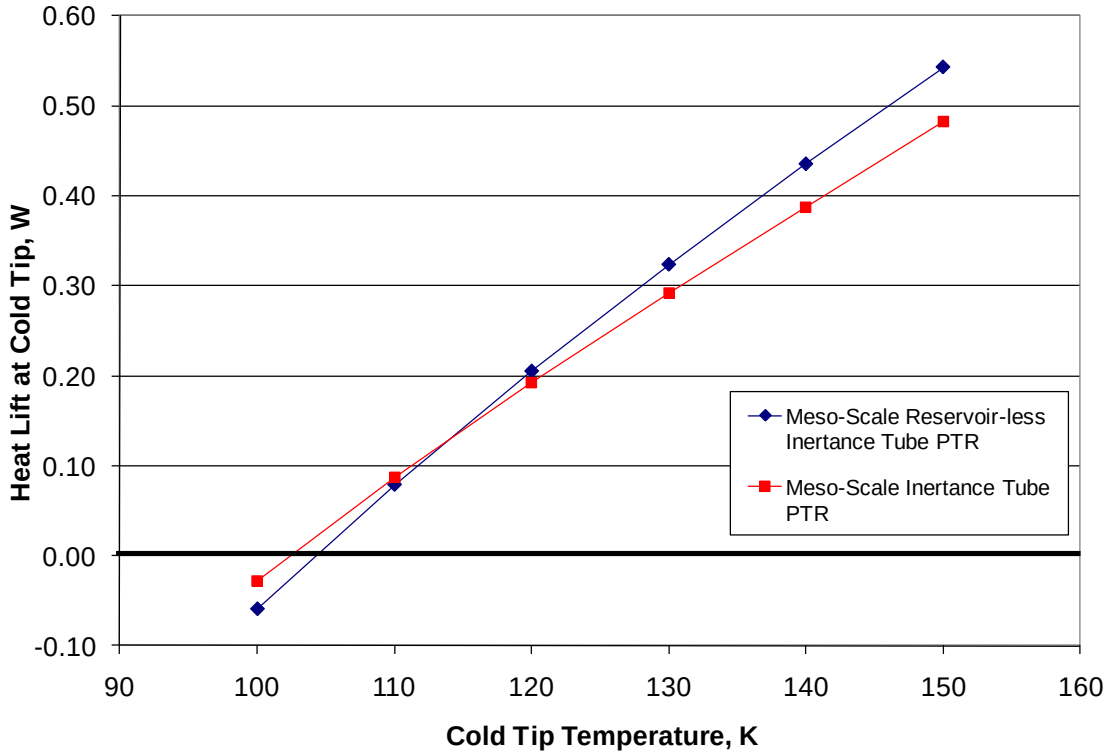

Figure 4.5 Sage predicted load curves

The initial scaling analysis was concluded with the generation of simulated load curves of heat lift from the cold tip versus cold tip temperature, shown in Figure 4.5.These curves were produced by models using the geometry given in Table 4.1 and operating conditions, exccluding the cold end temperature, given in Table 4.2. Ultimate (no-load) cold tip temperatures of approximately 105 K were predicted for both models. With these results, the geometry and operating conditions determined through the initial scaling analysis were deemed suitable to begin the CFD modeling effort. Through an iterative refinement process involving both Fluent and Sage modeling, the final meso-scale CFD models ended up using slightly different parameters than those given here. These models and the modifications made will be described in the following section.

4.3 System Level CFD Modeling

In this section, the full PTR system CFD models used in this investigation are described. A brief discussion is given of the initial CFD models which followed the Sage scaling analysis described in the previous section, followed by much more detailed descriptions of the subsequently improved system level models which were used to generate the majority of the results presented in the following chapter.

Following the preliminary scaling analysis in Sage, an initial set of system level CFD models was constructed using the geometry and operating conditions listed in Table 4.1 and Table 4.2. These models incorporated oscillatory pressure inlets and adiabatic walls on their cold heat exchangers in order to simulate a no-load condition; subsequently, both of these boundary conditions were determined to cause periodic

steady state convergence problems. For this reason, the performance predicted by these models was poor relative to that predicted by Sage. The results of these preliminary CFD models will not be repeated here but are available in [56]. Later system level CFD models were revised to eliminate the oscillatory pressure inlet condition in favor of a moving piston pressure oscillator and to incorporate constant temperature boundary conditions for their cold heat exchanger walls. These changes resulted in significantly faster and better convergence of the models to periodic steady state.

After the preliminary CFD modeling effort, improvements were made to the utilized modeling techniques and system level CFD models of meso-scale and micro-scale PTRs were constructed in Fluent. The meso-scale models shared common geometry and operating conditions while those at the micro-scale operated at successively higher pressures and frequencies using successively smaller component dimensions. In the following paragraphs modeling techniques common to both sets of models will be described. Their geometry and operating conditions, however, will be given with their results in Chapter 5.

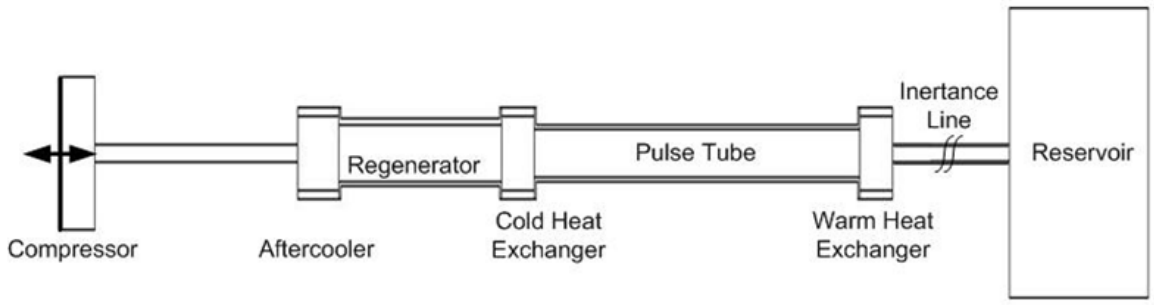

Figure 4.6 Schematic of system level PTR CFD models

The system level CFD models were all two dimensional axisymmetric representations of complete miniature PTRs as depicted in the common schematic of Figure 4.6. Only inertance tube PTRs with reservoirs were modeled; the reservoir-less versions considered in the preliminary Sage analysis were not investigated further. The compressor was modeled with a moving wall, shown with a double ended arrow in Figure 4.6, to which a user-defined sinusoidal displacement was applied. The user defined function defining this wall motion is reproduced in Appendix B. The Fluent dynamic meshing model was used to add and subtract mesh layers as the wall moved. Importantly, this method of simulating the compressor results in a closed system representation of the miniature PTRs, which was found to be necessary to prevent changes in the calculated total mass of the models during the extended transient simulations.

The Fluent models had helium specified as their working fluid, which was treated as an ideal gas. Solid and mesh filler materials were selected for the models based upon their suitability for the fabrication of miniature PTRs. As previously mentioned, #635 stainless steel mesh was chosen for the regenerator; likewise, the aftercooler, warm and cold heat exchangers were all modeled as #325 phosphor-bronze mesh. These mesh fillers have been selected for their small pore sizes and ability to be cut into discs small enough for miniaturized PTRs. To model these materials, the FLUENT porous media model requires viscous and inertial resistance coefficients related to the Darcy permeability and Forchheimer's inertial coefficient. As described in Chapter 3, these parameters have been determined from experiments as part of this investigation.

The aftercooler, cold and warm heat exchanger walls were all modeled as sterling silver while the regenerator and pulse tube walls were modeled as stainless steel. Construction of miniature PTR models using PEEK for the regenerator and pulse tube walls was considered, but preliminary results showed insufficient increase in performance to justify the accompanying difficulties in construction if a prototype device were to eventually be built. Wall conduction in these components was incorporated into the CFD models by discretizing the solid regions and applying the appropriate material properties. The reservoir, inertance line, and the transfer line between the compressor and aftercooler were all modeled with isothermal walls at 293 K. Modeling solid walls with finite thicknesses for these components was not necessary because the isothermal boundary condition eliminated axial temperature gradients, rendering axial heat conduction negligible in these elements.

The outer surfaces of the aftercooler and warm heat exchanger walls were modeled isothermally at 293 K. The outside of the cold heat exchanger wall was modeled isothermally as well, but at the specified cold tip temperature which was generally varied. The benefit of modeling the cold heat exchanger as isothermal rather than adiabatic is that defining a cold end temperature eliminates large transients and drifting in the model temperature profile and thus greatly speeds up convergence to periodic steady state. Adiabatic boundary conditions were reasonable for the outer surfaces of the regenerator and pulse tube walls, however, and were incorporated there.

For all of the system-level CFD models, ‘PRESTO!’ pressure discretization was used along with ‘PISO’ pressure-velocity coupling and second order upwind discretization of all other quantities; these settings have been chosen to provide the best

and fastest convergence of the models. Spatial discretization was accomplished with meshes fine enough that acceptable grid independence of the results could be verified; this is discussed further with the results for each set of models in Chapter 5. Double precision, pressure-based steady and unsteady solvers were used with the physical velocity porous media flow formulation selected. Preliminary simulation results suggested that oscillatory turbulent flow might occur in the transfer and inertance lines; therefore, the standard k-omega turbulence model with low Reynolds number corrections for near-wall processes was utilized. This turbulence model was chosen for its ability to handle transitionally turbulent flow and because it improved the overall periodic steady state convergence of the models. Residual convergence criteria for the 2D models were set at 10^{-9} for the energy equation and 10^{-8} for continuity, velocity, k, and omega.

To reduce computational time, the Fluent models were started with assumed linear temperature distributions. To accomplish this, the models were first initialized at a constant temperature of 293 K. The warm and cold heat exchanger exterior walls were then prescribed their normal isothermal boundary conditions and the models were iterated using the steady state solver in order to set up linear temperature gradients in the pulse tube and regenerator. A contour plot of temperature for a meso-scale model initialized in this manner to a cold tip temperature of 150 K is shown in Figure 4.7; for scaling purposes, the inertance volume and reservoir are omitted. Following this initialization, the unsteady solver was selected to begin the transient simulations. These were performed using time steps which were based upon the operating frequency of the model, determined so that there would be 250 time steps per period of the compressor driving frequency.

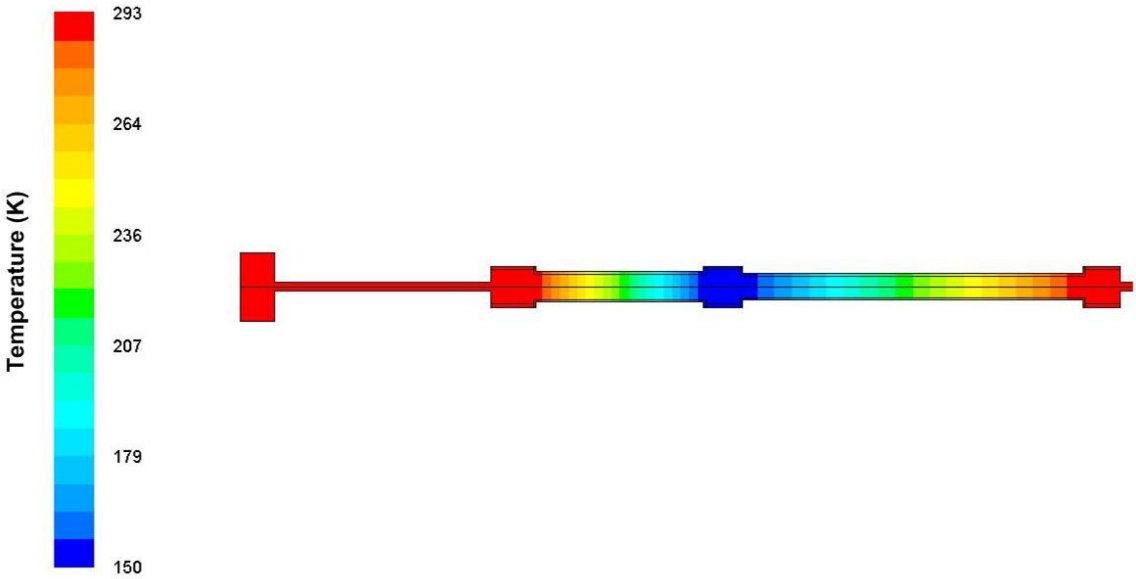

Figure 4.7 Temperature contours for initialized meso-scale model

The models were iterated until approximate periodic steady state conditions were attained, at which point the model results were essentially repeated for subsequent periods of the compressor oscillation. To judge this convergence, selected output values from the models were monitored and cycle-averaged. These included pressures, velocities, mass flow rates, and enthalpy flow rates at the inlet of each component, wall heat fluxes, and the total system mass and energy. The cycle-averaging was performed using a moving window with a width of 250 time steps, equal to one period of the compressor's oscillation. Two Matlab programs were written in order to post-process the system level CFD models. The first of these performs enthalpy balances on the overall system and all of its individual components, while the second calculates phase angles between the oscillatory velocity and pressure at the inlet to each component. These programs are reproduced in Appendix C.

An example of model results approaching periodic steady state is shown in Figure 4.8, which is a time history of the various cycle-averaged energy fluxes into and out of a

typical Fluent system level miniature PTR model. The lines in this figure represent the cycle-averaged rates of heat or energy transfer into and out of the model. The inlet power is calculated from the flow rate of Fluent's 'total enthalpy' field variable at the junction of the compressor and transfer line. Similarly, the net heat fluxes for the aftercooler and heat exchangers are integrals of 'total surface heat flux' on the outer walls of these components. For simplicity in reporting results, the aftercooler heat flux includes the heat transferred through the isothermal transfer line wall and the warm heat exchanger heat flux includes contributions from the inertance line and reservoir walls. The figure shows that the model converges rather quickly towards periodic steady state.

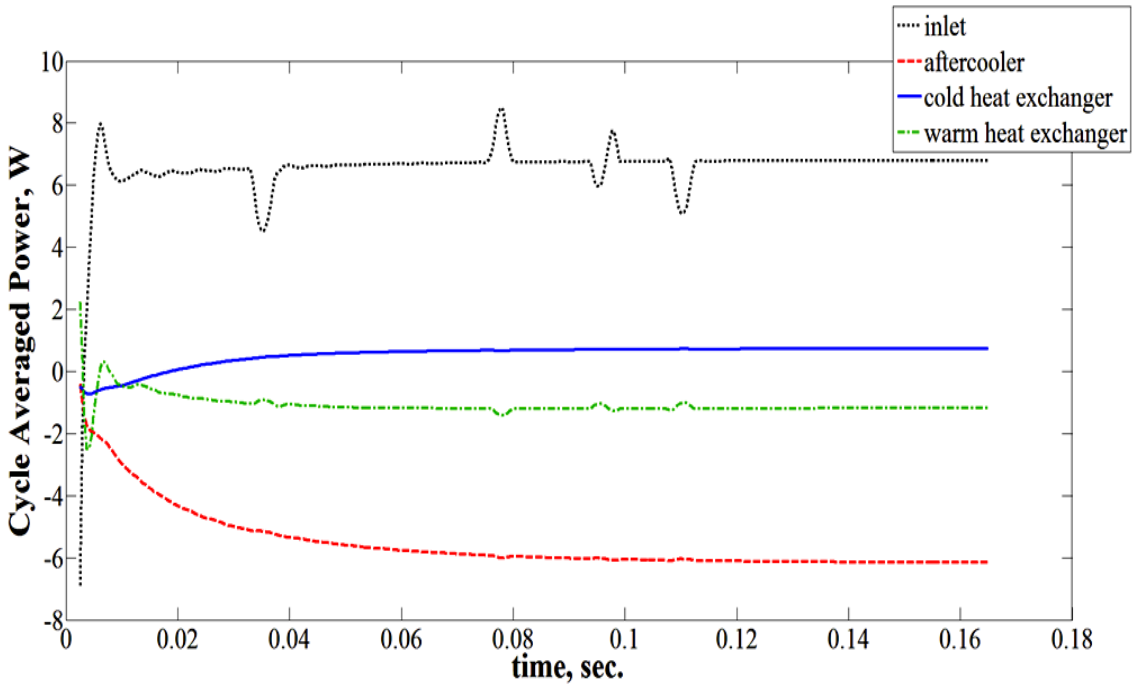

Figure 4.8 Sample cycle averaged model energy flux history, meso-scale base model with 180 K cold tip temperature

4.4 Component Level Models

CFD modeling of PTR sub-sections greatly reduces the necessary computational time compared to system level models of the same size and mesh spacing. This technique may therefore be useful for performing parametric studies requiring a large number of CFD models or for examining a PTR component with finer spatial or temporal spacing than is practical with a larger system level model. In this investigation, such component level models have been constructed in order to characterize the effects of the thermal and viscous boundary layers in the pulse tube. This was accomplished by performing a parametric study in which the ratio of the two boundary layer thicknesses to the pulse tube diameter was varied. Detailed representations of the characteristics of these boundary layers required multidimensional models with very fine grid spacing; furthermore, a large number of models was necessary in order to cover a wide range of boundary layer thickness to diameter ratios in the parametric study. The multidimensionality of the examined phenomena precluded the use of Sage and performing such a study with full system CFD models would have prohibitively time consuming; therefore, component level CFD modeling was an ideal approach to this problem.

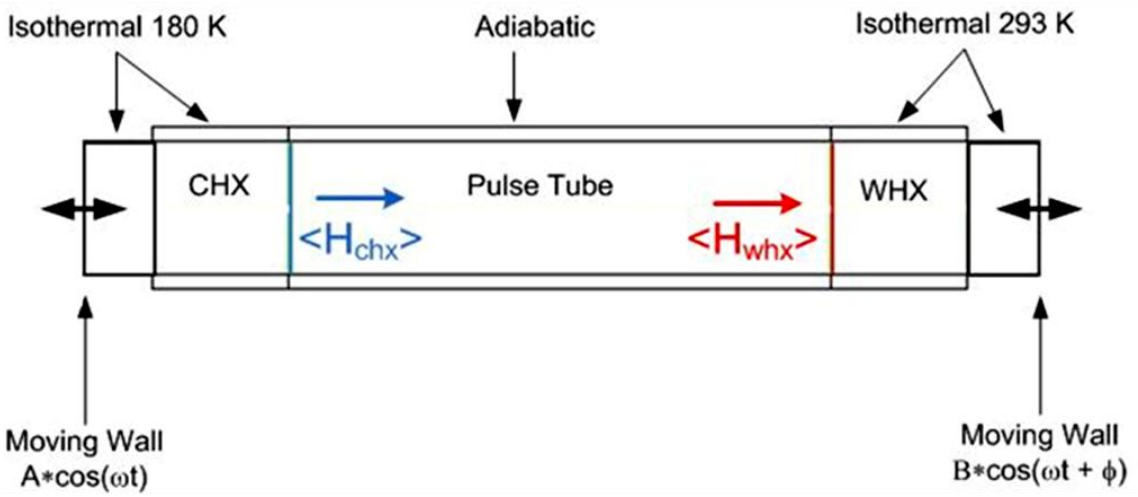

Figure 4.9 Schematic of pulse tube component level CFD model

A schematic of these component level CFD pulse tube models is shown in Figure 4.9. For computational efficiency, only the cold heat exchanger, pulse tube, and warm heat exchanger were included in the models, which were 2D axisymmetric in order to take advantage of the symmetry of the problem. Additional open fluid domains with initial lengths of 2 mm were added outside the two heat exchangers for the implementation of flow boundary conditions. The side walls of these domains were prescribed sinusoidal motions, shown in Figure 4.9, whose amplitudes A and B and phase angle ϕ were adjusted to produce the desired oscillatory flow conditions in the pulse tube. The Fluent user defined function through which these boundary conditions were implemented is reproduced in Appendix B. These parameters were selected to provide a pressure ratio of 1.10, pulse tube gas column of 92%, and phase angles of 8° and 46° at the cold end and warm end of the pulse tube, respectively. The pulse tube gas column is the percentage of the gas contained in the pulse tube which does not leave it over the course of the oscillatory flow cycle. It is indicative of the combined oscillatory mass flow rates at both ends of the pulse tube, but unlike the mass flow rates may be held constant

as the model scale changes. These boundary conditions were derived from the results of the full system CFD models described in the previous section.

The pulse tube walls were modeled as steel and the heat exchanger walls were modeled as copper using constant material properties. These solid regions were discretized and included in order to incorporate wall conduction into the models. Isothermal boundary conditions were applied to the outer surfaces of these walls with temperatures of 293 K and 180 K for the warm and cold heat exchangers, respectively, and the pulse tube outer wall was modeled as adiabatic. Helium was specified as the model working fluid with temperature dependent properties, expected to enhance streaming phenomena in the pulse tube, specified for its thermal conductivity, viscosity, and specific heat using tabular values at the operating pressure of 4 MPa [79]. Fluent's porous media model was used for the warm and cold heat exchangers, with viscous and inertial resistance coefficients specified for #325 phosphor-bronze mesh at 67% porosity, as given in Table 3.3.

Moving mesh models, discretization techniques, and other model parameters were identical to those previously described for the system level models, with the exception that a laminar flow model was used instead of the k-omega turbulence model. Residual convergence criteria were set at 10^{-8} for the energy equation, continuity, and axial and radial velocities. In the same manner as the full system models, these component level models were initialized with a linear temperature gradient and then iterated with the transient solver until they approached periodic steady state. The time step size was selected to provide 250 time steps per period of oscillations for each frequency and the models were iterated for 2500 time steps (10 periods) before results were evaluated.

Monitors of pressure, velocity, mass flow rates, enthalpy flow rates and surface heat fluxes on relevant control surfaces were incorporated and an additional Matlab program, reproduced in Appendix D, was written for post processing these component level pulse tube models.

CHAPTER 5

RESULTS AND DISCUSSION

In this chapter, the results of the previously described CFD models are given. System level models at the meso-scale are discussed first, followed by component level models of the pulse tube. Finally, the results of these are applied to produce successively smaller micro scale PTR models for which cooling is predicted at cryogenic temperatures.

5.1 Meso-Scale System Level Models

The results of the meso-scale system level CFD models of inertance tube PTRs are described in this section. The meso-scale refers here to miniature PTRs having a total system volume of less than 10 cc. These models shared geometry and operating conditions so that their results could be quantitatively compared to one another. These parameters are presented in the first subsection along with the results of the unmodified or base models. Later subsections present the results of models incorporating preferential flow paths in the regenerator and tapering of sharp edged component junctions.

5.1.1Base Models

The geometry and operating conditions for the system level meso scale models were similar to those presented as the result of the Sage scaling analysis in the previous chapter. The revisions consisted of an increase in operating pressure to 4 MPa, an

increase in the pressure ratio from 1.15 to approximately 1.25, and several adjustments to the model geometry. Specifically, these were a reduction in the regenerator diameter from 4 mm to 3 mm, reductions in the lengths of the warm heat exchangers, an increase in the volume of the reservoir, and a re-optimization of the inertance tube length and slight increase in its diameter. The resulting geometry and operating conditions, shared by all of the meso-scale CFD models, are presented in Table 5.1. For all of these simulations, time steps of 20 μs were used, corresponding to 250 time steps per period of the 200 Hz operating frequency The schematic of these models is displayed in the previous chapter as Figure 4.6.

Table 5.1 Meso-scale CFD model geometry and operating conditions

Regenerator		Pulse Tube		Inertance Tube		Frequency	Operating
length (mm)	dia (mm)	length (mm)	dia (mm)	length (m)	dia (mm)	(Hz)	Pressure (MPa)
20	3	40	2.5	0.8208	1	200	4

Aftercooler		Cold Heat Exchanger		Warm Heat Exchanger		Reservoir	Approximate Total
length (mm)	dia (mm)	length (mm)	dia (mm)	length (mm)	dia (mm)	Volume (cm^3)	Volume (cm^3)
5	4	4	4	4	4	5	6.3

Following the methodology described in Chapter 4, miniature PTR models incorporating these parameters were constructed in both Sage and Fluent. Using these models, a direct comparison of the results of Sage and Fluent could be made and the effects of subsequent modifications to the Fluent models could be quantified. Load curves of heat lift from the cold end vs. cold tip temperature predicted by both Fluent and Sage for these meso-scale models are shown in Figure 5.1. Although the pressure ratios calculated by Sage and Fluent were approximately equal, Sage predicted a lower average input power of approximately 5.4 W compared to the 6.8 W predicted by Fluent. For this reason, the differences in the simulated performance results of the two programs become

more apparent when the coefficient of performance is calculated. The COP for a refrigeration cycle is defined below and plotted in Figure 5.2 as a percentage of the Carnot COP. From Figure 5.1 and Figure 5.2 it is apparent that Sage predicts generally higher performance as well as a lower ultimate cold tip temperature for the simulated meso-scale PTR. Unfortunately, due to the lack of experimental data for the simulated PTR conclusions regarding the accuracy of the two models cannot be drawn.

$$\mathrm{COP_R} = \frac{Q_C}{W_{in}} \tag{5.1}$$

$$\mathrm{COP_{Carnot}} = \frac{\mathrm{T_C}}{(\mathrm{T_W} - \mathrm{T_C})} \tag{5.2}$$

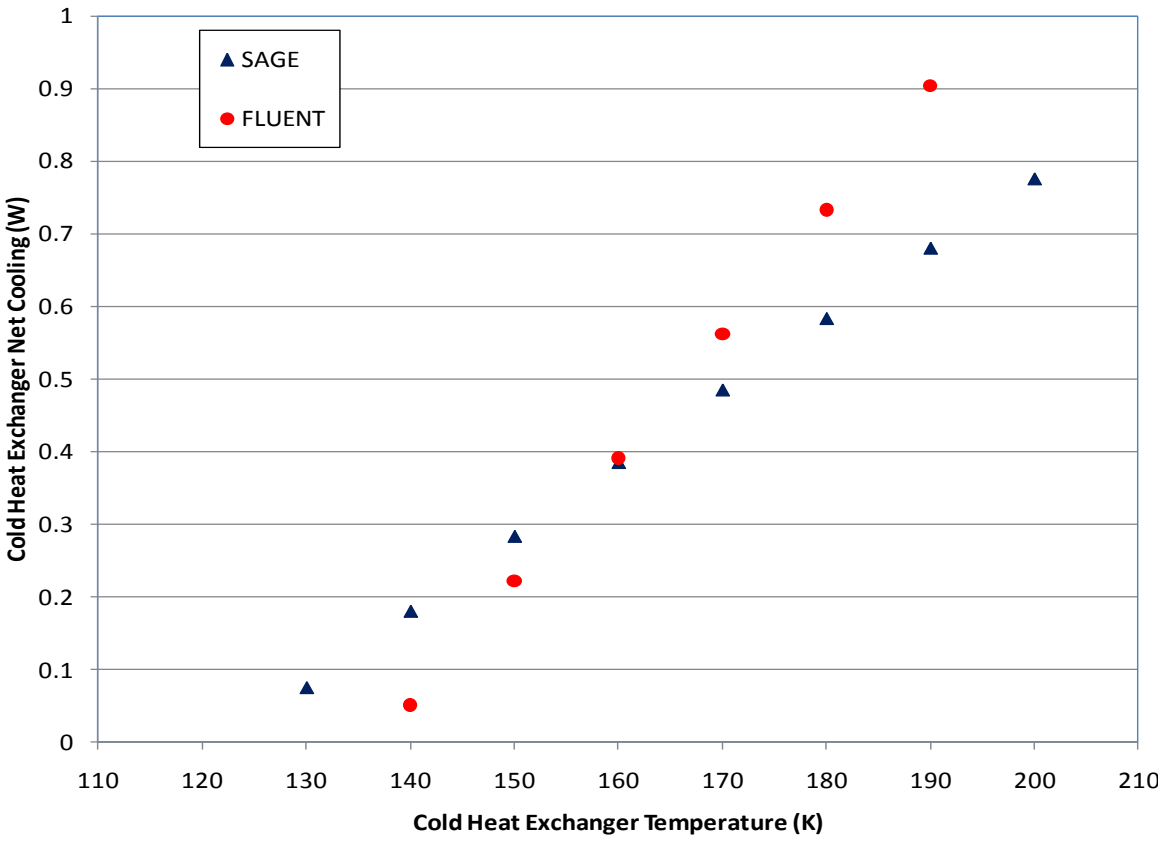

Figure 5.1 Simulated load curves for meso-scale PTR Models in Fluent and Sage

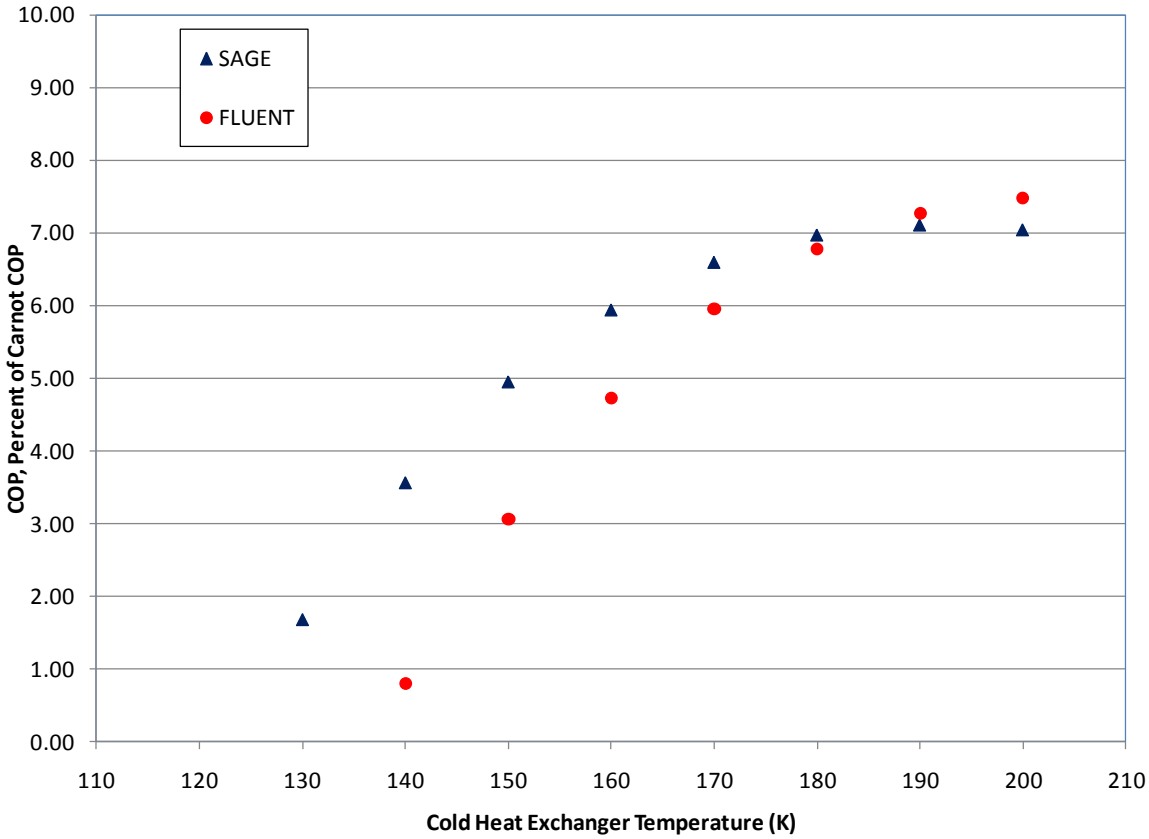

Figure 5.2 COP as a percentage of the Carnot COP for Sage and Fluent models

As discussed in Chapter 2, the phase angle between the pressure and the velocity or mass flow rate is critical to efficient PTR operation. The maximum enthalpy flux in the pulse tube occurs when these quantities are in phase at its cold end. Pressure losses in the regenerator, however, are usually minimized when the phase angle is zero near the regenerator center instead. Therefore, the optimum case which maximizes the PTR's efficiency generally lies between these two conditions. Because of the importance of this phase relationship, the phase angle between the simulated pressure and velocity waveforms was calculated at the inlet (compressor side) of each of the PTR components identified in Figure 4.6, with the exception of the compressor. These are presented for the base model with 150 K cold tip temperature in Table 5.2. Phase angles calculated using a corresponding Sage model are tabulated there as well.

Table 5.2 Simulated phase angles at various component inlets, base model 150 K.

	Simulated Phase Angles (Degrees)			
Model	Aftercooler	Regenerator	Cold Heat Exchanger	Pulse Tube
Fluent	-23	-17	-2	7
Sage	-23.6	-11.3	15.7	26.6

Model	Warm Heat Exchanger	Inertance Line	Reservoir
Fluent	38	47	-84
Sage	56.1	61.1	-86.8

The phase angles shown in Table 5.2 are reasonable for an optimized inertance tube PTR, although it is likely that there is potential for further optimization for the Fluent CFD models. The phase angles depend significantly on the inertance tube length, which was determined using Sage and simply input into the Fluent models. Therefore, the discrepancy between the phase angles predicted by the two programs suggests that the inertance tube length prescribed by Sage may not result in optimal performance for the Fluent models. However, due to the difficulty in performing significant geometry optimization using CFD, the inertance length optimized in Sage was used for all of the meso-scale system level Fluent models. The additions of the regenerator annular gaps and component junction tapers presented in the following sections were found to have no significant effect on the calculated phase angles, with variations of no more than one degree observed. Therefore, the phase angles given in Table 5.2 are characteristic of all the meso-scale models and the effects of the gaps and tapers presented in the following sections on the simulated PTR performance were not due to changes in phase relationships.

5.1.2 Regenerator Defect Models

One of the concerns for PTR miniaturization identified in Chapter 2 was the likelihood that the gaps occurring between their regenerator fillers and housings would have a more significant effect on the miniature coolers than they do on conventional scale devices. Due partially to limitations on the wire and pore diameters of available wire mesh screens, miniature cryocoolers that use these materials as regenerator fillers generally have a much larger ratio of regenerator filler pore size to regenerator diameter than their conventionally sized counterparts. The porous morphology of the screens prevents them from being cut to perfectly match the diameter of the regenerator housing; instead, the edge of a cut screen will consist of partial mesh cells which have a characteristic size less than or equal to the pore diameter. As a result of both this irregular edge and manufacturing considerations, some open space is expected to exist between the edges of the screens and the housing with a dimension that is likely on the order of the mesh screen pore diameter. These gaps provide a low resistance flow path which may decrease the effectiveness of the regenerator.

In order to determine the effects of these gaps or defects on the performance of the miniature PTRs, models were constructed which included a small open annular region between the mesh regenerator filler and the inner wall of the regenerator housing. Accurately representing such multidimensional geometric features requires multidimensional modeling techniques; thus the effects of the annular gaps were simulated using meso-scale system level Fluent models. A basic schematic of these models is shown in Figure 5.3, including detail views of the annular regenerator gap of

width δ. Aside from the inclusion of the gap, these used the same geometry and operating conditions presented in Table 5.1.

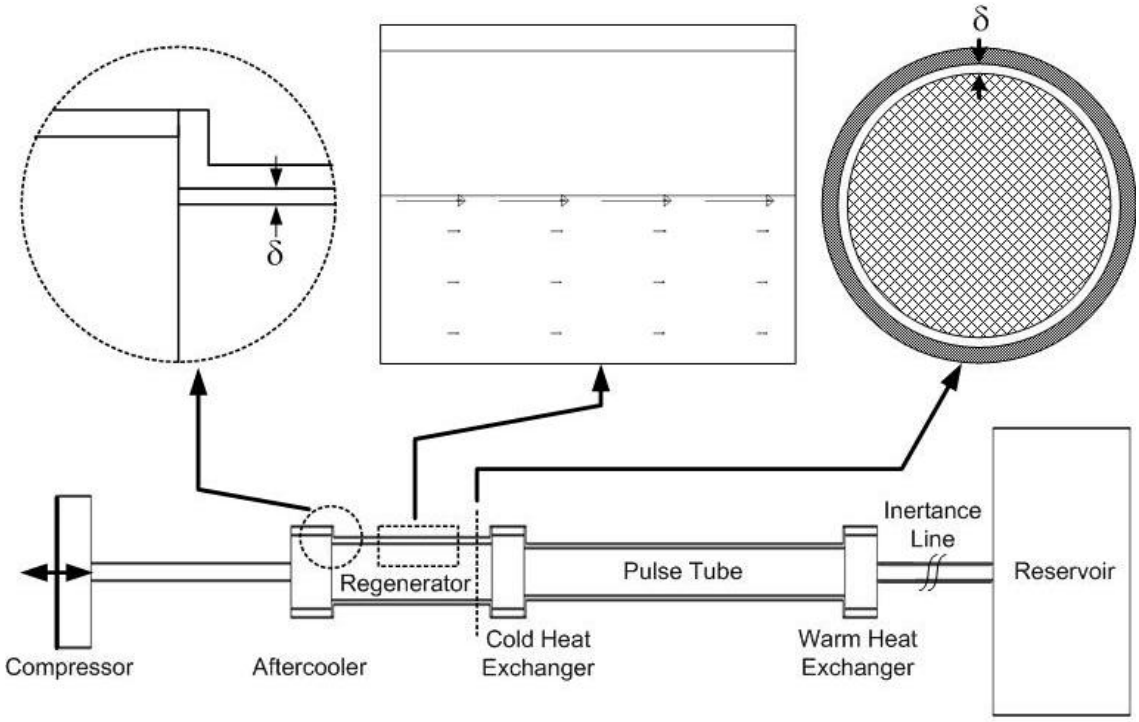

Figure 5.3 Schematic of PTR model with detail views of regenerator defects

Simulations were performed with defects of 10-30 μm, represented as an open fluid domain separate from the porous zone corresponding to the regenerator. The base model then represented a perfectly packed regenerator with a 0 μm gap. These defect widths, nondimensionalized by the regenerator shell inner radius R, corresponded to a range of δ/R from 0 to 0.02. The regenerator filler was modeled as #635 stainless steel mesh, which has a pore size of 20 μm; therefore, the 10 and 20 μm defects also corresponded to gaps of 0.5 and 1 mesh cell, respectively.

Simulated load curves of net heat lift vs. cold tip temperature for models having 10, 15, and 20 μm regenerator defects were constructed and are shown along with the

base model load curve in Figure 5.4. These load curves show that the 10 μm regenerator defect had very little effect on the predicted net cooling. The 15 and 20 μm gaps, however, were increasingly detrimental to the predicted performance and the 20 μm gap increased the predicted no-load temperature by approximately 20 K. Similarly, the 10 μm defect had little effect on the simulated coefficients of performance, plotted as a percentage of the Carnot COP in Figure 5.5, while the 15 μm defect decreased the COP slightly and the 20 μm defect decreased it much more significantly.

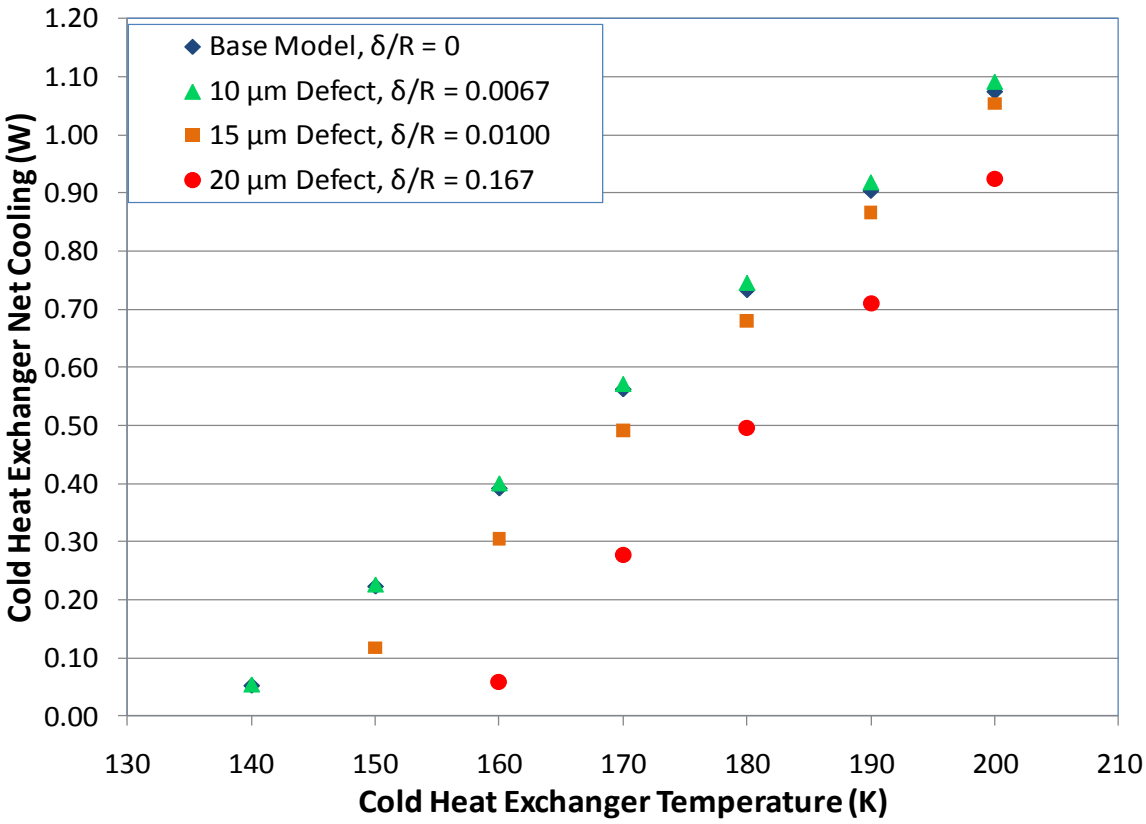

Figure 5.4 Simulated load curves for selected regenerator defect models

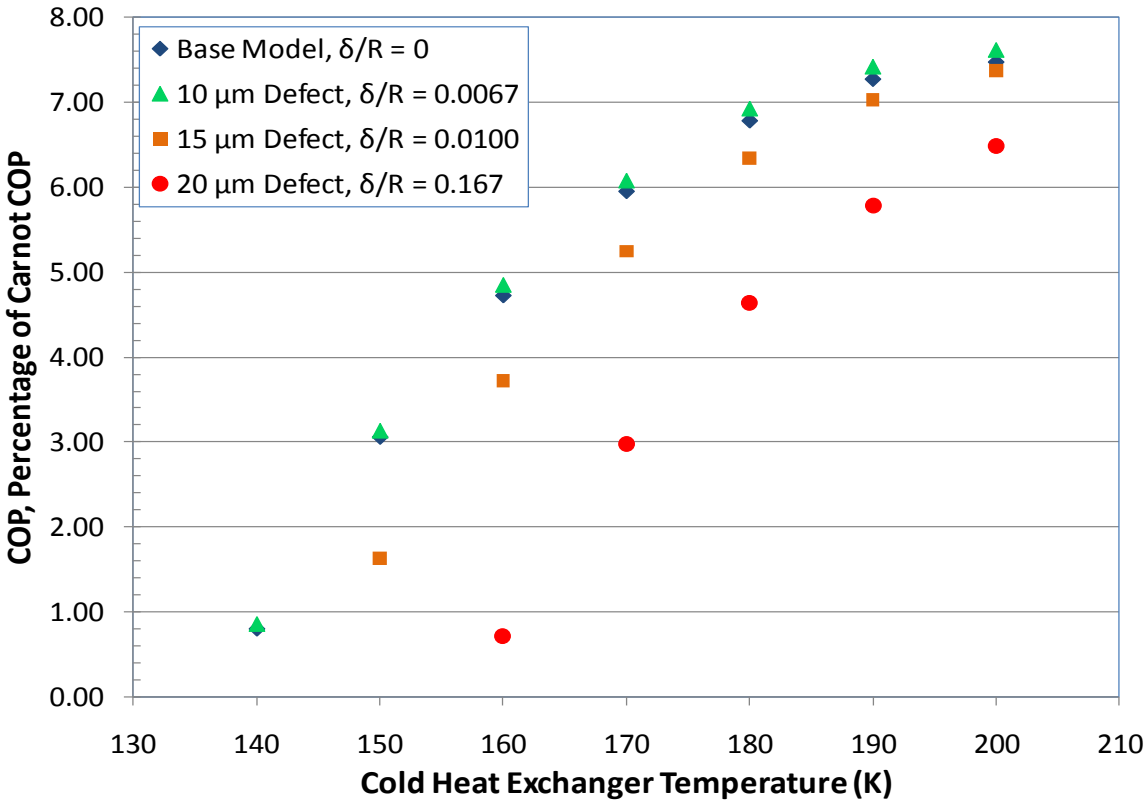

Figure 5.5 COP as a percentage of the Carnot COP for selected regenerator defect models

Additional regenerator defect models with gap widths from 10 to 30 µm in 2.5 µm increments were constructed with a 180 K cold tip temperature. The normalized loss in cooling resulting from these defects, obtained by subtracting the net cooling predicted for each model from that predicted for the base model at the same temperature and then normalizing by the cooling predicted for the base model, is plotted in Figure 5.6 along with the COP as a percentage of the Carnot COP for these models. These simulations indicate that the miniature PTRs may be relatively insensitive to gap widths of up to approximately 15 µm, or δ/R of 0.01. As the regenerator defect width increases beyond this point, the losses attributable to the defect rapidly become more significant. For the 30 µm defect (δ/R = 0.02) this loss becomes greater than the predicted net cooling for the

ideal case and thus the model predicts negative net cooling and a negative COP, synonymous with a predicted inability to maintain the indicated cold tip temperature.

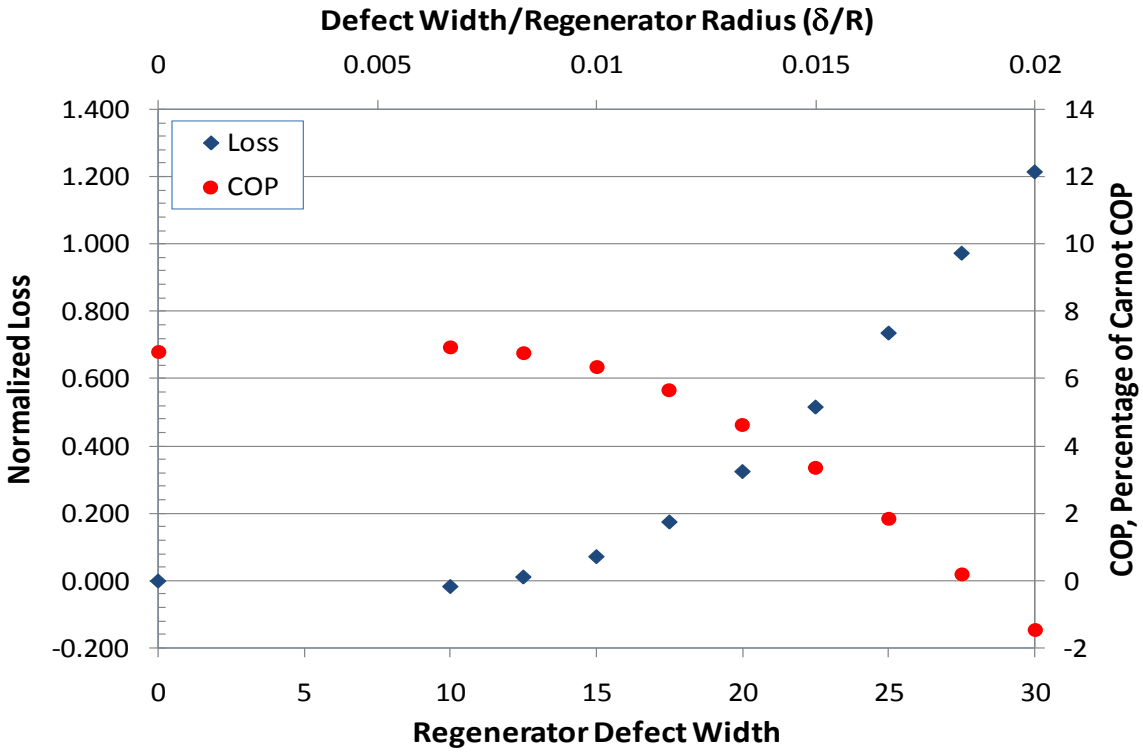

Figure 5.6 Normalized losses and COPs vs. regenerator defect width, 180 K cold tip temperature

The curves in the previous three figures demonstrate the effects of the regenerator gaps on cycle-averaged quantities which describe the overall PTC model performance. They offer very little insight, however, into how the presence of the defects alters the physical processes occurring in the regenerator. One of the greatest advantages of CFD modeling, in comparison to other techniques, is the level of detail available in the model results. In the following figures, visualizations of the predicted instantaneous temperature and velocity fields illustrate the effects of the regenerator gaps on the thermal and hydrodynamic processes in the regenerator, providing some explanation for the effects seen on the predicted overall performance.

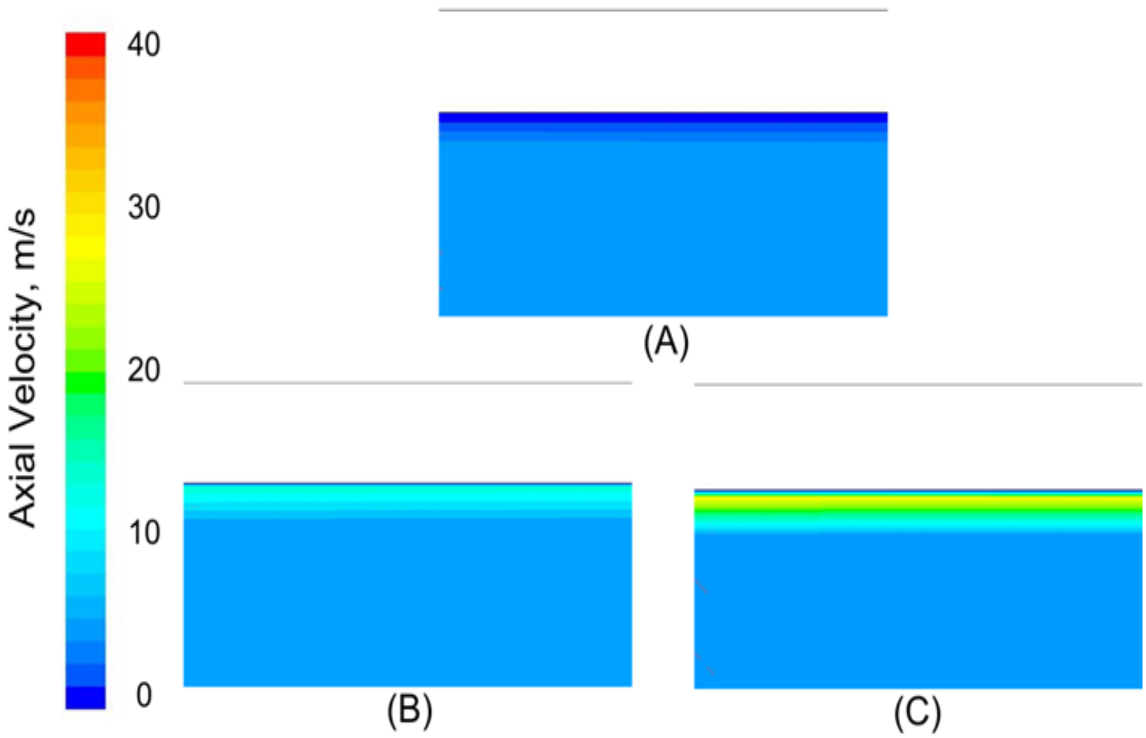

Figure 5.7 Velocity contours near the regenerator wall for (A) the base model, (B) the 10 μm defect model, and (C) the 20 μm defect model, all with 180 K cold tip temperature.

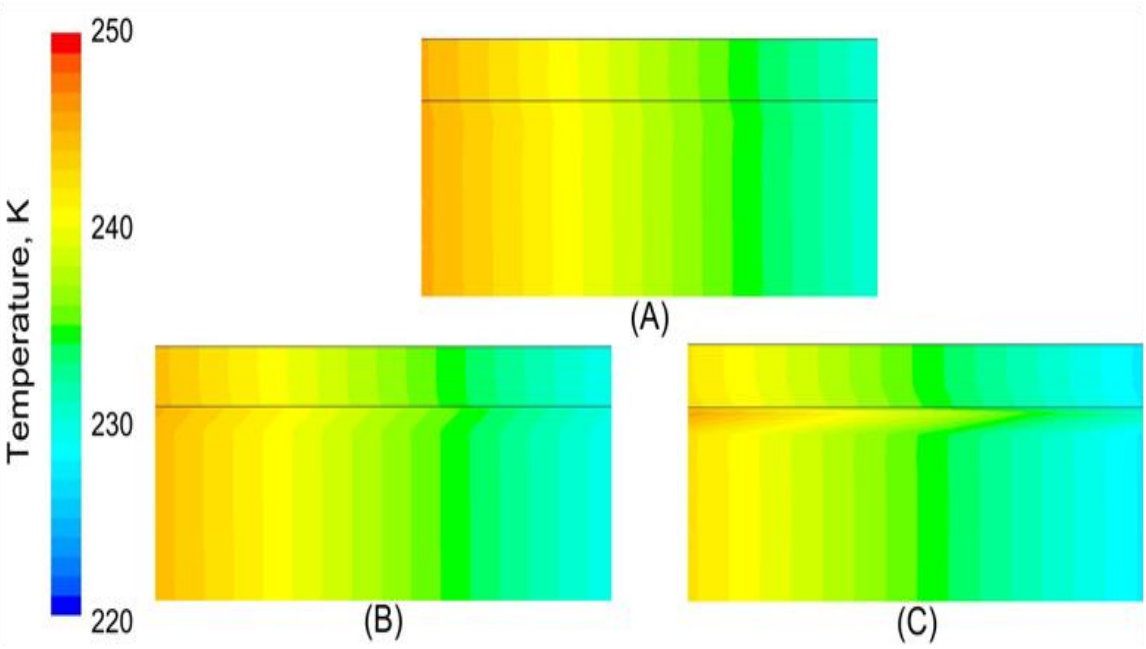

Figure 5.8 Temperature contours near the regenerator wall for (A) the base model, (B) the 10 μm defect model, and (C) the 20 μm defect model, all with 180 K cold tip temperature.

Figure 5.7 and Figure 5.8 show instantaneous contours of axial velocity and temperature, respectively, for a small region near the regenerator wall, outlined in Figure 5.3. Both figures display model results at 0.1105 seconds of simulation time, at which point the velocity in the regenerator is at its cyclical maximum. Figure 5.7 shows that the effect of the open annular defects is to allow a higher velocity leakage of helium through the gaps around the regenerator. As would be expected, the width of this flow and its maximum velocity are both higher for the 20 μm gap (C) than the 10 μm (B). Figure 5.8 shows that the flow through the annular gap is warmer than that in the interior of the regenerator at the same axial position. Again the effect is more pronounced for the 20 μm gap, with significantly more penetration of warm gas into the colder end of the regenerator. At the opposite point in the cycle, not shown here, the maximum velocity in the other direction occurs; at this point the velocity and temperature distributions are reversed and colder gas penetrates the warmer end of the regenerator. The temperature and velocity plots, considered together, confirm that the regenerator annular defect presents a lower resistance flow path around the regenerator which allows the working fluid to partially bypass it. This in turn would result in enhanced heat transfer from the warm end of the regenerator to the cold end, increasing the regenerator loss and reducing the net cooling power of the PTC.

The results of these simulations clearly indicate that the width of the gap between the regenerator wire mesh screens and the inner wall of the regenerator shell is a critical parameter. The working fluid that bypasses the core and passes through the gap is not effectively regenerated, resulting in a direct shuttling loss. These results indicate that the magnitude of this loss increases significantly for defect widths greater than 15 μm, which

corresponds to ¾ of the pore diameter or δ/R of 0.01 for the simulated regenerator filler and diameter. In practice, this criterion may be difficult to achieve; examining the wire mesh screens shown in Figure 3.2, it is apparent that the edge of a cut screen is not going to be defined by a solid wire, but rather by a series of partial cells with characteristic dimensions between 0 and 1 pore diameter. This means that to effectively achieve a defect gap on the order of ½ pore diameter, line-to-line contact between the regenerator screen outer diameter and the shell is practically required; a gap of ¾ pore diameter therefore leaves little room for variation in the manufacturing process. Consequently, these results suggest that for miniature PTRs alternative regenerator materials for which these gaps may be reduced or eliminated will most likely be preferable.

5.1.3 Component Junction Tapering

Due to their relatively smaller volume and available cooling power, miniature cryocoolers are likely to be more sensitive to hydrodynamic losses than their full scale counterparts. Abrupt changes in diameter between cryocooler components are a possible source of such losses as flow separation and recirculation may occur at these points. Underutilization of regions of the regenerator and heat exchanger porous matrices may also occur due to jetting of fluid into these components. Simulations were performed to determine the effects of reducing or eliminating such abrupt diameter changes by tapering or chamfering the transitions between the various miniature cryocooler components.

As was the case for the regenerator defects, modeling multidimensional geometric features such as these tapers requires a multidimensional modeling approach and therefore these simulations were carried out with meso-scale system level CFD models.

A schematic identifying the tapered component junctions is shown in Figure 5.9, a detailed view of the applied taper is presented in Figure 5.10, and its lengths and depths are tabulated for the various models in Table 5.3. The ratios b/c and b/r in this table are the taper depth nondimensionalized by the step change in radius and the radius of the component being tapered, respectively. All other geometry and operating conditions for these models are the same as those presented in Table 5.1.

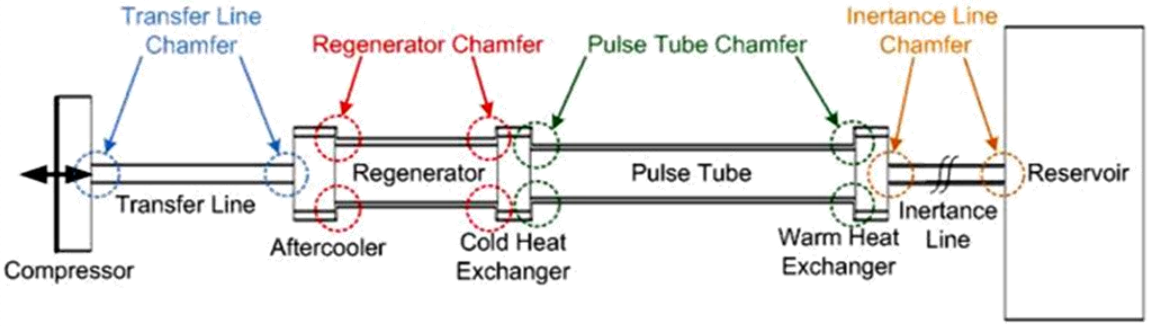

Figure 5.9 Schematic identifying tapered component junctions

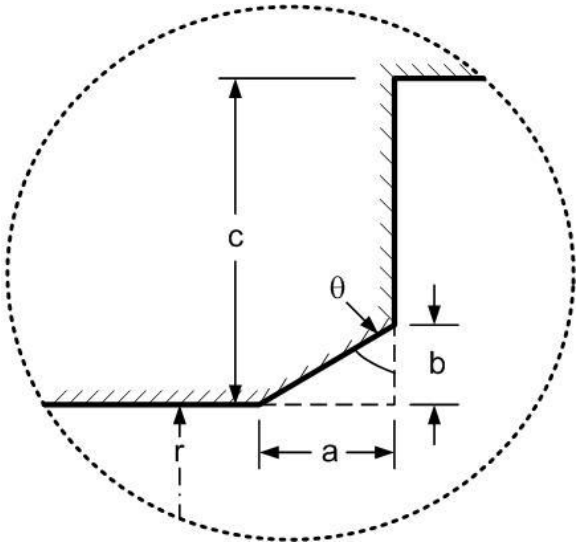

Figure 5.10 Detail view of tapers.

Table 5.3 Taper lengths and depths for various models

Model	Chamfer Dimensions							
	Transfer Line				Regenerator			
	a (mm)	b (mm)	b/c	b/r	a (mm)	b (mm)	b/c	b/r
45° Taper C	0.1	0.1	0.067	0.2	0.25	0.25	0.5	0.167
45° Taper B	0.2	0.2	0.133	0.4	0.5	0.5	1	0.333
45° Taper A	0.5	0.5	0.333	1	0.5	0.5	1	0.333
60° Taper A	0.866	0.5	0.333	1	0.866	0.5	1	0.333
75° Taper A	1.866	0.5	0.333	1	1.866	0.5	1	0.333

Model	Pulse Tube				Inertance Line			
	a (mm)	b (mm)	b/c	b/r	a (mm)	b (mm)	b/c	b/r
45° Taper C	0.25	0.25	0.333	0.2	0.1	0.1	0.067	0.2
45° Taper B	0.5	0.5	0.667	0.4	0.2	0.2	0.133	0.4
45° Taper A	0.75	0.75	1	0.6	0.5	0.5	0.333	1
60° Taper A	1.3	0.75	1	0.6	0.866	0.5	0.333	1
75° Taper A	2.8	0.75	1	0.6	1.866	0.5	0.333	1

As shown in Table 5.3, the effect of the taper depth was investigated using the 45° models and the effect of the taper angle was investigated with models having the maximum depths for each component junction. Additionally, simulations were performed in order to determine the contribution of each individual component junction taper on the predicted cryocooler performance. These models used the 45° chamfer geometry given above for the investigated junction and sharp edged transitions, as used in the base model, for the remaining connections. The effects of these tapers on the overall system performance characteristics of predicted net cooling and efficiency are presented first, followed by detailed vector and contour plots of specific regions which give some explanation to the observed differences in simulated performance.

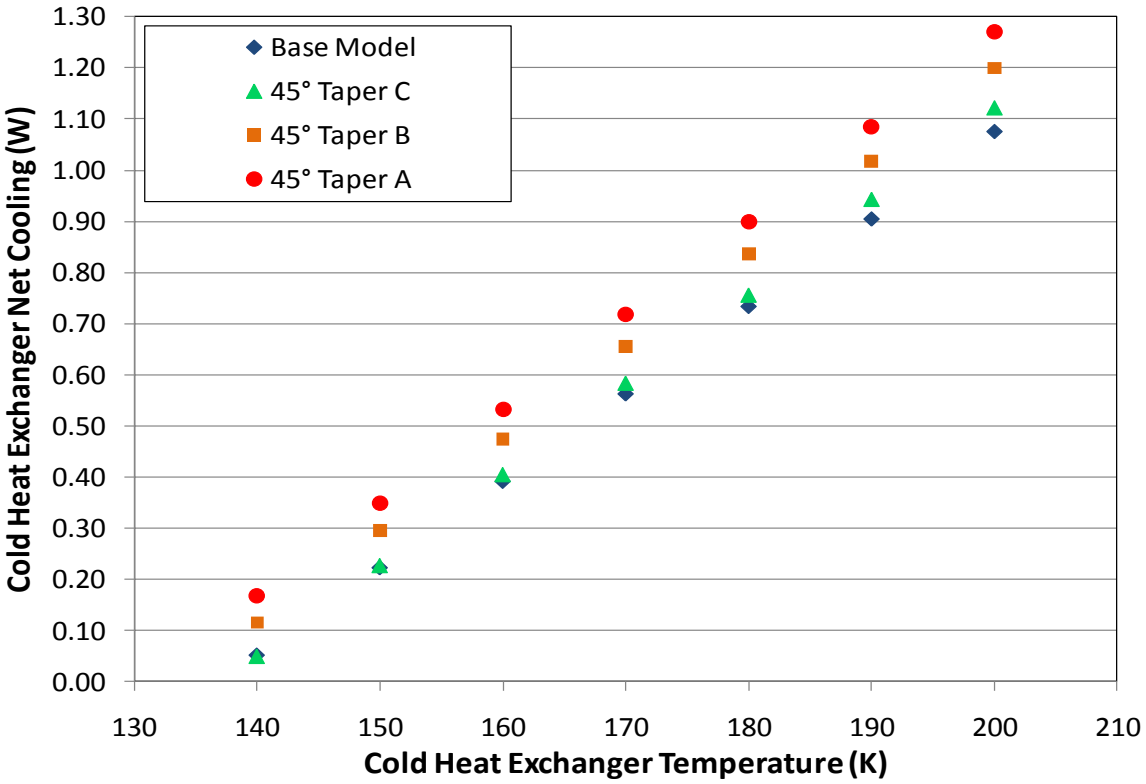

Figure 5.11 Simulated load curves for 45° taper models, various depths

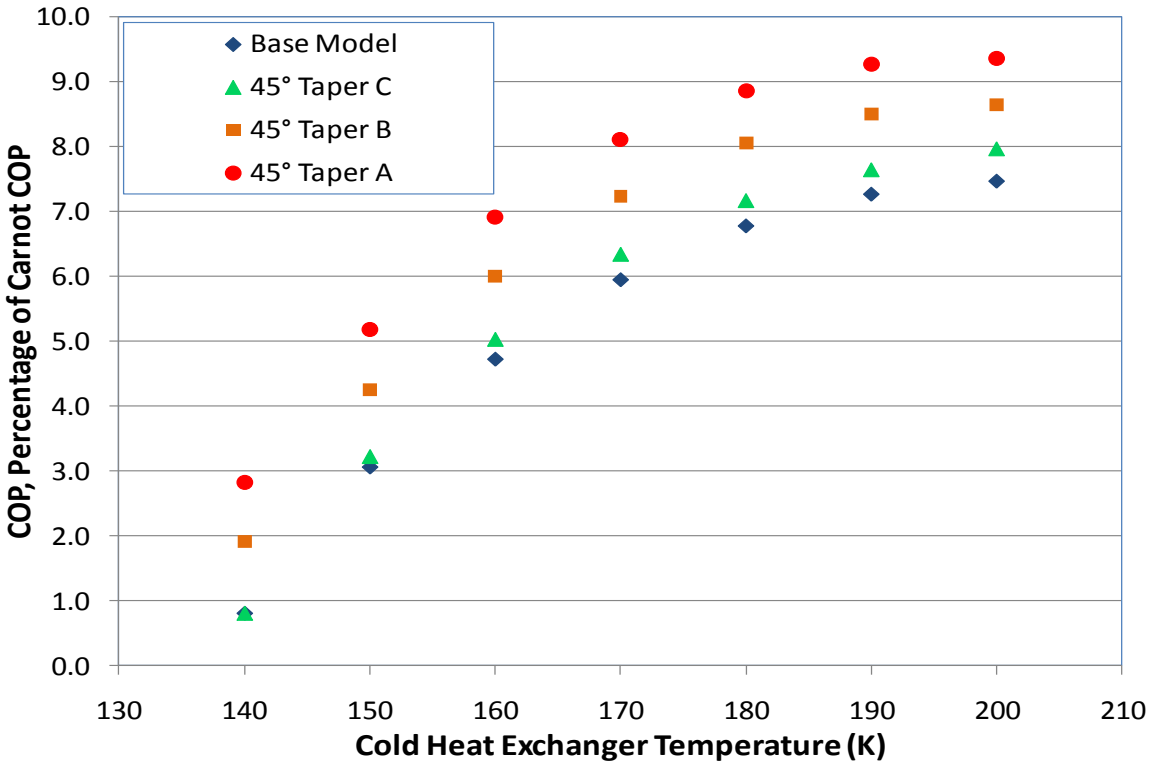

Figure 5.12 COP as a percentage of the Carnot COP for 45° taper models

Simulated load curves and plots of COP as a percentage of the Carnot COP are presented in Figure 5.11 and Figure 5.12, respectively, for the 45° taper models. From these results it is apparent that the predicted performance increases significantly as the chamfer depth is increased. Across the range of simulated cold tip temperatures the 45° Taper A model, which has the largest taper depths, is predicted to produce 0.1 to 0.2 W of additional cooling and an increase in COP of approximately 2% of Carnot relative to the base model. This increase in COP results not only from the increase in net cooling but from a decrease in the calculated PV power input from the compressor, discussed in more detail with the vector and contour plots presented later.

In order to determine the effect of the taper angle on the predicted PTR performance, load curves were also simulated for the 60° Taper A and 75° Taper A models. These are shown along with the results for the base model and 45° Taper A model in Figure 5.13; their COP as a percentage of the Carnot COP is shown in Figure 5.14. These results indicate that although increasing the taper angle from 45° to 60° has little effect on the predicted performance, the further increase in angle to 75° leads to a significant additional gain in heat lift and COP.

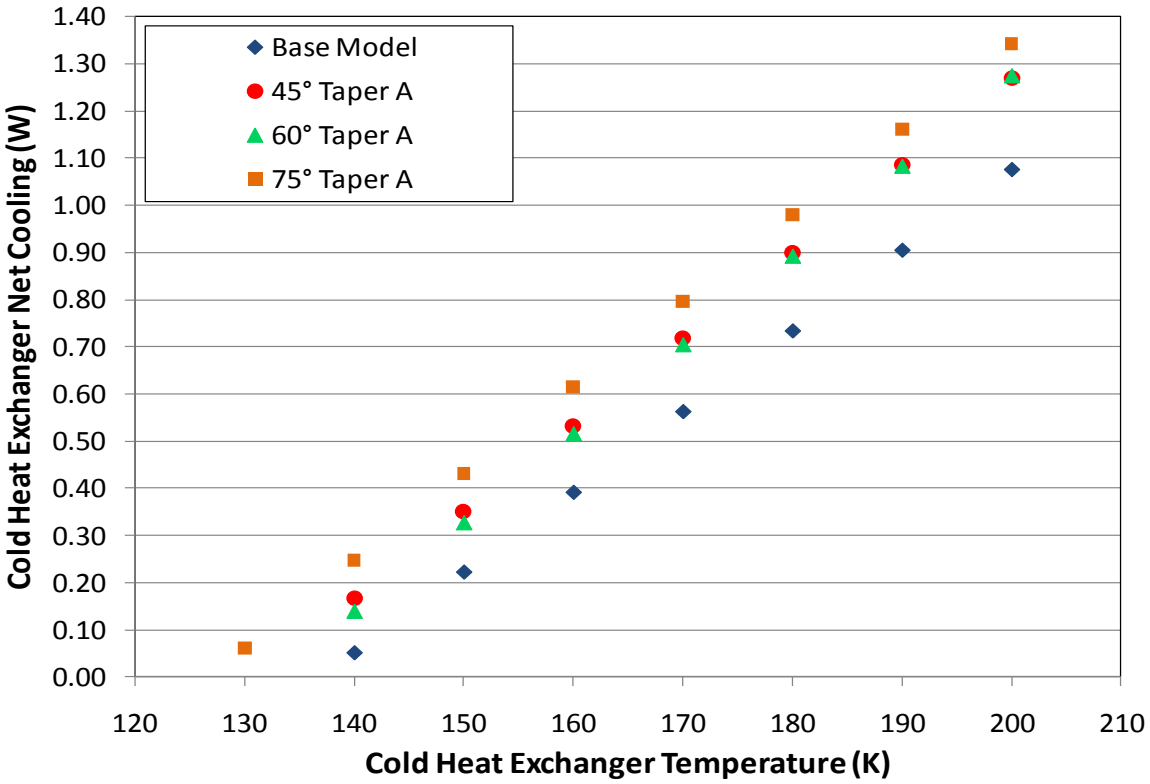

Figure 5.13 Simulated load curves for taper models, various taper angles

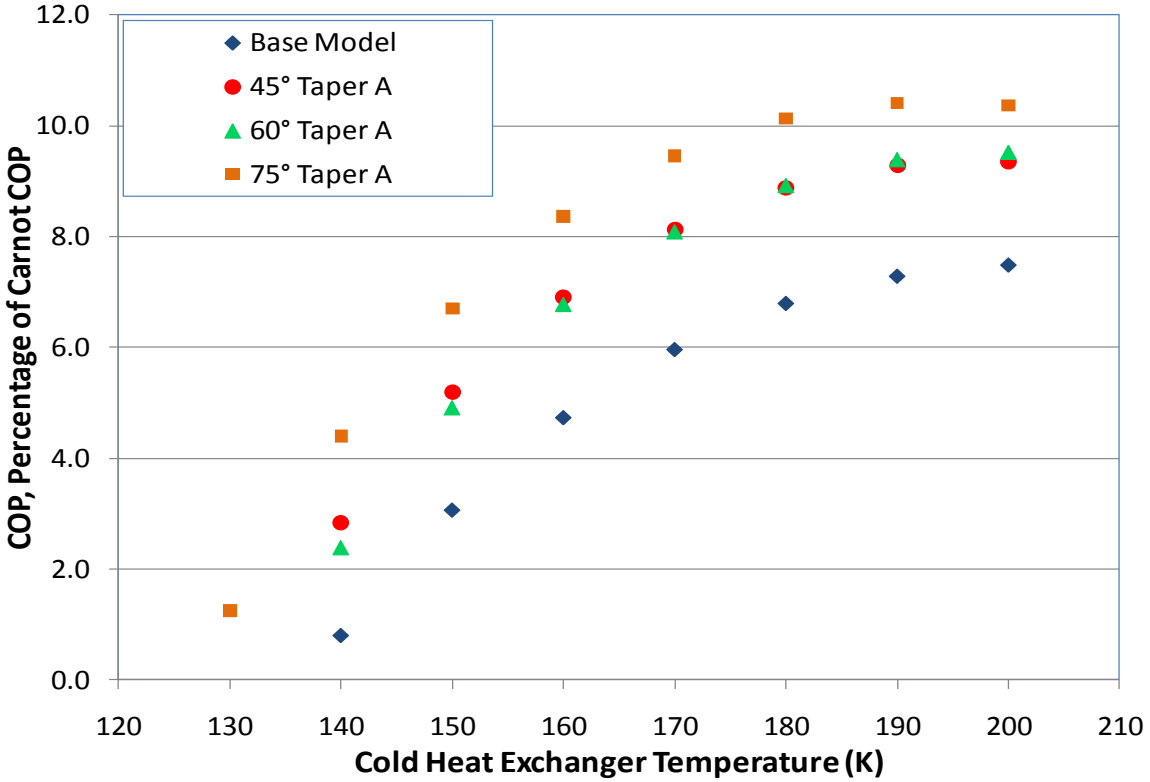

Figure 5.14 COP as a percentage of the Carnot COP for taper models, various taper angles

The individual effects of the component junction tapers, investigated with the 45° chamfer models for a 180 K simulated cold tip temperature, are shown in Figure 5.15. From this figure it is apparent that the tapering applied to the pulse tube has the most significant effect on the predicted PTR net cooling; additionally, there is also a smaller improvement due to the tapering of the transfer line between the compressor and aftercooler. The regenerator taper appears to provide little to no benefit and the presence of the inertance line taper results in a slight increase in predicted performance which is insensitive to the taper depth.

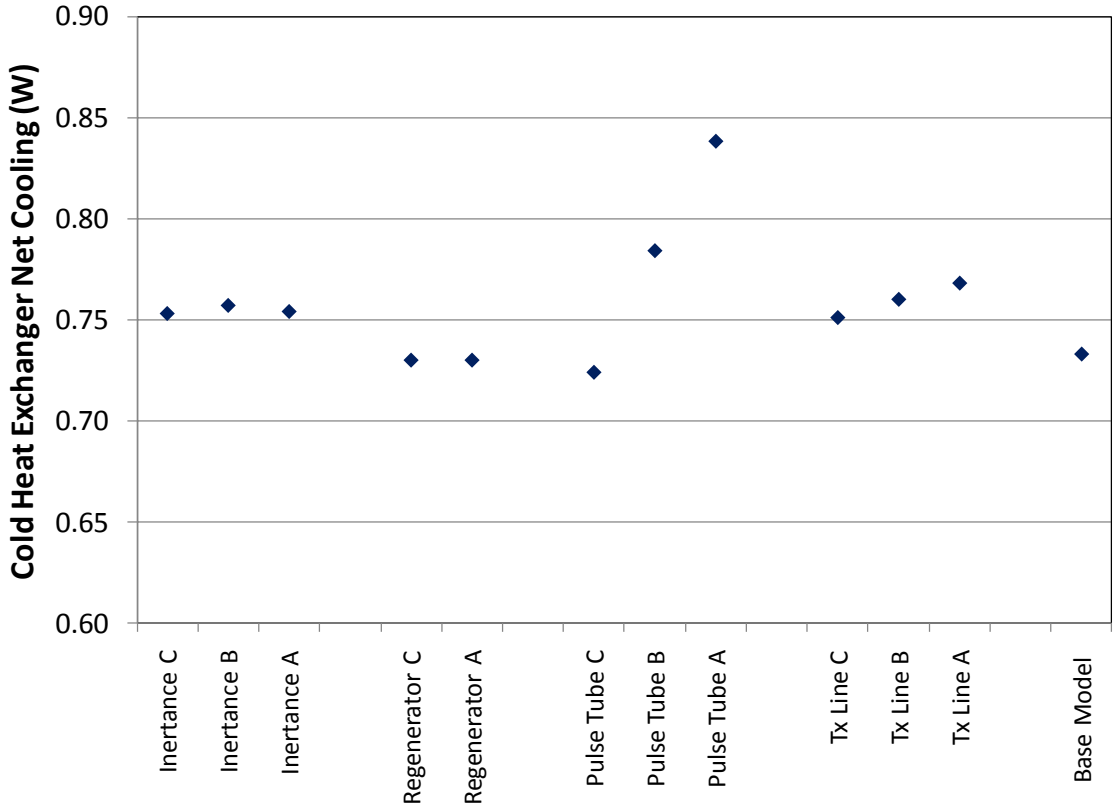

Figure 5.15 Predicted net cooling for 180 K cold tip temperature, 45° individually tapered junctions

In order to reveal the mechanisms by which the tapers may be improving the predicted PTR performance, detailed representations of the simulated flow in the CFD models have been produced. Contour and vector plots are presented which reveal some of the effects of the tapers on simulated flow believed to be responsible for the increases observed in their predicted overall performance. The transfer line and aftercooler are examined first in Figure 5.16 and Figure 5.17, which depict instantaneous contours of velocity and oscillatory pressure for the base and 75° Taper A models at the point in their cycles corresponding to the maximum velocity at the aftercooler inlet.

From these figures it is apparent that although the maximum velocity in the transfer line is higher for the tapered model, the pressure drop across the transfer line is significantly lower. The reduction in oscillatory pressure depicted in Figure 5.17 results in a decrease in the pressure ratio predicted at the compressor. This in turn results in the lower calculated input powers which were partially responsible for the variation in the predicted COP results shown in Figure 5.12 and Figure 5.14. To further quantify this effect, the pressure ratios at the inlets of the transfer line and pulse tube are given in Table 5.4 for the base model and selected taper models. Also included in this table are the oscillatory mass flow rate amplitudes at the same locations and the calculated input PV powers. The inlet pressure ratio and input power presented in the table decrease as tapers of increasing angle are applied. The pressure ratio at the pulse tube inlet and the mass flow rate amplitudes at both locations, however, are slightly greater than or equal to those predicted for the base model. Therefore, the tapered models would be expected to predict similar or slightly greater heat lift than the base model despite their lower input powers.

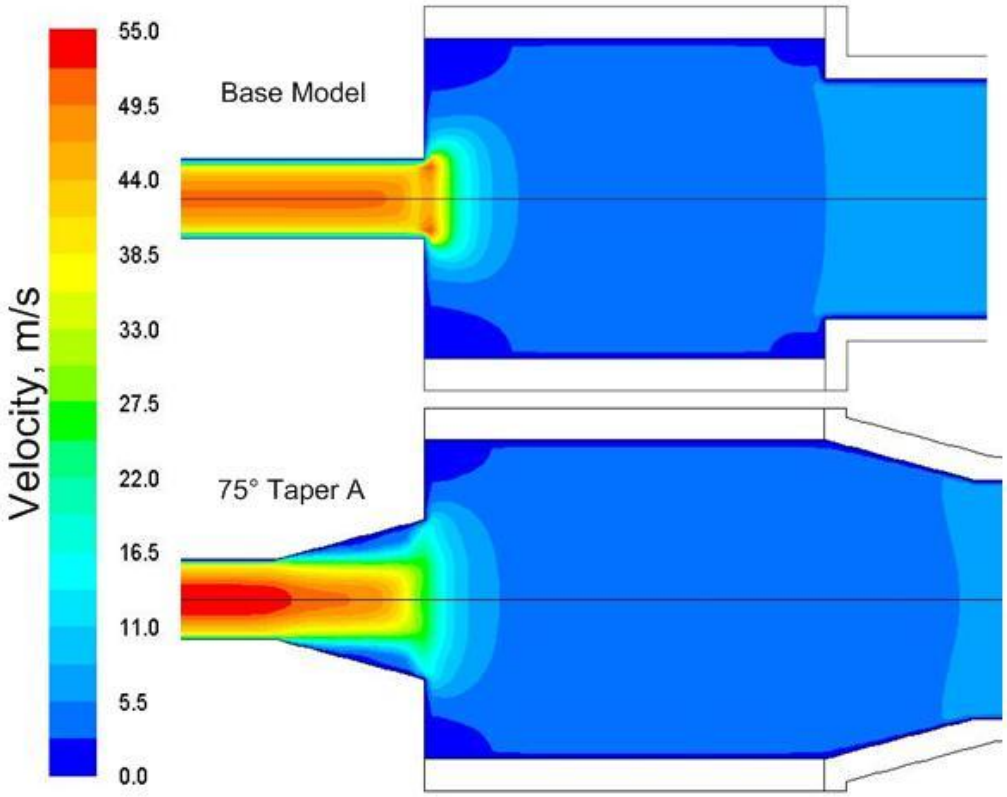

Figure 5.16 Contours of velocity in the transfer line and aftercooler, 180 K cold tip temperature

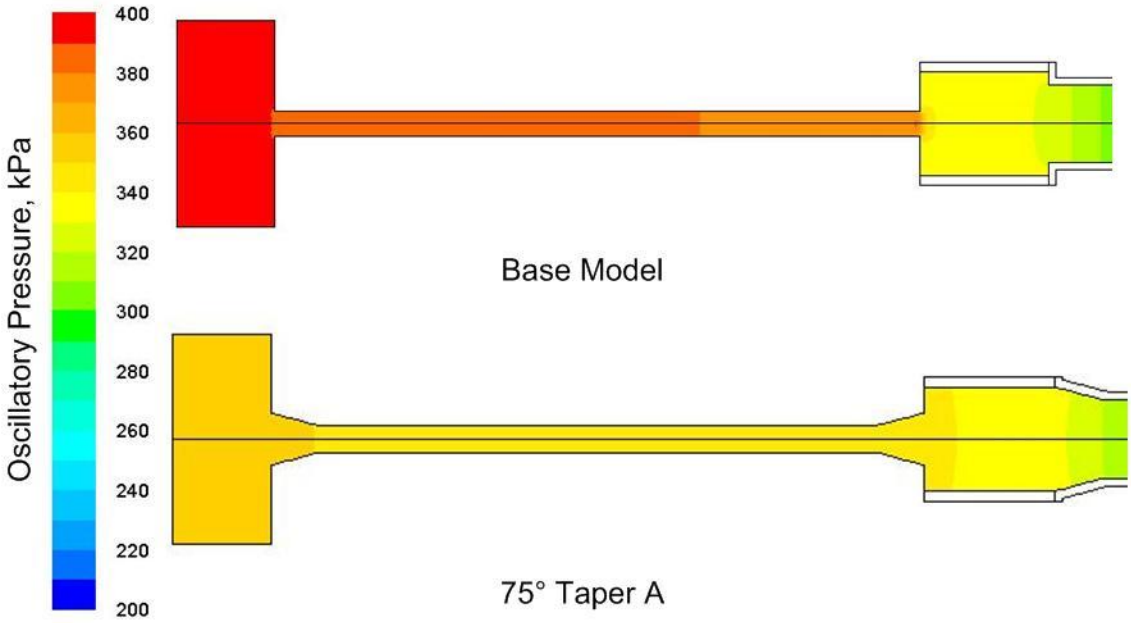

Figure 5.17 Contours of oscillatory pressure in the compressor, transfer line and aftercooler, 180 K cold tip temperature

Table 5.4 Pressure ratios, mass flow rate amplitudes, and input PV powers for selected models, 180 K cold tip temperature

Model	Pressure Ratio		Mass Flow Rate Amplitude, g/s		Input PV Power, W
	Inlet	Pulse Tube	Inlet	Pulse Tube	--
Base Model	1.254	1.132	0.211	0.179	6.784
45° Taper A	1.236	1.135	0.217	0.183	6.367
60° Taper A	1.234	1.136	0.217	0.182	6.285
75° Taper A	1.228	1.134	0.219	0.179	6.074

Additionally, Figure 5.16 shows that the low velocity regions in the corners of the aftercooler of the base model have been significantly reduced in size or eliminated in the tapered model. Regions such as these where the flow is minimal are essentially dead volume: they do not contribute to the cooling produced by the PTR but still require work input for oscillatory compression of the gas that they contain.

Because the tapering applied to the pulse tube was identified in Figure 5.15 to have the greatest effect on the overall model performance, the flow patterns at the junction of the pulse tube and cold heat exchanger are examined in Figure 5.18. This figure depicts instantaneous vector plots of simulated velocity at the point in the oscillatory flow cycle when the average velocity magnitude at the pulse tube inlet is at its maximum value. It shows that the flow entering the pulse tube becomes more uniform both when the 45° taper is applied and again when its angle is increased to 75°. Significant non-uniformity is seen in the predicted flow for the base model due to the presence of the sharp corner. For the 45° taper model, the simulated flow at the pulse tube entrance is more uniform but it is still disturbed by the edge of the taper inside the pulse tube. The 75° taper model, however, exhibits a predicted flow pattern that is much more uniform throughout the entire transition. Similar patterns are seen a half cycle later when

the flow reverses directions and also at the warm end of the pulse tube where it joins the warm heat exchanger. These more uniform predicted flow patterns in the pulse tube are believed to be partially responsible for the increase in the simulated net cooling and COP reported for the tapered PTR models.

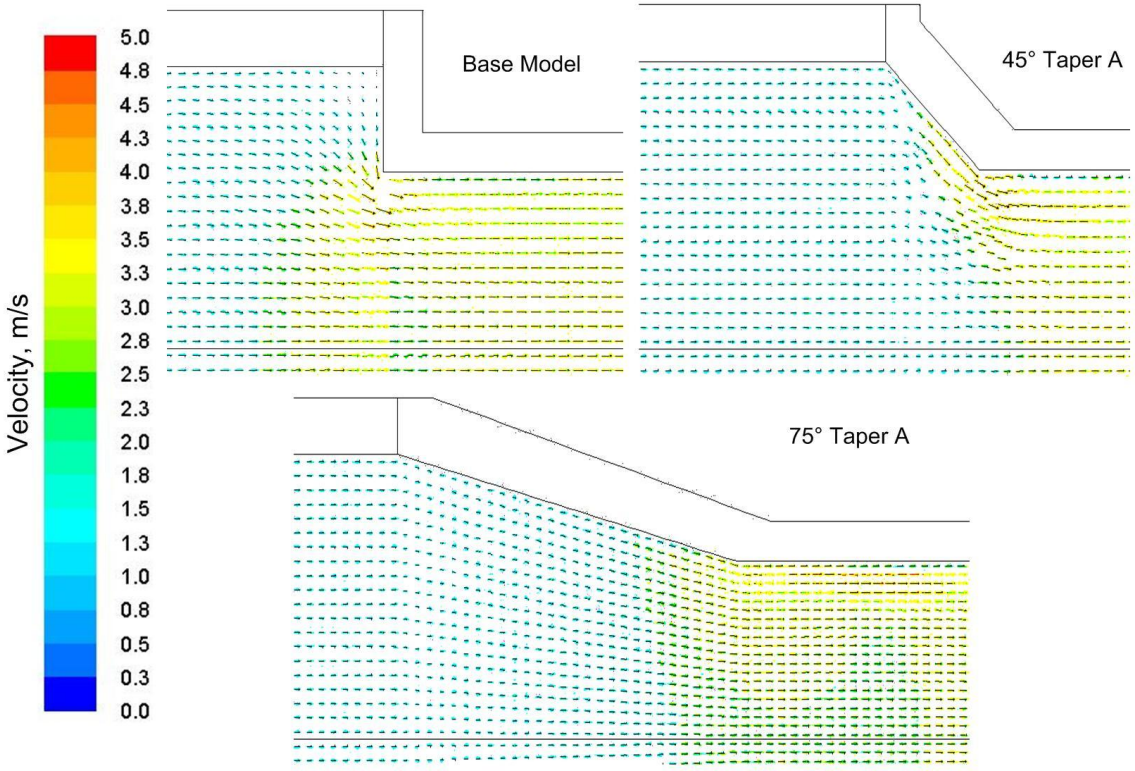

Figure 5.18 Vector plots of velocity, junction of cold heat exchanger and pulse tube, 180 K cold tip temperature

5.2 Pulse Tube Component Level Models

As discussed in Chapter 2, miniaturized pulse tubes may experience enhanced heat and momentum transfer between their working fluid and walls, as well as enhanced acoustic streaming losses due to their likely larger boundary layer thickness to diameter ratios. A parametric study was performed with component level CFD models of the pulse tube and its adjoining heat exchangers in order to characterize the effects of the thermal and viscous boundary layers in this critical component. The schematic for these models is shown in Figure 4.9 and their boundary conditions and other parameters are described in Chapter 4.

In this parametric study, the ratio of the two boundary layer thicknesses to the pulse tube diameter was varied and losses resulting from thermal and viscous interactions between the working fluid and walls were quantified. The relevant boundary layer thicknesses are the thermal and viscous penetration depths, δ_T and $\delta_{V,}$ the orders of magnitude of which are defined in Eq. 2.1 and 2.2, respectively. These two quantities are related by the Prandtl number as shown in Eq. 5.3 below. The ratio δ_V/D is closely related to another dimensionless parameter, the Womersley number, which is defined in Eq. 5.4.

$$\delta_T = {\delta_V}\Big/{\sqrt{Pr}} \tag{5.3}$$

$$Wo = \frac{D}{2}\sqrt{\frac{\omega\rho}{\mu}} \tag{5.4}$$

$$\frac{\delta_V}{D} = \frac{\sqrt{2}}{Wo} \tag{5.5}$$

Models were constructed with pulse tube diameters of 1, 2, and 4 mm and operating frequencies of 100, 200, 300 and 400 Hz in order to investigate a range of δ_T/D and δ_V/D values from approximately 0.01 to 0.1. Mean values of the thermal and viscous penetration depths, evaluated for helium at the mean temperature of 240 K, are shown in Table 5.5 for each of the investigated frequencies. Values of δ_T/D and δ_V/D, also for the mean temperature of 240 K, are presented for all of the models in Table 5.6.

Table 5.5 Thermal and viscous penetration depths for helium at 4 MPa and 240K

Penetration Depths (mm)		
f	δ_T	δ_V
100	0.103	0.084
200	0.073	0.059
300	0.060	0.048
400	0.052	0.042

Table 5.6 Values of δ_T/D and δ_V/D for the investigated frequencies and pulse tube diameters at 240 K

	Pulse Tube Diameter (mm)					
	1		2		4	
f	δ_T/D	δ_V/D	δ_T/D	δ_V/D	δ_T/D	δ_V/D
100	0.103	0.084	0.052	0.042	0.026	0.021
200	0.073	0.059	0.037	0.030	0.018	0.015
300	0.060	0.048	0.030	0.024	0.015	0.012
400	0.052	0.042	0.026	0.021	0.013	0.010

The remaining geometry for the pulse tube component level models was chosen to be representative of typical miniature PTRs. Pulse tube lengths of 20 mm and warm and cold heat exchanger lengths of 5 mm were used for all of the models, regardless of

diameter. Similarly, thicknesses of 0.25 mm were used for the pulse tube and heat exchanger walls.

The performance of the miniature pulse tube models was evaluated by comparing their net and gross cooling rates to those of corresponding 'ideal' models. The ideal models had adiabatic internal pulse tube walls and viscosities which were artificially reduced by a factor of 1000. All other boundary conditions and model parameters were unchanged, resulting in models which were essentially one-dimensional with negligible boundary layer effects. This is demonstrated in the velocity profiles shown in Figure 5.19 and the temperature profiles shown in Figure 5.20.

Figure 5.19 shows simulated instantaneous profiles of axial velocity for a cross section located at the midpoint of the pulse tube. Profiles are shown for the 200 Hz, 2 mm diameter ideal case and three δ_V/D values corresponding to the 200 Hz cases for each of the three pulse tube diameters. The radial position was nondimensionalized using the pulse tube inner radius. The profiles displayed correspond to a time step at which the mass flow rate at the warm end of the pulse tube is at its cyclical maximum. Due to the phase shift occurring across the pulse tube, however, this is not exactly the time step corresponding to maximum velocity at the midpoint of the pulse tube and so the beginning of the flow reversal can be seen in the profile. The simulated results show nearly uniform flow for the ideal case and increasing viscous boundary layer thickness relative to the diameter as δ_V/D increases, indicating qualitative agreement of the model predictions with theory.

Similarly, Figure 5.20 shows simulated instantaneous profiles of temperature for the same cross section and time step. The ideal case is presented along with the same 200

Hz cases presented in the velocity profiles, although in this figure the models are identified by their δ_T/D values. Figure 5.21 shows contours of simulated temperature for the 2 mm diameter, 200 Hz ideal and standard models. From these two figures it can be seen that the ideal case has a nearly uniform predicted radial temperature distribution while thermal boundary layers are apparent for the non-ideal models. As was the case with the velocity profiles, the relative thickness of the simulated thermal boundary layer with respect to the diameter increased along with the δ_T/D parameter, again indicating model results in qualitative agreement with theoretical predictions.

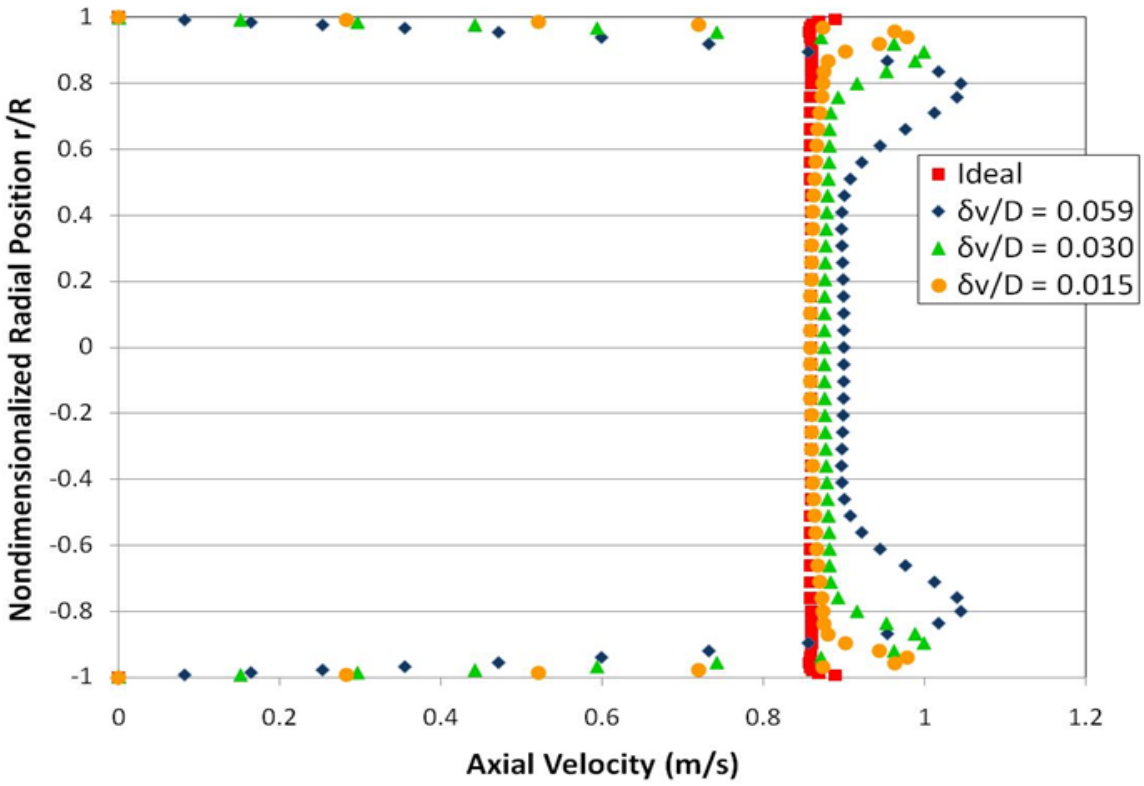

Figure 5.19 Simulated instantaneous velocity profiles, selected pulse tube models

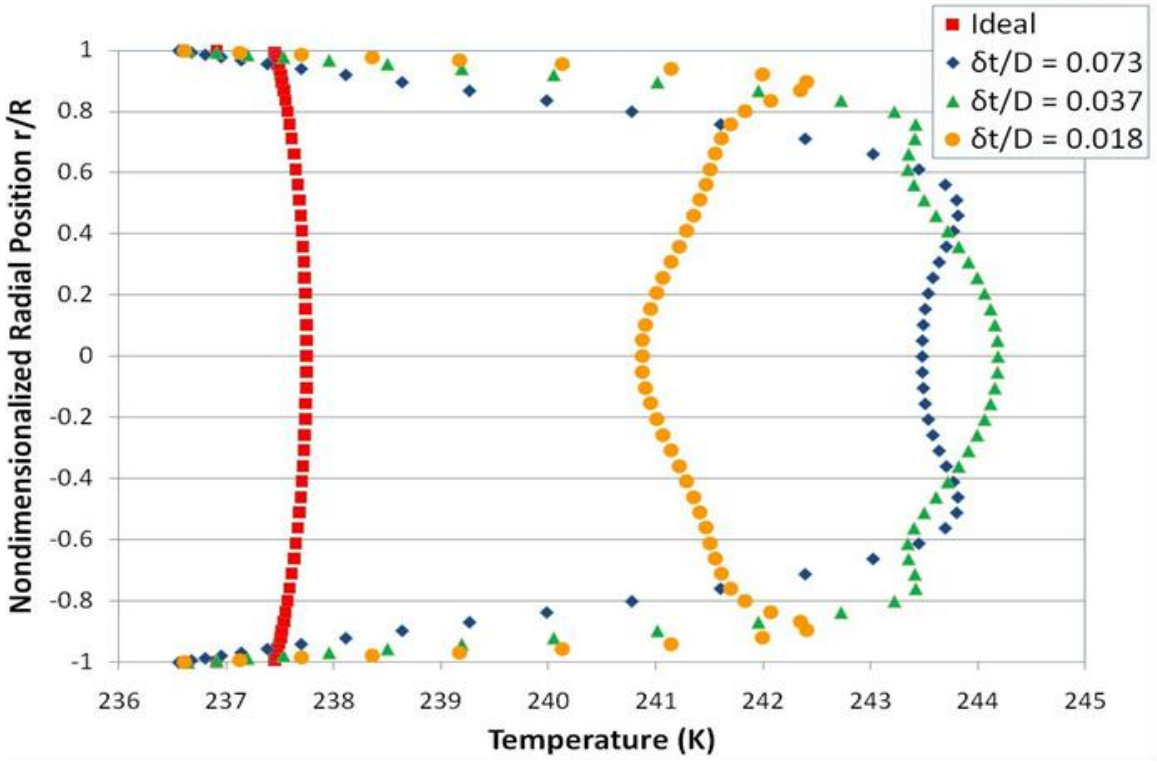

Figure 5.20 Simulated instantaneous temperature profiles, selected pulse tube models

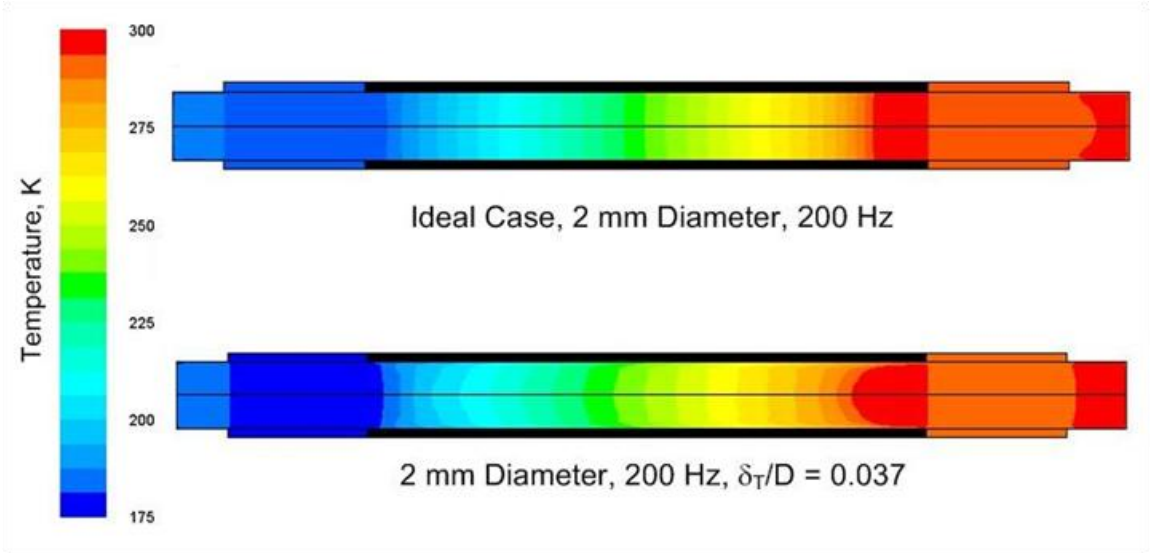

Figure 5.21 Simulated temperature contours, selected pulse tube models

The results presented in these three figures display the ability of the CFD models to capture the expected thermal and viscous boundary layer phenomena and also demonstrate the minimal presence of these phenomena in the ideal cases. The ideal cases may therefore be used for separating the losses attributable to the boundary layers from those which would occur regardless of their presence. For all of the cases, net and gross cooling rates were evaluated from the cycle-averaged enthalpy flow rates at the warm and cold ends of the pulse tube, respectively, labeled <Hwhx> and <Hchx> in Figure 4.9. These are evaluated using surface monitors of the flow rate of Fluent's 'total enthalpy' field variable. The boundary layer loss for each model was defined as the difference between its predicted net cooling rate and that of the corresponding ideal case. The model's gross cooling rate was then used to normalize the boundary layer loss.

The results of the entire set of pulse tube models are presented in this form in Figure 5.22. Predicted boundary layer losses, normalized by the corresponding gross cooling rates, are plotted as a function of thermal boundary layer thickness divided by the pulse tube diameter (δ_T/D). The results show that the simulated boundary layer loss increases nearly linearly with δ_T/D, ranging from less than 10% to 70% of the maximum available heat lift. Losses of approximately 10%, calculated for δ_T/D below 0.02, are considered typical for conventional scale PTCs and are likely acceptable for miniaturized PTCs as well. The higher losses predicted as δ_T/D approaches 0.1, however, would likely be prohibitive to obtaining useful cryogenic refrigeration. These results therefore provide interdependent criteria for the pulse tube diameter, mean pressure and operating frequency for the design of miniature PTRs. Reductions in the pulse tube diameter will require increases in mean pressure and/or operating frequency in order to maintain

efficient operation. In the following section, these relationships are used to scale the system level PTR models down to successively smaller sizes.

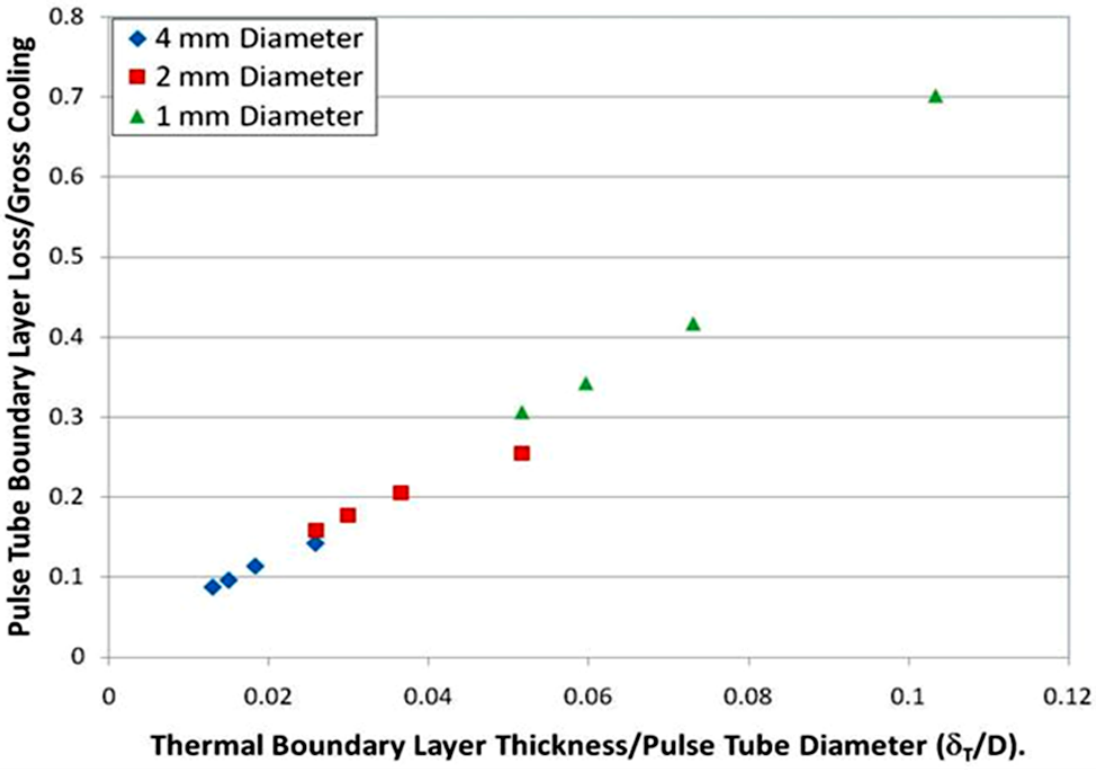

Figure 5.22 Normalized pulse tube boundary layer loss vs. δ_T/D

5.3 Micro Scale Models

To complete this investigation, the results of the previously described system and component level models were employed to create miniature PTR models at the micro-scale. Due to several challenges remaining for both the modeling techniques used and the practical construction of such devices, these models are intended to simply establish the feasibility of PTRs operating at significantly higher frequencies and smaller scales than

those which have recently been demonstrated. The scaling analysis performed in order to generate these models and the resulting geometry and operating conditions are presented first, followed by their simulated results.

5.3.1 Micro-Scale Model Scaling Analysis

Micro-scale models were created for operating frequencies of 400, 600, 800 and 1000 Hz. Their geometry and other operating parameters were generated by scaling those of the previously described meso-scale system level CFD models using these frequencies and other subsequently determined quantities. A cold temperature of 180 K was initially assumed during scaling due to uncertainty regarding the ultimate low temperature that the models would achieve. In retrospect a lower temperature could have been used as the performance predicted by the micro-scale models was much better than expected. No geometry optimization was performed for the micro-scale models other than determination of suitable inertance lengths using Sage; therefore, there is likely potential for improvement in their simulated performance. Nevertheless, the resulting micro-scale PTR designs take into account many of the considerations for minaiturization previously discussed in Chapter 2 along with the results of the other parts of this investigation in order to demonstrate the possibility of PTR operation at significantly increased operating frequencies and greatly reduced physical dimensions. The results presented here are tentative, however, since several issues must still be addressed before such micro-scale PTRs might be experimentally demonstrated.

With the operating frequencies established, the first component to be scaled was the compressor. In order to keep the input power reasonable for miniature devices and

allow for fair comparison between the various models, the compressor diameter and swept volume were reduced so that less than 10 W of input power was estimated for each operating frequency. These values were iteratively adjusted as the scaling analysis continued in order to maintain this estimated input power as the mean pressure was increased. The resulting swept volume was used to scale several of the components, including the reservoir volume, regenerator, pulse tube and heat exchangers. The ratio of component fluid volume to this swept volume will be denoted β and tabulated with the model geometry in Table 5.7 when relevant.

The pulse tube diameter was chosen so that the ratio of thermal boundary layer thickness to pulse tube diameter was less than 0.02, the criterion determined in the previous section. Values of δ_T/D and δ_V/D for the pulse tube of each model are given in Table 5.7 for the initially expected mean temperature of 240 K. In order to eliminate stepped transitions between components, the regenerator and heat exchanger diameters were identical to the pulse tube diameter. The lengths of these components were scaled to progressively smaller values, maintaining similar values of β, as the specified operating frequency increased.

The inertance and transfer line diameters were scaled using the viscous boundary layer thickness, evaluated at 293 K, and were tapered with 75° taper angles as defined in Figure 5.10. The ratio of this boundary layer thickness to their diameters is listed with their dimensions in Table 5.7. The transfer line length was constant for all of the models while the inertance tube length was optimized using Sage. The micro-scale PTR models resulting from this scaling analysis had total volumes of 0.141 to 1.153 cc, making them

roughly an order of magnitude smaller than any PTR which has recently been demonstrated.

These models were constructed in Fluent using the same system-level modeling techniques as the meso-scale system level models presented previously. Walls of stainless steel 0.04 mm thick were modeled for the regenerator and pulse tube while silver walls with the same thickness were used for the heat exchangers. Due to a lack of available closure relations for more suitable regenerator and heat exchanger fillers, the hydrodynamic parameters for stacked screens of #635 stainless steel and #325 phosphor bronze wire meshes were incorporated into the models. Time steps were chosen which resulted in 250 steps/period of oscillations at the operating frequency and the models were iterated for 5000 time steps, or 20 periods, before they were considered to be at periodic steady state and their results were evaluated.

Table 5.7 Geometry, operating conditions, and scaling parameters for micro-scale models

Model	Mean Pressure (MPa)	Compressor		Transfer Line			Aftercooler		
		Diameter (mm)	Stroke (mm)	Diameter (mm)	Length (mm)	δ_V/D	Diameter (mm)	Length (mm)	β
400 Hz	7	5	0.9	0.5	5	0.0768	2.2	4	1.73
600 Hz	10	4	0.7	0.34	5	0.0778	1.6	3	2.18
800 Hz	14	3.4	0.5	0.25	5	0.0784	1.3	2.5	2.04
1000 Hz	18	3	0.4	0.2	5	0.0782	1.1	2	2.22

Model	Regenerator				Cold Heat Exchanger			Pulse Tube	
	Diameter (mm)	Length (mm)	β	ρC_p Ratio	Diameter (mm)	Length (mm)	β	Diameter (mm)	Length (mm)
400 Hz	2.2	10	0.596	56.83	2.2	3	1.42	2.2	15
600 Hz	1.6	9	0.625	38.55	1.6	2.5	1.62	1.6	12
800 Hz	1.3	7	0.631	27.88	1.3	2	1.60	1.3	9
1000 Hz	1.1	6	0.643	21.74	1.1	1.8	1.56	1.1	7

Model	Pulse Tube			Warm Heat Exchanger			Inertance Tube		
	β	δ_T/D	δ_V/D	Diameter (mm)	Length (mm)	β	Diameter (mm)	Length (mm)	δ_V/D
400 Hz	0.250	0.0180	0.0146	2.2	3	2.31	0.5	238.5	0.0768
600 Hz	0.295	0.0172	0.0139	1.6	2.5	2.61	0.34	120.9	0.0778
800 Hz	0.309	0.0158	0.0127	1.3	2	2.55	0.25	68.9	0.0784
1000 Hz	0.347	0.0157	0.0121	1.1	1.8	2.47	0.2	45.7	0.0782

Model	Reservoir				Total Volume (cc)
	Diameter (mm)	Length (mm)	Volume (cc)	β	
400 Hz	10	12	0.942	0.0188	1.153
600 Hz	8	10	0.503	0.0175	0.585
800 Hz	6	8	0.226	0.0201	0.266
1000 Hz	5	6	0.118	0.0240	0.141

Before the results of these models are presented, the limitations in the CFD modeling technique and challenges for practical construction of such PTRs should be acknowledged. As previously mentioned, there is a lack of available hydrodynamic parameters for more suitable materials for these models; this is partially because there are very few regenerator fillers available with hydrodynamic diameters small enough to operate effectively at the high frequencies and mean pressures required. Table 5.8 shows

the thermal penetration depths in helium at the frequencies and mean pressures used in the micro-scale models for a temperature of 180 K. Generally, for effective regeneration the pore diameter or hydraulic diameter of the passages in the filler material must be less than the thermal penetration depth in the working fluid; for the thermal penetration depths shown in Table 5.8 this requirement rules out all currently available mesh screen fillers and other regenerator fillers in common use. Additionally, following the discussion in Chapter 2 and the results of Radebaugh [28], the approximate ratio of the heat capacity of the stainless steel matrix filler to that of the displaced helium was.much lower than generally considered necessary for effective regeneration. For these reasons, practical construction of PTRs at these scales will require new porous fillers having a combination of small pore diameter, high thermal capacity, low pressure drop, and low thermal conductivity.

Table 5.8 Thermal penetration depths in helium, micro-scale model operating conditions at 180 K

Model	Mean Pressure (MPa)	δ_T 180 K (μm)
400 Hz	7	31.6
600 Hz	10	22.0
800 Hz	14	16.6
1000 Hz	18	13.4

An additional concern is that the Fluent porous media model utilized includes an assumption of thermal equilibrium betweeen the fluid and solid phases. While it is possible to model thermal non-equilibrium in porous media with Fluent, additional empirical relationships for the heat transfer coefficients are required which are difficult to

determine and may add more uncertainty to validity of the model results. The assumption of thermal equilibrium is more reasonable when the porous filler hydraulic diameter is much smaller than the thermal penetration depth in the fluid, as is the case for the meso-scale PTR models, than it is when the thermal penetration depth is of the order of the hydraulic diameter or smaller. For the frequencies and mean pressures used in the micro-scale models, poor heat transfer in the regenerator would be expected if the specified #635 mesh were actually used; this would result in significant losses due to regenerator ineffectiveness. Because of this assumption of thermal equilibrium in the porous regions, Fluent is unable to represent this loss and is therefore likely to overpredict the performance of the micro-scale PTRs if they are modeled with unsuitable regenerator fillers.

Finally, producing compressors with the displacement and operating frequencies specified for the micro-scale models presents a significant challenge. The required mean pressures and pressure ratios complicate this task even more. The models presented here are not intended to address this issue, but rather to demonstrate what might be possible if such compressors were to become available. Incorporating a compressor, such as a piezoelectric actuator, which is more reasonable for fabrication in the near term brings with it limitations which are undesirable for this idealized investigation of the extent to which miniaturization of PTRs may be possible.

5.3.2 Micro-Scale Model Results

To evaluate the performance of the micro-scale PTR models, simulated load curves of net heat lift vs. cold tip temperature are presented in Figure 5.23 and predicted

COPs are presented as a percentage of the Carnot COP in Figure 5.24. The performance predicted for these models is significantly better than that predicted for the meso-scale models; they all are predicted to reach ultimate cold tip temperatures below 100 K. Although this result seems counterintuitive there are several factors, discussed in the following paragraph, which are likely to contribute to this predicted increase in performance.

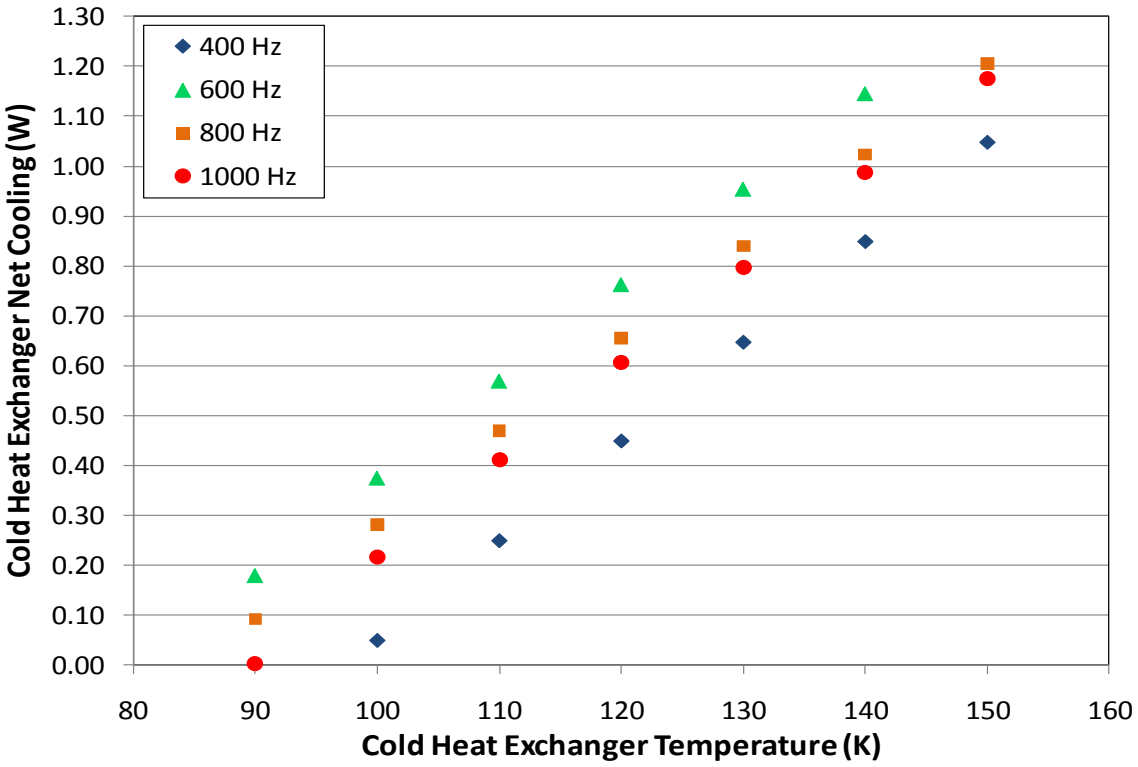

Figure 5.23 Simulated load curves for micro-scale PTR models

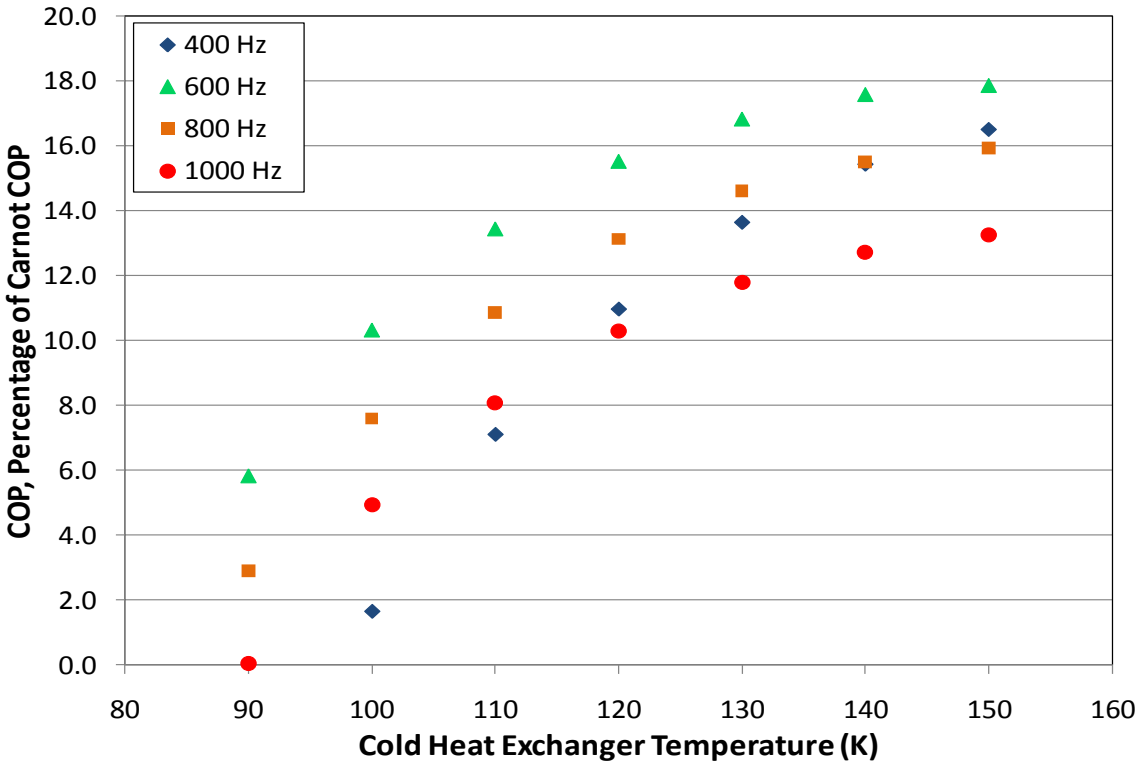

Figure 5.24 COP as a percentage of the Carnot COP for micro-scale models

First, although an effort was made to hold the input power relatively constant, the input PV powers and pressure ratios presented in Table 5.9 for the micro-scale models are generally higher than those calculated for the meso-scale models in Table 5.4. Additionally, the calculated thermal and viscous penetration depths are smaller relative to the pulse tube diameter for the micro-scale models than they are for those at the meso-scale, which were constructed before the results of the pulse tube component level models were obtained. The ratios of these penetration depths to the pulse tube diameter are given in Table 5.7 for the micro-scale models. Evaluated at the same temperature of 240 K for the meso-scale models, δ_T/D and δ_V/D are 0.0292 and .0237, respectively. Comparing these values against the results presented in Figure 5.22 reveals that the micro-scale models should have significantly lower normalized thermal and viscous

losses in their pulse tubes than those at the meso-scale. Finally, the pressure ratios at the pulse tube inlet for these models, shown in Table 5.9, are higher than those predicted for the meso-scale PTR models in Table 5.4, which would also be expected to result in increased predicted cooling.

Table 5.9 Pressure ratios and input PV powers for the micro-scale PTR models, 150 K cold tip temperature

Model	Pressure Ratio		Input PV Power (W)
	Inlet	Pulse Tube	
400 Hz	1.218	1.151	6.05
600 Hz	1.250	1.169	7.13
800 Hz	1.259	1.167	7.21
1000 Hz	1.301	1.165	8.46

Predicted phase angles between the pressure and velocity waveforms are tabulated at the inlet to each of the PTR components for the models with 150 K cold tip temperatures in Table 5.10. The simulated phase angles for most of the components decrease away from expected optimal values as the operating frequency increases. This indicates that either the intertance tube lengths predicted by Sage for these PTRs are not optimal for the CFD simulations or the inertance tube is becoming less effective as a phase shifting device as the frequency increases. Additional simulations, perhaps involving simple inertance tube optimization in Fluent, are needed to determine the reason for these variations in the predicted phase angles.

Table 5.10 Predicted phase angles between pressure and velocity, micro-scale PTR component inlets, 150 K cold tip temperature

	Simulated Phase Angles (Degrees)			
Model	Aftercooler	Regenerator	Cold Heat Exchanger	Pulse Tube
400 Hz	-25	-21	-4	4
600 Hz	-31	-28	-12	-3
800 Hz	-33	-30	-15	-6
1000 Hz	-33	-31	-16	-8

Model	Warm Heat Exchanger	Inertance Tube	Reservoir
400 Hz	40	47	-88
600 Hz	36	44	-88
800 Hz	32	40	-88
1000 Hz	28	36	-88

The results of these micro-scale models indicate that PTR operation at very high frequencies and greatly reduced scales may be feasible, providing that the challenges related to their regenerator fillers and compressors can be addressed. These models are highly idealized and their results are almost certain to be overly optimistic due to the previously discussed difficulties in modeling the regenerator and heat exchanger fillers. In spite of this, they still demonstrate the principles of PTR operation for coolers having total volumes as small as 0.141 cc. By addressing the majority of the considerations for miniaturization discussed in Chapter 2 and applying design criteria based on the physical phenomena expected to affect the operation of miniature PTRs, the scaling described in this section resulted in viable micro-scale PTR model geometry and operating conditions. Whether or not such coolers will ever be experimentally feasible will likely depend on the further development of miniaturized, high frequency compressors and suitable regenerator filler materials.

CHAPTER 6

CONCLUSIONS AND RECOMMENDATIONS

6.1 Conclusions

An investigation of the miniaturization of pulse tube refrigerators has been undertaken using a variety of numerical and experimental techniques. First, phenomena and processes expected to impact the performance of miniature PTRs were identified; some of these are unique to the miniaturized devices and others also affect conventionally scaled cryocoolers. A review of the experimental miniature PTRs which have been described in the open literature was performed and numerical modeling techniques suitable for predicting the performance of the miniature PTRs were presented. Numerical models of miniature PTRs were then constructed using both the Sage cryocooler modeling program and Fluent, a commercial CFD code. In support of this modeling effort, experiments were performed in order to determine directional hydrodynamic parameters characteristic of stacked screens of #635 stainless steel and #325 phosphor bronze wire mesh, two fine-mesh porous materials suitable for use in miniature PTRs. Complete system level and pulse tube component level CFD models incorporating these parameters were then employed to quantitatively estimate the effects of several of the previously identified phenomena expected to affect miniature PTRs. Finally, the results of these models were applied to produce successively smaller micro-scale PTR models having total volumes as small as 0.141 cc for which cooling was predicted at cryogenic temperatures.

Before the CFD models of miniature PTRs were constructed, a preliminary scaling analysis was performed using Sage. From the results of this scaling analysis Fluent models were constructed at the meso-scale, defined here as total PTR volume of less than 10 cc, and their results compared with those of Sage. Sage was found to predict higher performance than Fluent for identical model geometry and operating conditions; however, without experimental data the accuracy of the two modeling techniques for the miniature PTRs cannot be compared.

The meso-scale CFD models were then used to quantify the effects of imperfect contact between the regenerator mesh screens and the inner wall of the regenerator housing. Due to the morphology of the screens and necessary manufacturing tolerances for both screens and housing, imperfect contact is likely and may result in an annular region near the housing inner wall where the hydrodynamic resistance is significantly reduced. Such annular defects were simulated with the CFD models; the results show that the PTR models are relatively insensitive to gaps of up to approximately 1% of the regenerator radius, but as the gap width increases beyond this point the predicted PTR performance suffers significantly. In practice, this criterion may be difficult to achieve and thus these results suggest that for miniature PTRs alternative regenerator materials for which these gaps may be reduced or eliminated will most likely be necessary.

Similar meso-scale CFD models were also used to investigate the effects of eliminating sharp edged transitions between components of different diameter by tapering their junctions. The predicted net cooling and COP of the miniature PTR models were shown to increase as these tapers were applied and as their angles were increased from 45° to 75°. Tapering of the pulse tube had the most pronounced effect on the predicted

performance and was shown to reduce non-uniformity of the simulated flow as it entered and exited that component. Tapering of the transfer line between the compressor and aftercooler was also shown to result in a decrease in the simulated pressure drop across its length, leading to a reduction in the inlet pressure ratio and input PV power. These results suggest that sharp edged transitions between PTR components should be avoided if possible, although for physical PTRs this may sometimes be difficult due to practical fabrication considerations.

A parametric study was performed with component level CFD models of the pulse tube and its adjoining heat exchangers in order to characterize the effects of the thermal and viscous boundary layers in this critical component. In this parametric study, the ratio of the two boundary layer thicknesses to the pulse tube diameter was varied and losses resulting from thermal and viscous interactions between the working fluid and walls were quantified. Models were constructed with pulse tube diameters of 1, 2, and 4 mm and operating frequencies of 100, 200, 300 and 400 Hz in order to investigate a range of δ_T/D and δ_V/D values from approximately 0.01 to 0.1. For a value of δ_T/D of approximately 0.02, losses of 10% of the gross cooling were predicted; this is considered typical for conventional scale PTCs and is likely acceptable for miniaturized PTCs as well. The predicted losses increased as δ_T/D increased beyond this point, however, to levels which are likely prohibitive for obtaining useful cryogenic refrigeration. Thus the results of this parametric study indicate that δ_T/D should remain less than approximately 0.02 for efficient pulse tube operation.

Finally, the results of the system and component level CFD models were employed to create PTR models at the micro-scale, defined here as having total volume

of approximately 1 cc or less. Due to several challenges remaining for both the modeling techniques used and the practical construction of such devices, these models are intended to simply establish the feasibility of PTRs operating at significantly higher frequencies and smaller scales than those which have recently been demonstrated. Micro-scale models were created for operating frequencies of 400, 600, 800 and 1000 Hz, taking into account many of the considerations for minaiturization previously identified. These had total volumes between 0.141 and 1.153 cc, making them approximately an order of magnitude smaller than any PTRs which have recently been experimentally demonstrated. Excellent performance was predicted for these modeled PTRs, with cold tip temperatures of under 100 K reached for each of the operating frequencies. The results of these micro-scale models indicate that PTR operation at very high frequencies and greatly reduced scales may be feasible, providing that the challenges related to their regenerator fillers and compressors can be addressed

6.2 Recommendations for Future Work

In the course of this investigation, several areas were identified where improvements might have been made if not for the limitations of equipment, time, and a desire to keep the scope of the investigation manageable. These will be discussed in the following paragraphs along with possible directions for the continuation of this work.

In the experiments performed to determine the hydrodynamic parameters of the #635 stainless steel and #325 phosphor bronze wire screens, the range of frequencies achievable with the available compressor corresponded poorly with those of interest for

miniature PTRs. Low pressure amplitudes and oscillatory mass flow rates at the higher investigated frequencies made precise determination of the hydrodynamic parameters difficult. Repetition of these experiments using a compressor better suited to high frequencies would therefore be useful.

For the Sage and CFD modeling efforts, experimental validation of the model results is still needed. Conclusions regarding the accuracy of these models at the miniature scale must be drawn carefully until experimental results are available. Additionally, extension of the CFD modeling techniques used in this investigation to incorporate thermal nonequilibrium between the solid and fluid phases of porous media would be a significant advancement for cryocooler simulation.

The micro-scale PTR results are currently tentative due in large part to concerns regarding the suitability of the modeled regenerator and heat exchanger fillers and the accuracy of their representation in the Fluent porous media model. Incorporating more suitable regenerator fillers, such as parallel tubes with appropriate diameters, into these models would therefore improve the confidence in their results. Hydrodynamic parameters for these parallel tubes might be determined using direct numerical simulation, which is not feasible for randomly oriented wire meshes.

Additionally, because the presented micro-scale models were intended only to demonstrate feasibility of operation at the investigated high frequencies and reduced scales, significant additional analysis remains to be done at these scales. Initially, the mean pressure has been specified for each investigated frequency and the dimensions of the PTR components were then scaled based on these parameters and others derived from them. A more thorough investigation, including geometrical optimization and additional

parametric variations of charge pressure and frequency, should certainly be performed. Furthermore, the sensitivity of the micro-scale performance predictions to uncertainty in the model hydrodynamic parameters and additional losses in individual components should be determined.

Although they did not yield useable results and were therefore not presented here, preliminary 3D simulations of PTRs were carried out during this investigation in an attempt to model a variable gap around a regenerator which was offset from the axis of symmetry of the rest of the cryocooler. These simulations required an infeasible amount of computational time and converged much more slowly towards periodic steady state due to their large number of computational nodes. Such 3D simulations are needed for cryocoolers, however, and might be performed successfully in the future through the use of more computationally efficient modeling techniques or the application of high performance computing resources.

Finally, the miniature pulse tube refrigerators which were simulated in this investigation were all single stage devices. The possibility of building multi-stage miniature PTRs was not examined, nor was the option of staging them off of larger coolers. Such multistage configurations may allow these miniature cryocoolers to reach significantly colder temperaturs and should be explored in the future.

APPENDIX A

SAMPLE MATLAB PROGRAM FOR POST-PROCESSING

HYDRODYNAMIC PARAMETERS

The following function plots experimental and simulated waveforms for the experiments performed to determine oscillatory flow hydrodynamic parameters for porous materials. Pressure amplitudes and phase angles between inlet and outlet waveforms are calculated and printed to the command line.

```
function null = axial_ss_400psig_100_Hz_hiflow(dt);

%Matlab program for semi-automated post processing of Fluent results to
%determine porous media hydrodynamic parameters.

freq = 100;
omega = 2*pi*freq;

%FFT representation of experimentally measured oscillatory pressure data
%These are input for each Fluent case file and correspond to an individual test
p1m1 = 56475.336702;
p1m2 =   209.115925;
p1m3 =   349.628479;
p1phi1 =    -1.424009;
p1phi2 =    -2.917525;
p1phi3 =     2.560248;

p2m1 = 34727.597529;
p2m2 =   213.945331;
p2m3 =   417.550404;
p2phi1 =    -2.382826;
p2phi2 =     2.231943;
p2phi3 =    -0.623303;

p1_sim = readfile('p1.out');
p2_sim = readfile('p2.out');

K = size(p1_sim,1);

dt = dt*10^-5;
N = 1/(freq*dt);
```

```
t = [p1_sim(K-2*N,1):dt:p1_sim(K,1)];

p1_exp = p1m1*cos(1*omega*t+p1phi1)+p1m2*cos(2*omega*t+p1phi2)...
+p1m3*cos(3*omega*t+p1phi3);

p2_exp = (p2m1*cos(1*omega*t+p2phi1)+p2m2*cos(2*omega*t+p2phi2)...
+p2m3*cos(3*omega*t+p2phi3));

figure;
plot(t,p1_exp,'-b');
hold;
plot(p1_sim(K-2*N:K,1),p1_sim(K-2*N:K,2),'-g');
plot(t,p2_exp,'-r');
plot(p1_sim(K-2*N:K,1),p2_sim(K-2*N:K,2),'-m');
xlabel('Time [sec]');
ylabel('Gage Pressure [Pa]');
legend('p1_exp','p1_sim','p2_exp','p2_sim');
title('Simulated & Experimental Pressures');

[exp_xc,elags]=xcorr(p1_exp,p2_exp);
[sim_xc,slags]=xcorr(p1_sim(K-2*N:K,2),p2_sim(K-2*N:K,2));

[i,j] = max(exp_xc);
[k,l] = max(sim_xc);

exp_nt = elags(j);
sim_nt = slags(l);
sim_phase_ang = sim_nt*omega*dt;%*360/2/pi;
exp_phase_ang = exp_nt*omega*dt;%*360/2/pi;

[p1_sim_max_y,p] = max(p1_sim(K-1*N:K,2));
[p2_sim_max_y,m] = max(p2_sim(K-1*N:K,2));

[p1_exp_max_y,r] = max(p1_exp);
 [p2_exp_max_y,q] = max(p2_exp);

%displays the variable results in command window
display(p1_sim_max_y);
display(p2_sim_max_y);
display(sim_phase_ang);

display(p1_exp_max_y);
display(p2_exp_max_y);
display(exp_phase_ang);
null=0;
%--------------------------------------------------------------------
```

```
function res=readfile(name)
%subfunction res=readfile()
%[fname,pname]=uigetfile('*.*');         %select input file - tab del.
%filestring=strcat(pname,fname);         %

res=dlmread(name,' ',2,0);   %read tab-deliminated data
```

APPENDIX B

FLUENT USER DEFINED FUNCTIONS FOR PISTON WALL MOTION

System Level Models (Single Piston)

```
#include "udf.h"

DEFINE_CG_MOTION(vel_comp, dt, vel, omega, time, dtime)
{
  real freq=200.0;
  real w=2.0*M_PI*freq;
  real Xcomp=0.0007;

  /* reset velocities */
  NV_S (vel, =, 0.0);
  NV_S (omega, =, 0.0);

  vel[0] = w*Xcomp*cos(w*time);
}
```

Pulse Tube Component Level Models (Two PistonsWith Phase Difference)

```
#include "udf.h"

DEFINE_CG_MOTION(inlet_motion, dt, vel, omega, time, dtime)
{
  real freq = 200.0;
  real w = 2.0*M_PI*freq;
  real Xcomp = 0.0007;

  /* reset velocities */
  NV_S (vel, =, 0.0);
  NV_S (omega, =, 0.0);

  vel[0] = w*Xcomp*cos(w*time);
}

DEFINE_CG_MOTION(outlet_motion, dt, vel, omega, time, dtime)
{
  real freq = 200.0;
```

```
  real w = 2.0*M_PI*freq;
  real Xcomp = 0.0011;
  real phase = -0.36*M_PI;

  /* reset velocities */
  NV_S (vel, =, 0.0);
  NV_S (omega, =, 0.0);

  vel[0] = w*Xcomp*cos(w*time + phase);
}
```

APPENDIX C

MATLAB PROGRAMS FOR POST-PROCESSING SYSTEM LEVEL FLUENT MODELS

The following functions were used to post process the system level Fluent models. The first function performs control volume energy balances both on the entire system and on its individual components. The second function calculates phase angles between the oscillatory mass and velocity waveforms at the inlets to each component.

Enthalpy Balance (Individual Components and Complete System)

```
function out_files = enthalpy_bal_icc16(N,plots,clean)

%Enthalpy Balance Postprocessing for System Level Models
%if plots = 'component', control volume energy balances calculated
%if plots = 'overall', only overall energy balance
%if clean = clean, repeated data is removed
%if clean = raw, all data is plotted

close all; hold off;

%N = 250;      % number of points per period (period/time step)
n = N/2;       % midpoint of interval

if (strcmp(plots,'overall') ~= 1) & (strcmp(plots,'component') ~=1)
   error('invalid argument');
elseif (strcmp(clean,'clean') ~=1) & (strcmp(clean,'raw')~=1)
   error('invalid argument');
end

wd = cd;
path = strcat(wd,'\*.out');

out_files(1,1).name = 'tx_p.out';%tx p
out_files(2,1).name = 'tx_v.out';%tx v
out_files(3,1).name = 'tx_h_flow.out';
out_files(4,1).name = 'whx_1_h_flow.out';
out_files(5,1).name = 'whx_1_h_wall.out';
out_files(6,1).name = 'tx_h_wall.out';%tx h wall
out_files(7,1).name = 'whx_1_h_iw.out';
out_files(8,1).name = 'regen_sc.out';
out_files(9,1).name = 'regen_h_flow.out';
```

```
out_files(10,1).name = 'chx_h_flow.out';
out_files(11,1).name = 'chx_sc.out';
out_files(12,1).name = 'regen_h_iw.out';
out_files(13,1).name = 'chx_h_wall.out';
out_files(14,1).name = 'chx_h_iw.out';
out_files(15,1).name = 'pt_sc.out';
out_files(16,1).name = 'pt_h_flow.out';
out_files(17,1).name = 'pt_h_iw.out';
out_files(18,1).name = 'whx_2_sc.out';
out_files(19,1).name = 'whx_2_h_flow.out';
out_files(20,1).name = 'whx_2_h_wall.out';
out_files(21,1).name = 'whx_2_h_iw.out';
out_files(22,1).name = 'inertance_h_flow.out';
out_files(23,1).name = 'inertance_h_wall.out';
out_files(24,1).name = 'sv_h_flow.out';
out_files(25,1).name = 'sv_h_wall.out';
out_files(26,1).name = 'sv_h_wall.out'; %repeated, unused; this is a placeholder to
                                                    %maintain indices
out_files(27,1).name = 'regen_wall_ac_fluid.out';
out_files(28,1).name = 'regen_wall_chx_fluid.out';
out_files(29,1).name = 'pt_wall_chx_fluid.out';
out_files(30,1).name = 'pt_wall_whx_fluid.out';

k = size(out_files,1);
for i = 1:k
   out_files(i).data = readfile(out_files(i).name);
   if strcmp(clean,'clean') == 1
      out_files(i).data = cleanmyoutfile(out_files(i).data);
   end
   out_files(i).cycle_ave = cycleave(out_files(i).data,N,n);

end

%-----------------------------------------------------------------------
figure(1);
%Flow Enthalpy Plot
hold on;
title('Flow Enthalpy');
xlabel('time, sec.');
ylabel('Cycle Averaged Enthalpy flow, W');

dummy = [3 4 9 10 16 19 22 24];
color = ['g' 'r' 'k' 'b' 'm' 'y' 'c' ':g'];
z=1;

for i=dummy
```

```
plot(out_files(i).cycle_ave(:,1),out_files(i).cycle_ave(:,2),color(z));
z=z+1;

end

legend('inlet','whx_1','regen','chx','pt','whx_2','inertance', 'sv');
%------------------------------------------------------------------------
figure(2);
%System Level Enthalpy Balance (Control Surfaces)
hold on;
title('Overall Enthalpy Balance');
xlabel('time, sec.');
ylabel('Cycle Averaged Enthalpy flow, W');

dummy = [3 6 5 13 20 23 25];
color = ['g' 'r' 'k' 'b' 'm' 'y' 'c'];
z=1;

for i=dummy
plot(out_files(i).cycle_ave(:,1),out_files(i).cycle_ave(:,2),color(z));
z=z+1;

end

legend('Inlet','tx','whx_1','chx','whx_2','inertance','SV');

%------------------------------------------------------------------------
figure(3);
%Simplified Conrol Surface

hold on;
title('Simplified Overall Enthalpy Balance');
xlabel('time, sec.');
ylabel('Cycle Averaged Enthalpy flow, W');

% out_files(k+2).name = 'enthalpy balance';
% out_files(k+2).cycle_ave(1,2) = 0;

%add transfer line wall heat flux to whx 1
WHX1.cycle_ave(:,1) = out_files(5).cycle_ave(:,1);
WHX1.cycle_ave(:,2) = out_files(5).cycle_ave(:,2)+...
   out_files(6).cycle_ave(:,2);

%add inertance and sv wall heat flux to whx 2
WHX2.cycle_ave(:,1) = out_files(20).cycle_ave(:,1);
WHX2.cycle_ave(:,2) = out_files(20).cycle_ave(:,2) + ...
```

```
   out_files(23).cycle_ave(:,2) + out_files(25).cycle_ave(:,2);

plot(out_files(3).cycle_ave(:,1),out_files(3).cycle_ave(:,2),'c');
plot(WHX1.cycle_ave(:,1),WHX1.cycle_ave(:,2),'r');
plot(out_files(13).cycle_ave(:,1),out_files(13).cycle_ave(:,2),'b');
plot(WHX2.cycle_ave(:,1),WHX2.cycle_ave(:,2),'g');

Balance(:,1) = WHX1.cycle_ave(:,1);
Balance(:,2) = out_files(3).cycle_ave(:,2)+WHX1.cycle_ave(:,2)+...
   out_files(13).cycle_ave(:,2)+WHX2.cycle_ave(:,2);

plot(Balance(:,1),Balance(:,2),'k');

legend('inlet','whx_1','chx','whx_2','balance');

%------------------------------------------------------------------------
if strcmp(plots,'component') == 1
%component control volume plots

%------------------------------------------------------------------------
figure(4)
%Transfer Line
hold on;
dummy = [3 6 4];
flux_dir = [1 1 -1];     %included to correct for changes in surface normal defined by
                         %Fluent
z = 1;

%balance based on inlet-h
transfer_line_bal(:,1) = out_files(3).cycle_ave(:,1);
transfer_line_bal(1,2) = 0;

   for i=dummy
      plot(out_files(i).cycle_ave(:,1),out_files(i).cycle_ave(:,2),...
         color(z));
      transfer_line_bal(:,2) = transfer_line_bal(:,2) +...
         out_files(i).cycle_ave(:,2)*flux_dir(z);
      z=z+1;
   end

plot(transfer_line_bal(:,1),transfer_line_bal(:,2),color(z));
title('Transfer Line Enthalpy Balance');
xlabel('time, sec.');
ylabel('Cycle Averaged Enthalpy flow, W');
legend('inlet','wall','outlet','balance','PV','PV Balance');
```

```
%-----------------------------------------------------------------------
figure(5)
%Aftercooler
hold on;
dummy = [4 7 9 27];
flux_dir = [1 1 -1 1];

z = 1;
WHX1_bal(:,1) = out_files(4).cycle_ave(:,1);
WHX1_bal(1,2) = 0;

   for i=dummy
      plot(out_files(i).cycle_ave(:,1),out_files(i).cycle_ave(:,2),...
         color(z));
      WHX1_bal(:,2) = WHX1_bal(:,2) +...
         out_files(i).cycle_ave(:,2)*flux_dir(z);
      z=z+1;
   end

plot(WHX1_bal(:,1),WHX1_bal(:,2),color(z));
title('WHX1 Enthalpy Balance');
xlabel('time, sec.');
ylabel('Cycle Averaged Enthalpy flow, W');
legend('inlet','int wall','outlet','regen wall','balance');

%Aftercooler wall
figure(6);
hold on;

dummy = [7 8 5];
flux_dir = [1 -1 1];

z = 1;
WHX1_wall_bal(:,1) = out_files(7).cycle_ave(:,1);
WHX1_wall_bal(1,2) = 0;

   for i=dummy
      plot(out_files(i).cycle_ave(:,1),out_files(i).cycle_ave(:,2),...
         color(z));
      WHX1_wall_bal(:,2) = WHX1_wall_bal(:,2) +...
         out_files(i).cycle_ave(:,2)*flux_dir(z);
      z=z+1;
   end

plot(WHX1_wall_bal(:,1),WHX1_wall_bal(:,2),color(z));
title('WHX1 Wall Enthalpy Balance');
```

```
xlabel('time, sec.');
ylabel('Cycle Averaged Enthalpy flow, W');
legend('int wall','regen sc','outer wall','balance');
%------------------------------------------------------------------------
figure(7)
%Regenerator
hold on;
dummy = [9 12 10];
flux_dir = [1 1 1];

z = 1;
regenerator_bal(:,1) = out_files(9).cycle_ave(:,1);
regenerator_bal(1,2) = 0;

   for i=dummy
      plot(out_files(i).cycle_ave(:,1),out_files(i).cycle_ave(:,2),...
         color(z));
      regenerator_bal(:,2) = regenerator_bal(:,2) +...
         out_files(i).cycle_ave(:,2)*flux_dir(z);
      z=z+1;
   end

plot(regenerator_bal(:,1),regenerator_bal(:,2),color(z));
title('Regenerator Enthalpy Balance');
xlabel('time, sec.');
ylabel('Cycle Averaged Enthalpy flow, W');
legend('inlet','inner wall', 'outlet','balance');

%Regenerator Wall
figure(8);
hold on;

dummy = [8 11 12 27 28];
flux_dir = [1 -1 1 1 1];

z = 1;
regenerator_wall_bal(:,1) = out_files(7).cycle_ave(:,1);
regenerator_wall_bal(1,2) = 0;

   for i=dummy
      plot(out_files(i).cycle_ave(:,1),out_files(i).cycle_ave(:,2),...
         color(z));
      regenerator_wall_bal(:,2) = regenerator_wall_bal(:,2) +...
         out_files(i).cycle_ave(:,2)*flux_dir(z);
      z=z+1;
   end
```

```
plot(regenerator_wall_bal(:,1),regenerator_wall_bal(:,2),color(z));
title('Regenerator Wall Enthalpy Balance');
xlabel('time, sec.');
ylabel('Cycle Averaged Enthalpy flow, W');
legend('whx sc', 'chx sc','inner wall','aftercooler','chx','balance');

%------------------------------------------------------------------------
figure(9)
%Cold Heat Exchanger
hold on;
dummy = [10 14 16 28 29];
flux_dir = [1 1 1 1 1];

z = 1;
CHX_bal(:,1) = out_files(10).cycle_ave(:,1);
CHX_bal(1,2) = 0;

   for i=dummy
      plot(out_files(i).cycle_ave(:,1),out_files(i).cycle_ave(:,2),...
         color(z));
      CHX_bal(:,2) = CHX_bal(:,2) +...
         out_files(i).cycle_ave(:,2)*flux_dir(z);
      z=z+1;
   end

plot(CHX_bal(:,1),CHX_bal(:,2),color(z));
title('CHX Enthalpy Balance');
xlabel('time, sec.');
ylabel('Cycle Averaged Enthalpy flow, W');
legend('inlet','inner wall','outlet','regen wall','pt wall','balance');

%Cold Heat Exchanger Wall
figure(10)
hold on;
dummy = [11 14 15 13];
flux_dir = [1 1 1 1];

z = 1;
CHX_Wall_bal(:,1) = out_files(11).cycle_ave(:,1);
CHX_Wall_bal(1,2) = 0;

   for i=dummy
      plot(out_files(i).cycle_ave(:,1),out_files(i).cycle_ave(:,2),...
         color(z));
      CHX_Wall_bal(:,2) = CHX_Wall_bal(:,2) +...
```

```
            out_files(i).cycle_ave(:,2)*flux_dir(z);
        z=z+1;
    end

plot(CHX_Wall_bal(:,1),CHX_Wall_bal(:,2),color(z));
title('CHX Wall Enthalpy Balance');
xlabel('time, sec.');
ylabel('Cycle Averaged Enthalpy flow, W');
legend('regen sc','inner wall','pt sc','outer wall','balance');

%------------------------------------------------------------------------
figure(11)
%Pulse Tube
hold on;
dummy = [16 17 19];
flux_dir = [1 1 1];

z = 1;
PT_bal(:,1) = out_files(10).cycle_ave(:,1);
PT_bal(1,2) = 0;

    for i=dummy
        plot(out_files(i).cycle_ave(:,1),out_files(i).cycle_ave(:,2),...
            color(z));
        PT_bal(:,2) = PT_bal(:,2) +...
            out_files(i).cycle_ave(:,2)*flux_dir(z);
        z=z+1;
    end

plot(PT_bal(:,1),PT_bal(:,2),color(z));
title('Pulse Tube Enthalpy Balance');
xlabel('time, sec.');
ylabel('Cycle Averaged Enthalpy flow, W');
legend('inlet','inner wall','outlet','balance');

%Pulse Tube Wall
figure(12)
hold on;
dummy = [15 17 18 29 30];
flux_dir = [1 1 1 1 1];

z = 1;
PT_Wall_bal(:,1) = out_files(10).cycle_ave(:,1);
PT_Wall_bal(1,2) = 0;

    for i=dummy
```

```
      plot(out_files(i).cycle_ave(:,1),out_files(i).cycle_ave(:,2),...
         color(z));
      PT_Wall_bal(:,2) = PT_Wall_bal(:,2) +...
         out_files(i).cycle_ave(:,2)*flux_dir(z);
      z=z+1;
   end

plot(PT_Wall_bal(:,1),PT_Wall_bal(:,2),color(z));
title('Pulse Tube Wall Enthalpy Balance');
xlabel('time, sec.');
ylabel('Cycle Averaged Enthalpy flow, W');
legend('chx sc','inner wall','whx sc','chx','whx','balance');

%-----------------------------------------------------------------------
figure(13)
%Warm Heat Exchanger 2
hold on;
dummy = [19 21 22 30];
flux_dir = [1 1 1 1];

z = 1;
WHX2_bal(:,1) = out_files(19).cycle_ave(:,1);
WHX2_bal(1,2) = 0;

   for i=dummy
      plot(out_files(i).cycle_ave(:,1),...
         out_files(i).cycle_ave(:,2),color(z));
      WHX2_bal(:,2) = WHX2_bal(:,2) +...
         out_files(i).cycle_ave(:,2)*flux_dir(z);
      z=z+1;
   end

plot(WHX2_bal(:,1),WHX2_bal(:,2),color(z));
title('WHX2 Enthalpy Balance');
xlabel('time, sec.');
ylabel('Cycle Averaged Enthalpy flow, W');
legend('inlet','inner wall','outlet','pt wall','balance');

%Warm Heat Exchanger 2 Wall
figure(14)
hold on;
dummy = [18 21 20];
flux_dir = [1 1 1];

z = 1;
WHX2_Wall_bal(:,1) = out_files(19).cycle_ave(:,1);
```

```
WHX2_Wall_bal(1,2) = 0;

   for i=dummy
      plot(out_files(i).cycle_ave(:,1),...
         out_files(i).cycle_ave(:,2),color(z));
      WHX2_Wall_bal(:,2) = WHX2_Wall_bal(:,2) +...
         out_files(i).cycle_ave(:,2)*flux_dir(z);
      z=z+1;
   end

plot(WHX2_Wall_bal(:,1),WHX2_Wall_bal(:,2),color(z));
title('WHX2 Wall Enthalpy Balance');
xlabel('time, sec.');
ylabel('Cycle Averaged Enthalpy flow, W');
legend('pt sc','inner wall','outer wall','balance');

%-------------------------------------------------------------------------
figure(15)
%Inertance Line
hold on;
dummy = [22 23 24];
flux_dir = [1 1 -1];

z = 1;
inertance_bal(:,1) = out_files(13).cycle_ave(:,1);
inertance_bal(1,2) = 0;

   for i=dummy
      plot(out_files(i).cycle_ave(:,1),out_files(i).cycle_ave(:,2),...
         color(z));
      inertance_bal(:,2) = inertance_bal(:,2) +...
         out_files(i).cycle_ave(:,2)*flux_dir(z);
      z=z+1;
   end

plot(inertance_bal(:,1),inertance_bal(:,2),color(z));
title('Inertance Line Enthalpy Balance');
xlabel('time, sec.');
ylabel('Cycle Averaged Enthalpy flow, W');
legend('inlet','wall','outlet','balance');

%-------------------------------------------------------------------------
figure(16)
%Surge Volume
hold on;
dummy = [24 25];
```

```
flux_dir = [1 1];

z = 1;
SV_bal(:,1) = out_files(14).cycle_ave(:,1);
SV_bal(1,2) = 0;

   for i=dummy
      plot(out_files(i).cycle_ave(:,1),out_files(i).cycle_ave(:,2),...
         color(z));
      SV_bal(:,2) = SV_bal(:,2) +...
         out_files(i).cycle_ave(:,2)*flux_dir(z);
      z=z+1;
   end

plot(SV_bal(:,1),SV_bal(:,2),color(z));
title('Surge Volume Enthalpy Balance');
xlabel('time, sec.');
ylabel('Cycle Averaged Enthalpy flow, W');
legend('inlet','wall','balance');

end

null = 0;

%------------------------------------------------------------------------
function av_res=cycleave(res,N,n)

k = 20;                %window stepping interval
L=size(res,1);

for i=1:k:L-N+1
   sum = 0;
   for j=1:N
      sum = sum + res(i+j-1,2);
   end

   av_res((i-1)/k + 1,1)=res(i+n-1,1);
   av_res((i-1)/k + 1,2)=sum/N;

end

%------------------------------------------------------------------------
function res=readfile(name)

%subfunction res=readfile()
```

```
%[fname,pname]=uigetfile('*.*');         %select input file - tab del.
%filestring=strcat(pname,fname);         %
res=dlmread(name,' ',2,0);   %read space-deliminated data

%------------------------------------------------------------------------
function null = writefile(fname,pname,dat)

filestring = strcat(pname,fname);
dlmwrite(filestring,dat,'delimiter','\t','newline','pc');
null=0;

%------------------------------------------------------------------------
function cleandata = cleanmyoutfile(cleandata);

%This subroutine erases the new duplicate data when time steps have been repeated

KK = size(cleandata,1);

i = 1;

while i < KK
   if cleandata(i+1,1) <= cleandata(i,1)
      j =i+1; k =i+1;
      while cleandata(k,1) < cleandata(i,1);
         k = k+1;
      end
      cleandata(j:k,:)=[];
      KK = size(cleandata,1);
   end
   i = i+1;
end
```

Phase Angle Calculation (Inlet of Each Component)

```
function null = pressure_velocity_icc16(N)

%Pressure-Velocity Phase Angle Postprocessing for System Level Models

close all; hold off;

%N = 250;   % Number of points per period (period/time step)
n = N/2;    % midpoint of interval

clean = 'raw';
wd = cd;
path = strcat(wd,'\*.out');

    out_files(1,1).name = 'tx_p.out';
    out_files(2,1).name = 'tx_v.out';
    out_files(3,1).name = 'tx_h_flow.out';
    out_files(4,1).name = 'whx_1_p.out';
    out_files(5,1).name = 'whx_1_v.out';
    out_files(6,1).name = 'whx_1_h_flow.out';
    out_files(7,1).name = 'regen_p.out';
    out_files(8,1).name = 'regen_v.out';
    out_files(9,1).name = 'regen_h_flow.out';
    out_files(10,1).name = 'chx_p.out';
    out_files(11,1).name = 'chx_v.out';
    out_files(12,1).name = 'chx_h_flow.out';
    out_files(13,1).name = 'pt_p.out';
    out_files(14,1).name = 'pt_v.out';
    out_files(15,1).name = 'pt_h_flow.out';
    out_files(16,1).name = 'whx_2_p.out';
    out_files(17,1).name = 'whx_2_v.out';
    out_files(18,1).name = 'whx_2_h_flow.out';
    out_files(19,1).name = 'inertance_p.out';
    out_files(20,1).name = 'inertance_v.out';
    out_files(21,1).name = 'inertance_h_flow.out';
    out_files(22,1).name = 'sv_p.out';
    out_files(23,1).name = 'sv_v.out';
    out_files(24,1).name = 'sv_h_flow.out';

k = size(out_files,1);
```

```
for i = 1:k
   out_files(i).data = readfile(out_files(i).name);
   if strcmp(clean,'clean') == 1
      out_files(i).data = cleanmyoutfile(out_files(i).data);
   end
   out_files(i).cycle_ave = cycleave(out_files(i).data,N,n);

end

color = ['g' 'r' 'k' 'b' 'm' 'y' 'c'];

%-----------------------------------------------------------------------
Names = {'inlet' 'aftercooler' 'regenerator' 'chx' 'pt' 'whx' 'inertance'...
   'sv'};
Diameters = [.001; .001; .003; .003; .0025; .0025; .001; .001];

ph_ang(8).values = 0;
pv_pwr(8).values = 0;

for i = 1:8

   A(i)= pi*(Diameters(i)^2)/4;

   figure(i);
   title(Names(i));
   %subplot(2,2,1)
   hold on;
   %title('normalized waveforms');
   xlabel('time, sec.');
   ylabel('normalized pressure/velocity');

   pnorm = 4000000; %Pa, model mean pressure
   vnorm = max(out_files(3*i-1).data(:,2)); %m/s

   out_files(3*i-2).norm = normalize_data(out_files(3*i-2).data,pnorm);
   out_files(3*i-2).norm(:,2) = out_files(3*i-2).norm(:,2) - 1;
   pnorm2 = max(out_files(3*i-2).norm(:,2));
   out_files(3*i-2).norm = normalize_data(out_files(3*i-2).norm,pnorm2);

   out_files(3*i-1).norm = normalize_data(out_files(3*i-1).data,vnorm);

   plot(out_files(3*i-2).norm(:,1),out_files(3*i-2).norm(:,2),'r');
   plot(out_files(3*i-1).norm(:,1),out_files(3*i-1).norm(:,2),'b');

   legend('pressure','velocity');
```

```
    ph_ang(i).values=phase_angle(out_files(3*i-2).norm,...
       out_files(3*i-1).norm,N);

    pv_pwr(i).values = avg_inst_power(out_files(3*i-2).data,...
       out_files(3*i-1).data,N,A(i));

    hold off
    figure(100+i)          %phase angle vs time, approximate
    hold on
    title(Names(i));
    xlabel('time, sec.');
    ylabel('Phase Angle');
    plot(ph_ang(i).values(:,1),ph_ang(i).values(:,2));

    hold off
    figure(200+i)
    hold on
    title(Names(i));
    xlabel('time, sec.');
    ylabel('Power (W)');
    plot(pv_pwr(i).values(:,1),pv_pwr(i).values(:,2),'r',...
       out_files(3*i).cycle_ave(:,1),out_files(3*i).cycle_ave(:,2),'b');
    legend('Calculated','FLUENT');

    hold off
    figure(300+i)          %phase angle calculated by cross-correlation function
    hold on
    title(Names(i));
    xlabel(Phase Angle, Degrees.');
    ylabel('cross-correlation function');

    [c,lags] = xcorr(out_files(3*i-1).norm(:,2),out_files(3*i-2).norm(:,2),250);
    lags = lags/N*360;
    plot(lags,c)

end
null = out_files;

%--------------------------------------------------------------------------
function pv_pwr=avg_inst_power(Pressure_Data,Velocity_Data,N,cs_area)

k = 20;                %window stepping interval
n = int16(N/2);
L=size(Pressure_Data,1);
```

```
for i=1:k:L-N+1

   ave_pwr = mean(Pressure_Data(i:i+N,2).*Velocity_Data(i:i+N,2));
   pv_pwr((i-1)/k + 1,2)=ave_pwr*cs_area;
   pv_pwr((i-1)/k + 1,1)=Pressure_Data(i+n-1,1);

end

%-------------------------------------------------------------------------
function ph_ang=phase_angle(Pressure_Data,Velocity_Data,N)

k = 20;              %window stepping interval
n = int16(N/2);
L=size(Pressure_Data,1);

for i=1:k:L-N+1

   MAG = 2*mean(Pressure_Data(i:i+N,2).*Velocity_Data(i:i+N,2));
   maxP = max(Pressure_Data(i:i+N,2));
   maxV = max(Velocity_Data(i:i+N,2));

   ph_ang((i-1)/k + 1,2)=acos(MAG/(maxP*maxV))*180/pi;
   ph_ang((i-1)/k + 1,1)=Pressure_Data(i+n-1,1);

end

%---------------------------------------
function av_res=cycleave(res,N,n)

k = 20;              %window stepping interval

%res=readfile(name);     %read FLUENT results
L=size(res,1);

for i=1:k:L-N+1
   sum = 0;
   for j=1:N
      sum = sum + res(i+j-1,2);
   end
   av_res((i-1)/k + 1,1)=res(i+n-1,1);
   av_res((i-1)/k + 1,2)=sum/N;
end
```

```
%-------------------------------------------------------------------------
function res=readfile(name)

%subfunction res=readfile()

%[fname,pname]=uigetfile('*.*');         %select input file - tab del.
%filestring=strcat(pname,fname);         %
res=dlmread(name,' ',2,0);   %read space-deliminated data

%-------------------------------------------------------------------------

function null = writefile(fname,pname,dat)

filestring = strcat(pname,fname);
dlmwrite(filestring,dat,'delimiter','\t','newline','pc');
null=0;

%-------------------------------------------------------------------------
function cleandata = cleanmyoutfile(cleandata);
%[cleandata,header] = readfile(name);
%This subroutine erases the new duplicate data when time steps have been repeated.

KK = size(cleandata,1);

i = 1;

while i < KK
   if cleandata(i+1,1) <= cleandata(i,1)
      j =i+1; k =i+1;
      while cleandata(k,1) < cleandata(i,1);
         k = k+1;
      end
      cleandata(j:k,:)=[];
      KK = size(cleandata,1);
   end
   i = i+1;
end

%-------------------------------------------------------------------------
function norm_data = normalize_data(raw_data,nf)
% normalization function
%nf is normalization factor

norm_data(:,1) = raw_data(:,1);
norm_data(:,2) = raw_data(:,2)/nf;
```

APPENDIX D

MATLAB PROGRAM FOR POST-PROCESSING PULSE TUBE COMPONENT LEVEL MODELS

The following function was written to post-process the pulse tube component level models. Enthalpy flow rates, phase angles, and waveforms of pressure and mass flow rate are all calculated and plotted at the inlet to each component in the models.

```
function null = ICC16_PT(N,D)

% Postprocessing for Component Level Pulse Tube Models
%N – Number of Time Steps/Period
%D - PT diameter

close all; hold off;

%N = 250;   % Number of points per period (period/time step)
n = N/2;    % midpoint of interval

clean = 'raw';

wd = cd;
path = strcat(wd,'\*.out');

   out_files(1,1).name = 'chx_p.out';
   out_files(2,1).name = 'chx_v.out';
   out_files(3,1).name = 'chx_h.out';
   out_files(4,1).name = 'chx_mfr.out';
   out_files(5,1).name = 'chx_h_wall.out';

   out_files(6,1).name = 'pt_p.out';
   out_files(7,1).name = 'pt_v.out';
   out_files(8,1).name = 'pt_h.out';
   out_files(9,1).name = 'pt_mfr.out';
   out_files(10,1).name = 'pt_h_iw.out';

   out_files(11,1).name = 'whx_p.out';
   out_files(12,1).name = 'whx_v.out';
   out_files(13,1).name = 'whx_h.out';
   out_files(14,1).name = 'whx_mfr.out';
```

```
   out_files(15,1).name = 'whx_h_wall.out';

   out_files(16,1).name = 'outlet_p.out';
   out_files(17,1).name = 'outlet_v.out';
   out_files(18,1).name = 'outlet_h.out';
   out_files(19,1).name = 'outlet_mfr.out';
   out_files(20,1).name = 'outlet_h_wall.out';

   out_files(21,1).name = 'chx_h_iw.out';
   out_files(22,1).name = 'pt_h_iw.out';
   out_files(23,1).name = 'whx_h_iw.out';
   out_files(24,1).name = 'inlet_h_wall.out';

k = size(out_files,1);

for i = 1:k
   out_files(i).data = readfile(out_files(i).name);
   if strcmp(clean,'clean') == 1
      out_files(i).data = cleanmyoutfile(out_files(i).data);
   end
   out_files(i).cycle_ave = cycleave(out_files(i).data,N,n);
end

color = ['g' 'r' 'k' 'b' 'm' 'y' 'c'];

%---------------------------------------------------------------------

Names = {'chx' 'pt' 'whx' 'outlet'};
ph_ang(4).values = 0;
pv_pwr(4).values = 0;

for i = 1:4
   A(i)= pi*(D^2)/4;
   figure(i);
   title(Names(i));

   subplot(1,2,1)
   hold on;
   xlabel('time, sec.');
   ylabel('Pressure, Pa');
   plot(out_files(5*(i-1)+1).data(:,1),out_files(5*(i-1)+1).data(:,2),'r');

   subplot(1,2,2)
   hold on;
   xlabel('time, sec.');
   ylabel('mass flow rate, kg/s');
```

```
plot(out_files(5*(i-1)+4).data(:,1),-out_files(5*(i-1)+4).data(:,2),'r');

figure(100+i);
title(Names(i));
hold on;
pnorm = 4000000; %Pa

mnorm = -max(out_files(5*(i-1)+4).data(:,2)); %kg/s
vnorm = -max(out_files(5*(i-1)+2).data(:,2)); %m/s
%mass flow rates are inverted; correct above

out_files(5*(i-1)+1).norm = normalize_data(out_files(5*(i-1)+1).data,pnorm);
out_files(5*(i-1)+1).norm(:,2) = out_files(5*(i-1)+1).norm(:,2) - 1;
pnorm2 = max(out_files(5*(i-1)+1).norm(:,2));
out_files(5*(i-1)+1).norm = normalize_data(out_files(5*(i-1)+1).norm,pnorm2);
out_files(5*(i-1)+2).norm = normalize_data(out_files(5*(i-1)+2).data,vnorm);
out_files(5*(i-1)+4).norm = normalize_data(out_files(5*(i-1)+4).data,mnorm);

plot(out_files(5*(i-1)+1).norm(:,1),out_files(5*(i-1)+1).norm(:,2),'r');
plot(out_files(5*(i-1)+4).norm(:,1),out_files(5*(i-1)+4).norm(:,2),'b');
legend('pressure','mass flow rate');

ph_ang(i).values=phase_angle(out_files(5*(i-1)+1).norm,...
   out_files(5*(i-1)+4).norm,N);
figure(200+i);
title(Names(i));

subplot(1,2,1);
hold on
xlabel('time, sec.');
ylabel('Phase Angle');
plot(ph_ang(i).values(:,1),ph_ang(i).values(:,2));

subplot(1,2,2);
hold on
title(Names(i));
xlabel('time, sec.');
ylabel('Power (W)');
plot(out_files(5*(i-1)+3).cycle_ave(:,1),-out_files(5*(i-1)+3).cycle_ave(:,2),'b');

hold off
figure(300+i)
hold on
title(Names(i));
xlabel('Phase Angle, Degrees');
ylabel('cross-correlation function');
  [c,lags] = xcorr(out_files(5*(i-1)+1).norm(:,2),out_files(5*(i-1)+2).norm(:,2),250);
```

```
   lags = lags/N*360;
   plot(lags,c)

end

%-------------------------------------------------------------------------
figure(400);
hold on;
title('Energy Balance');
CHX(:,1) = out_files(5).cycle_ave(:,1);
CHX(:,2) = out_files(5).cycle_ave(:,2)+out_files(24).cycle_ave(:,2);
WHX(:,1) = out_files(15).cycle_ave(:,1);
WHX(:,2) = out_files(15).cycle_ave(:,2)+out_files(20).cycle_ave(:,2);
plot(CHX(:,1),CHX(:,2),'b',WHX(:,1),WHX(:,2),'r');
legend('CHX','WHX');

null = out_files;
%-------------------------------------------------------------------------
function ph_ang=phase_angle(Pressure_Data,Velocity_Data,N)

k = 20;                %window stepping interval
n = int16(N/2);
L=size(Pressure_Data,1);

for i=1:k:L-N
   MAG = 2*mean(Pressure_Data(i:i+N,2).*Velocity_Data(i:i+N,2));
   maxP = max(Pressure_Data(i:i+N,2));
   minP = min(Pressure_Data(i:i+N,2));
   Pamp = abs((maxP)+abs(minP))/2;

   maxV = max(Velocity_Data(i:i+N,2));
   minV = min(Velocity_Data(i:i+N,2));
   Vamp = abs((maxV)+abs(minV))/2;

   ph_ang((i-1)/k + 1,2)=acos(MAG/(Pamp*Vamp))*180/pi;
   ph_ang((i-1)/k + 1,1)=Pressure_Data(i+n-1,1);
end

%---------------------------------------
function av_res=cycleave(res,N,n)

k = 20;                %window stepping interval
L=size(res,1);
for i=1:k:L-N+1
   sum = 0;
   for j=1:N
```

```
      sum = sum + res(i+j-1,2);
   end
   av_res((i-1)/k + 1,1)=res(i+n-1,1);
   av_res((i-1)/k + 1,2)=sum/N;
end
%------------------------------------------------------------------------
function res=readfile(name)
%subfunction res=readfile()
%[fname,pname]=uigetfile('*.*');        %select input file - tab del.
%filestring=strcat(pname,fname);        %
res=dlmread(name,' ',2,0);                %read space-deliminated data

%------------------------------------------------------------------------
function null = writefile(fname,pname,dat)
filestring = strcat(pname,fname);
dlmwrite(filestring,dat,'delimiter','\t','newline','pc');
null=0;

%------------------------------------------------------------------------
function cleandata = cleanmyoutfile(cleandata);

%[cleandata,header] = readfile(name);
%This subroutine erases the new duplicate data.

KK = size(cleandata,1);

i = 1;
while i < KK
   if cleandata(i+1,1) <= cleandata(i,1)
      j =i+1; k =i+1;
      while cleandata(k,1) < cleandata(i,1);
         k = k+1;
      end
      cleandata(j:k,:)=[];
      KK = size(cleandata,1);
   end
   i = i+1;
end

%------------------------------------------------------------------------
function norm_data = normalize_data(raw_data,nf)
% normalization function
%nf is normalization factor
norm_data(:,1) = raw_data(:,1);
norm_data(:,2) = raw_data(:,2)/nf;
```

REFERENCES

[1] R. Radebaugh, "Cryocoolers: the state of the art and recent developments," *Journal of Physics: Condensed Matter*, vol. 21, 2009.

[2] G. Walker, *Low-capacity cryogenic refrigeration*, New York: Oxford University Press, 1994.

[3] R. Radebaugh, "Development of the pulse tube refrigerator as an efficient and reliable cryocooler," *Proc. Institute of Refrigeration (London)*, 2000.

[4] R. Ross, "Aerospace coolers: a 50-year quest for long-life cryogenic cooling in Space," *Cryogenic Engineering*, 2007, p. 225–284.

[5] X. Yang and J. Chung, "Size effects on miniature Stirling cycle cryocoolers," *Cryogenics*, vol. 45, 2005, pp. 537-545.

[6] R. Peterson, "Size limits for regenerative heat engines," *Microscale Thermophysical Engineering*, vol. 2, 1998, pp. 121-131.

[7] A. Veprik, H. Vilenchik, and S. Riabzev, "Microminiature Linear Split Stirling Cryogenic Cooler for Portable Infrared Applications," *Cryocoolers*, vol. 14, 2007, pp. 105-115.

[8] M. Mai, I. Ruehlich, C. Rosenhagen, T. Wiedmann, A.I.M.I.M. GmbH, and G. Heilbronn, "Development of the Miniature Flexure Bearing Cryocooler SF070," *Cryocoolers*, vol. 15, 2009, pp. 133-138.

[9] A. Veprik, S. Zehtzer, H. Vilenchik, N. Pundak, and J.G. Weisend, "Micro-Miniature Split Stirling Linear Crycooler," *Engineering Conference*, vol. 55, 2010, pp. 363-370.

[10] W.E. Gifford and R. Longsworth, "Pulse Tube Refrigeration," *Winter Annual Meeting of the ASME*, Philadelphia, PA: 1963.

[11] E.I. Mikulin, A.A. Tarasov, and M.P. Shkrebonock, "Low Temperature Expansion Pulse Tubes," *Adv. in Cryogenic Engineering*, vol. 29, 1984, pp. 629-637.

[12] R. Radebaugh, J. Zimmerman, D. Smith, and B. Louie, "A comparison of three types of pulse tube refrigerators-New methods for reaching 60 K," *Adv. in Cryogenic Engineering*, vol. 31, 1986, p. 779.

[13] S. Zhu, P. Wu, and Z. Chen, "Double inlet pulse tube refrigerators: an important improvement," *Cryogenics*, vol. 30, Jun. 1990, pp. 514-520.

[14] S.W. Zhu, S.L. Zhou, N. Yoshimura, and Y. Matsubara, "Phase shift effect of the long neck tube for the pulse tube refrigerator," *Cryocoolers*, vol. 9, 1997, pp. 269-278.

[15] D.L. Gardner and G.W. Swift, "Use of inertance in orifice pulse tube refrigerators," *Cryogenics*, vol. 37, 1997, pp. 117-121.

[16] R. Radebaugh, "Pulse tube cryocoolers for cooling infrared sensors," *Proceedings of SPIE*, vol. 4130, 2000, pp. 363-379.

[17] M.H. Lin, P.E. Bradley, H.J. Wu, J. Booth, R. Radebaugh, and Y. Lee, "Design, fabrication, and assembly of a hollow-core fiber-based micro cryogenic cooler," *Solid-State Sensors, Actuators and Microsystems Conference, 2009. Transducers 2009.*, Denver, CO: IEEE, 2009, p. 1114–1117.

[18] W.L. Swift, F.X. Dolan, M.V. Zagarola, J.G. Weisend, J. Barclay, S. Breon, J. Demko, M. DiPirro, J.P. Kelley, P. Kittel, A. Klebaner, A. Zeller, M. Zagarola, S. Van Sciver, A. Rowe, J. Pfotenhauer, T. Peterson, and J. Lock, "the Nicmos Cooling System—5 Years of Successful on-Orbit Operation," *AIP Conference Proceedings*, vol. 53, 2008, pp. 799-806.

[19] F.J. DiSalvo, "Thermoelectric Cooling and Power Generation," *Science*, vol. 285, Jul. 1999, pp. 703-706.

[20] R. Venkatasubramanian, "Cascade Cryogenic Thermoelectric Cooler for Cryogenic and Room Temperature Applications," , March 2003.

[21] P.E. Phelan, V. a Chiriac, and T.-Y.T. Lee, "Current and future miniature refrigeration cooling technologies for high power microelectronics," *IEEE Transactions on Components and Packaging Technologies*, vol. 25, Sep. 2002, pp. 356-365.

[22] M. Moran, D. Wesolek, B. Berhane, and K. Rebello, "Microsystem cooler development," *2nd International Energy Conversion Engineering Conference*, Providence, RI: 2004.

[23] *Defense Advanced Research Projects Agency Microsystems Technology Office* (n.d.) Available: http://www.darpa.mil/

[24] A.G. Nnanna, "Application of refrigeration system in electronics cooling," *Applied Thermal Engineering*, vol. 26, Jan. 2006, pp. 18-27.

[25] R. Mongia, K. Masahiro, E. DiStefano, J. Barry, W. Chen, M. Izenson, F. Possamai, a Zimmermann, and M. Mochizuki, "Small scale refrigeration system for electronics cooling within a notebook computer," *Thermal and Thermomechanical Proceedings 10th Intersociety Conference on Phenomena in Electronics Systems, 2006. ITHERM 2006.*, 2006, pp. 751-758.

[26] C.S. Kirkconnell, "A cryocooler in your laptop computer? Maybe," *Electronics Cooling*, vol. 11, 2008.

[27] P. Nika, Y. Bailly, M.D. Labachelerie, J. Jeannot, and J. Lalee, "Miniature Pulse Tube for the Cooling of Electronic Devices: Functioning Principles and Practical Modeling," *Microscale Thermophysical Engineering*, vol. 8, 2004, pp. 301-325.

[28] R. Radebaugh and A. O'Gallagher, "Regenerator operation at very high frequencies for microcryocoolers," *Adv. in Cryogenic Engineering*, vol. 51, 2006, pp. 1919-1928.

[29] I. Garaway, Z.H. Gan, P.E. Bradley, A. Veprik, and R. Radebaugh, "Development of a Miniature 150 Hz Pulse Tube Cryocooler," *Cryocoolers*, vol. 15, 2008, pp. 105-113.

[30] I. Garaway and G. Grossman, “A Study of High Frequency Miniature Reservoir-Less Pulse Tube,” *Adv. in Cryogenic Engineering*, vol. 53, 2008, pp. 1547-1554.

[31] M. Moran, S. Stelter, and M. Stelter, “Micro-Scale Regenerative Heat Exchanger,” *Conference on Micro-Nano-Technologies*, Monterey, California: 2004.

[32] X.X. Chu, Z.X. Wu, R.J. Huang, Y. Zhou, and L.F. Li, “Mechanical and thermal expansion properties of glass fibers reinforced PEEK composites at cryogenic temperatures,” *Cryogenics*, vol. 50, Feb. 2010, pp. 84-88.

[33] G.W. Swift and S. Garrett, *Thermoacoustics: A unifying perspective for some engines and refrigerators*, 2003.

[34] H. Cai, L. Yang, E. Luo, and Y. Zhou, “A 300Hz two-stage pulse tube cryocooler that attains 58K,” *Cryogenics*, vol. 50, Aug. 2010, pp. 469-471.

[35] P. Nika, “An integrated pulse tube refrigeration device with micro exchangers: design and experiments,” *International Journal of Thermal Sciences*, vol. 42, Nov. 2003, pp. 1029-1045.

[36] D. Guidry, J. McLean, and W. Avants, “Microfabricated Microchanel Regenerators for Cryocoolers,” *Adv. in Cryogenic Engineering*, vol. 51, 2006, pp. 1895-1903.

[37] M. Petach, M. Waterman, G. Pruitt, and E. Tward, “High Frequency Coaxial Pulse Tube Microcooler,” *Cryocoolers*, vol. 15, 2009, pp. 97-103.

[38] S. Vanapalli, H.J.M. Ter Brake, H.V. Jansen, Y. Zhao, H.J. Holland, J.F. Burger, and M.C. Elwenspoek, "High frequency pressure oscillator for microcryocoolers.," *Review of Scientific Instruments*, vol. 79, 2008, p. 045103.

[39] I. Garaway and G. Grossman, "Piezo-Hydraulic Actuation for Driving High Frequency Miniature Split-Stirling Pulse Tube Cryocoolers," *Adv. in Cryogenic Engineering*, vol. 53, 2008, p. 622.

[40] M. Xu, Y. He, P. Wu, and Z. Chen, "Experimental research of a miniature coaxial pulse tube refrigerator using nylon tube," *Cryogenics*, vol. 36, 1996, pp. 131-133.

[41] P. Curlier, "Progress on miniature pulse tube cryocoolers for the commercial and military market," *Proceedings of SPIE*, vol. 3061, 1997, pp. 84-92.

[42] J. Liang, Y. Zhou, W. Zhu, W. Sun, J. Yang, and S. Li, "Study on miniature pulse tube cryocooler for space application," *Cryogenics*, vol. 40, 2000, pp. 229-233.

[43] E. Tward, T. Nguyen, J. Godden, and G. Toma, "Miniature Pulse Tube Cooler," *Adv. in Cryogenic Engineering*, vol. 49, 2004, pp. 1326-1329.

[44] H. Chen, L.W. Yang, J.H. Cai, J. Liang, L. Zhang, and Y. Zhou, "An Integrated Miniature Pulse Tube Cryocooler at 80K," *Adv. in Cryogenic Engineering*, vol. 53, 2008, pp. 673-677.

[45] S. Vanapalli, M.A. Lewis, Z.H. Gan, and R. Radebaugh, "120 Hz pulse tube cryocooler for fast cooldown to 50 K," *Applied physics letters*, 2007, pp. 7-10.

[46] S. Vanapalli, M.A. Lewis, G. Grossman, Z.H. Gan, R. Radebaugh, H.J.M.T. Brake, J.G. Weisend, J. Barclay, S. Breon, J. Demko, M. DiPirro, J.P. Kelley, P. Kittel, A. Klebaner, A. Zeller, M. Zagarola, S. Van Sciver, A. Rowe, J. Pfotenhauer, T. Peterson, and J. Lock, "Modeling and Experiments on Fast Cooldown of a 120 Hz Pulse Tube Cryocooler," *Adv. in Cryogenic Engineering*, vol. 53, 2008, pp. 1429-1436.

[47] I. Garaway and G. Grossman, "Studies in high frequency oscillating compressible flow for application in a micro regenerative cryocooler," *Adv. in Cryogenic Engineering*, vol. 51, 2006, pp. 1588-1595.

[48] I. Garaway, A. Veprik, R. Radebaugh, and J.G. Weisend, "Diagnostics and Optimization of a Miniature High Frequency Pulse Tube Cryocooler," *Adv. in Cryogenic Engineering*, vol. 55, 2010, pp. 167-174.

[49] S. Sobol, Y. Katz, and G. Grossman, "A Study of a Miniature In-Line Pulse Tube Cryocooler," *Cryocoolers*, vol. 16, 2010, pp. 87-95.

[50] P. Nika and Y. Bailly, "Comparison of two models of a double inlet miniature pulse tube refrigerator: Part A thermodynamics," *Cryogenics*, vol. 42, 2002, pp. 593-603.

[51] Y. Bailly and P. Nika, "Comparison of two models of a double inlet miniature pulse tube refrigerator: Part B electrical analogy," *Cryogenics*, vol. 42, 2002, p. 605–615.

[52] B. Ward and G.W. Swift, "Design Environment for Low-Amplitude ThermoAcoustic Engines (DeltaE) Tutorial and User's Guide (Version 5.1)," *Los Alamos National Laboratory*, 2001.

[53] J. Gary, A.O. Gallagher, R. Radebaugh, Y. Huang, and E. Marquardt, *REGEN 3.3 User Manual*, 2008.

[54] D. Gedeon, *Sage User's Guide*, Gedeon Associates, 2009.

[55] R.W. Dyson, S.D. Wilson, R.C. Tew, and R. Demko, "On the Need for Multidimensional Stirling Simulations," *NASA Technical Memorandum 2005-21397*, 2005.

[56] T. Conrad, E. Landrum, S.M. Ghiaasiaan, and C.S. Kirkconnell, "CFD Modeling of Meso-Scale and Micro-Scale Pulse Tube Refrigerators," *Cryocoolers*, vol. 15, 2008, pp. 241-249.

[57] J.J. Cha, S.M. Ghiaasiaan, P.V. Desai, J.P. Harvey, and C. Kirkconnell, "Multi-dimensional flow effects in pulse tube refrigerators," *Cryogenics*, vol. 46, 2006, p. 658–665.

[58] R. Taylor, G. Nellis, and S. Klein, "Optimal Pulse-Tube Design Using Computational Fluid Dynamics," *Adv. in Cryogenic Engineering*, vol. 53, 2008, pp. 1445-1453.

[59] X. Zhang, L. Qiu, Z.H. Gan, and Y. He, "CFD study of a simple orifice pulse tube cooler," *Cryogenics*, vol. 47, 2007, pp. 315-321.

[60] B. Flake and A. Razani, "Modeling pulse tube cryocoolers with CFD," *Adv. in Cryogenic Engineering*, vol. 49, 2004, pp. 1493-1499.

[61] I. Nachman, N. Pundak, and G. Grossman, "CFD Modeling of Reciprocating Flow around a Bend in Pulse Tube Cryocoolers," *Cryocoolers*, vol. 15, 2009, pp. 251-259.

[62] Fluent Inc., *Fluent 6.3 User's Guide*, 2006.

[63] J.P. Harvey, "Oscillatory Compressible Flow and Heat Transfer in Porous Media – Application To Cryocooler Regenerators," Georgia Instituite of Technology, 2003.

[64] W.M. Clearman, "Measurement and Correlation of Directional Permeability and Forchheimer's Inertial Coefficient of Micro Porous Structures Used in Pulse-Tube Cryocoolers," Georgia Institute of Technology, 2007.

[65] J.J. Cha, "Hydrodynamic Parameters of Micro Porous Media for Steady and Oscillatory Flow : Application to Cryocooler Regenerators," Ph.D Thesis, Georgia Institute of Technology, 2007.

[66] E. Landrum, "Anisotropic Parameters of Mesh Fillers Relevant to Miniature Cryocoolers," Georgia Institute of Technology, 2009.

[67] Q. Shen and Y. Ju, "A New Correlation of Friction Factor for Oscillating Flow Regenerator Operating at High Frequencies," *Adv. in Cryogenic Engineering*, vol. 53, 2008, pp. 1507 - 1514.

[68] K. Nam and S. Jeong, “Investigation of oscillating flow friction factor for cryocooler regenerator considering cryogenic temperature effect,” *Cryogenics*, vol. 45, 2005, p. 733–738.

[69] M.G. Pathak, “Thermal Dispersion and Convective Heat Transfer During Laminar Pulsating Flow in Porous Media,” Georgia Institute of Technology, 2010.

[70] F. Kuwahara, M. Shirota, and A. Nakayama, “A numerical study of interfacial convective heat transfer coefficient in two-energy equation model for convection in porous media,” *International Journal of Heat and Mass Transfer*, vol. 44, Mar. 2001, pp. 1153-1159.

[71] F. Kuwahara, A. Nakayama, and H. Koyama, “A numerical study of thermal dispersion in porous media,” *Journal of heat transfer*, vol. 118, 1996, p. 756.

[72] A. Nakayama, F. Kuwahara, T. Umemoto, and T. Hayashi, “Heat and fluid flow within an anisotropic porous medium,” *Journal of Heat Transfer*, vol. 124, 2002, p. 746–753.

[73] S.M. Kim and S. Ghiaasiaan, “Numerical modeling of laminar pulsating flow in porous media,” *Journal of Fluids Engineering*, vol. 131, 2009.

[74] D.A. Nield and A. Bejan, *Convection in porous media*, New York: Springer Verlag, 1998.

[75] E. Landrum, T. Conrad, S.M. Ghiaasiaan, and C.S. Kirkconnell, "Hydrodynamic parameters of mesh fillers relevant to miniature regenerative cryocoolers," *Cryogenics*, vol. 50, 2010, pp. 373-380.

[76] E. Landrum, T. Conrad, and S. Ghiaasiaan, "Effect of Pressure on Hydrodynamic Parameters of Several PTR Regenerator Fillers In Axial Steady Flow," *Cryocoolers*, vol. 15, 2008, pp. 335-342.

[77] M.H.J. Pedras and M.J.S. de Lemos, "Macroscopic turbulence modeling for incompressible flow through undeformable porous media," *International journal of heat and mass transfer*, vol. 44, 2001, p. 1081–1093.

[78] E.C. Landrum, T.J. Conrad, M.G. Pathak, S.M. Ghiaasiaan, C.S. Kirkconnell, T. Crittenden, and S. Yorish, "Effect of Frequency on Hydrodynamic Parameters of Mesh Fillers in Oscillatory Flow," *Cryocoolers*, vol. 16, 2011, pp. 411-418.

[79] *Thermophysical Properties of Fluid Systems* (n.d.) Available: *http://webbook.nist.gov/chemistry/fluid/*.